UNIVERSITAT JAUME·I

(Photo)electrochemical approaches for renewable energy storage into high-added value chemicals

Roser Fernandez Climent

Supervisor: Prof. Sixto Giménez Juliá

Doctoral Thesis
February 2024

Programa de Doctorat en Ciències
Escola de Doctorat de la Universitat Jaume I

(Photo)electrochemical approaches for renewable energy storage into high-added value chemicals

Report submitted by Roser Fernandez Climent in order to be eligible for a Doctoral degree awarded by the Universitat Jaume I.

Firmado por ROSER FERNANDEZ CLIMENT -

Roser Fernandez Climent
Ph.D. Candidate

SIXTO| GIMENEZ| JULIA

Firmado digitalmente por SIXTO|GIMENEZ|JULIA
Nombre de reconocimiento (DN): cn=SIXTO|GIMENEZ|JULIA, serialNumber=34804561H, givenName=SIXTO, sn=GIMENEZ JULIA, ou=CIUDADANOS, o=ACCV, c=ES
Fecha: 2024.02.02 12:02:17 +01'00'

Sixto Giménez Juliá
Director

Castelló de la Plana, February 2024

Funding

- Project: “An Artificial Leaf: a photo-electrocatalytic cell from earth-abundant materials for sustainable solar production of CO_2-based chemicals and fuels” (A-LEAF), European Union Horizon 2020, reference 732840.
- Project: “Desarrollo de Sistemas electrocatalíticos integrados para la síntesis de productos químicos de alto valor añadido (PID2020-116093RB-C41)” funded by MCIN/ AEI/10.13039/501100011033/ and by “ERDF A way of making Europe”, by the “European Union”.
- Project: “Contrato de evaluación de tecnología”, H2B2 Electrolysis Technologies S.L.

Acknowledgements

In this section, I would like to express my gratitude to all the people who have supported me during this doctoral thesis. This section is written in English, Spanish and Valencian.

En primer lugar, quiero agradecer a mi director Sixto Giménez por darme la oportunidad de formar parte de su equipo de investigación para realizar la presente tesis doctoral. Gracias por toda la confianza depositada en mí para llevar a cabo este proyecto, por el apoyo tanto profesional como personal recibido y por preocuparte porque todo el esfuerzo llegase a buen puerto. También quiero agradecer a la directora del INAM Elena Mas y al resto de profesores, compañeros y equipo administrativo. Fue bonito compartir no solo ciencia con vosotros. Quiero hacer una mención especial a aquellas personas que durante estos años se convirtieron en amigos: Agus, Ana, Cam, Drialys, Laura, Loles, Marisé, Marta, Nihal, Nuria y Ramón. Vuestro apoyo y amistad fueron fundamentales. Todo lo que compartimos y vivimos juntos lo llevaré siempre conmigo. Cam, un gracias muy grande para ti, por todo tu apoyo, por levantarme y levantarnos juntos del suelo tantas veces, por hacerlo posible. Gracias por creer siempre en mí y haberme valorado tantísimo como científica.

Me siento muy afortunada y agradecida por cada una de las colaboraciones realizadas durante este proyecto que me han permitido aprender y conocer a personas extraordinarias. Gracias Iván Mora y equipo por introducirme en el mundo de los nano cristales de perovskita y por las discusiones científicas tan interesantes que surgieron por el camino. Thank you very much Nikolay Kornienko for being interested in our work at that conference in Barcelona. Your powerful *operando* characterization measurements have been extremely helpful for the study of our electrocatalyst. Muchas gracias Sara Barja por acogerme con tanto cariño en San Sebastián. Aprender sobre XPS y compartir tiempo contigo, con Fred y con Jesús fue una suerte enorme que siempre recordaré con mucho respeto y cariño. Incluso hacer malabares con un *tupperware* y una bolsa de nitrógeno fue increíble. Grazie mille Claudio Ampelli for hosting me in your lab in Messina for my doctoral research stay. Thank you for giving me the opportunity to learn from such an incredible team and for making me feel part of it. Also thanks to Chiara, Matteo, Luana and Daniele for your time and help, I am extremely grateful to all of you. También quiero dar las gracias a todos los técnicos de Serveis Centrals d'Instrumentació Científica de la UJI por el apoyo recibido para la realización de los análisis estructurales y morfológicos.

Però, sense dubte tots aquests anys plens d'esforços, resistència i resiliència no hagueren estat possible sense el meu *equip*. El meu profund agraïment a cadascuna de les persones que amb el seu recolzament, confiança i estima em fan ser capaç d'aplegar allà on em propose per molt que es pugui complicar el camí.

Imprescindibles les meues amigues i el seu suport incondicional. A Àngela, Àngels, Cristina, Elena, Irma, Lidia, Mireia, Roser, Sheila i resta de *comboiet* i de *dolçaineres* moltes gràcies per estar-hi sempre, per escoltar-me, recolzar-me, animar-me, confiar en mi i treure'm de casa quan tot pesava massa. A les meues químiques preferides Ele, Eva, i Maria, gràcies de tot cor per tindre sempre ben a prop la vostra mà. Sou amistat, inspiració i refugi segur dins i fora de l'UJI. També als qui en algun moment van formar part de l'aventura, gràcies. Gràcies Ivan pels teus ànims, suport incondicional i per creure sempre en mi. *Merci* Mariona perquè has sigut un descobriment molt bonic aquest any.

I per últim i més important, gràcies a la meua família. Gràcies als meus pares, Pedro i Susi, sou totes les coses bones que s'ha de ser en la vida, sou bondat, amor, esforç i perseverança. Gràcies per confiar cegament en mi, perquè tot el que sóc i tot allò que aconsegueixi és gràcies a vosaltres. Què fàcil és volar si vosaltres hi sou al niu. Gràcies al meu germà Pau i a Teresa i als meus nebots Mateo y Clara. Clara, vas arribar en plena escriptura de tesi per a donar caliu en aquells dies tan complicats. Mateo, *carinyo*, tu encara no eres conscient de tot el que eres per a la tia. Passar temps amb tu i gaudir d'eixe vincle tan bonic que tenim ha sigut la millor teràpia. Finalment als qui ja no esteu, però que mai haveu deixat de ser-hi, els meus iaios Asunción i Sisco. Sempre hi sereu amb mi en cada pas i des d'allà on esteu sols vull que sapigueu que ho he aconseguit, que no ha estat fàcil però que a pesar de tot mai ho he deixat d'intentar i mai he perdut la il·lusió. Que he aplegat fins el final i ho he fet amb vosaltres.

Als meus pares, Pedro i Susi

I hereby declare that except when specific reference is made, the material presented in this thesis is the result of my own work.

List of publications

- García-Tecedor, M.; Cardenas-Morcoso, D.; **Fernández-Climent, R**.; & Giménez, S. (**2019**). The role of underlayers and overlayers in thin film $BiVO_4$ photoanodes for solar water splitting. *Advanced Materials Interfaces*, *6*(15), 1900299.

- **Fernández-Climent, R**.; Giménez, S.; & García-Tecedor, M. (**2020**). The role of oxygen vacancies in water splitting photoanodes. *Sustainable Energy & Fuels*, *4*(12), 5916-5926.

- **Fernández-Climent, R.**; Gualdrón-Reyes, A. F.; García-Tecedor, M.; Mesa, C. A.; Cárdenas-Morcoso, D.; Montañes, L.; Barea, E.M.; Mas-Marzá, E.; Julián-López, B.; Mora-Seró, I.; & Giménez, S. (**2022**). Switchable All Inorganic Halide Perovskite Nanocrystalline Photoelectrodes for Solar-Driven Organic Transformations. *Solar RRL*, *6*(1), 2100723.

- Gualdrón-Reyes, A. F.; **Fernández-Climent, R**.; Masi, S.; Mesa, C. A.; Echeverría-Arrondo, C.; Aiello, F.; Balzano F.; Uccello-Barretta G.; Rodríguez-Pereira, J.; Giménez, S.; & Mora-Seró, I. (**2023**). Efficient Ligand Passivation Enables Ultrastable $CsPbX_3$ Perovskite Nanocrystals in Fully Alcohol Environments. *Advanced Optical Materials*, *11*(12), 2203096.

- **Fernández-Climent, R**.; Redondo, J.; García-Tecedor, M.; Spadaro, M. C.; Li, J.; Chartrand, D.; Schiller, F.; Pazos, J.; Hurtado, M. F.; de la Peña O'Shea, V.; Kornienko. N.; Arbiol, J.; Barja, S.; Mesa, C.A.; & Giménez, S. (**2023**). Highly Durable Nanoporous $Cu_{2-x}S$ Films for Efficient Hydrogen Evolution Electrocatalysis under Mild pH Conditions. *ACS catalysis*, *13*(15), 10457-10467.

Abstract

An energy transition toward a clean and sustainable model is crucial to overcome the well-known problems related to traditional coal energy consumption. In this regard, the generation and storage of renewable energies is key to this transition. (Photo)electrochemical systems powered by renewable energy have emerged as a promising technology for storing renewable energy in chemical bonds. However, the scalability of efficient, durable and cost-effective (photo)electrochemical systems is still challenging. To address these limitations, many efforts are focused on the developpment and optimization of efficient (photo)electrocatalysts based on abundant materials and with the capacity to operate for long periods of time under benign conditions.

With this purpose, this doctoral thesis aims at studying the implementation of non-critical materials as catalysts for (photo)electrochemical conversion reactions of interest. The main contributions of this thesis are:

- The optimization of a simple, cost-effective, and eco-friendly synthetic route for preparing $Cu_{2-x}S$ electrocatalysts for H_2 evolution, working under moderate pH conditions, with Faradaic efficiencies close to 100%. Additionally, these catalysts demonstrate unprecedented durability of nearly one month, under continuous operation.

- The investigation of the electrochemical reduction of carbon dioxide (CO_2) with the $Cu_{2-x}S$ electrodes, including strategies to maximize the selectivity toward formate production.

- A comprehensive electrochemical, structural, and morphological characterization, including *operando* SEC and EIS, *ex-situ* XPS, XRD, and XANES, and in-situ Raman and XRD, to identify the catalytically active species involved in both, HER and CO_2ER.

- The implementation of selective contact engineering strategies for the development of versatile switchable photoelectrodes based on heterostructured inorganic halide perovskite $CsPbBr_3$ nanocrystals for organic transformations.

Resum

Per a fer front a la problemàtica dels models energètics tradicionals basats en el consum de carboni, es requereix d'una imminent implementació de nous models energètics nets i sostenibles. Amb aquest fi, és fonamental la generació i emmagatzematge d'energies renovables. En aquest context, els sistemes (foto)electroquímics impulsats per fonts d'energies renovables han sorgit com una tecnologia capaç d'emmagatzemar aquestes energies en enllaços químics. No obstant, la implementació dels sistemes (foto)electroquímics a gran escala encara presenta alguns reptes. Molts esforços es centren en l'estudi i optimització de catalitzadors eficients, basats en materials abundants i capaços d'operar per llargs períodes de temps.

Amb aquest propòsit, la present tesi doctoral té com a objectiu l'estudi de materials sostenibles com a catalitzadors de reaccions de conversió (foto)electroquímiques. Les principals aportacions d'aquesta tesi són:

- L'optimització d'un mètode sintètic senzill, econòmic i respectuós amb el medi ambient per a l'obtenció d'electrocatalitzadors de $Cu_{2-x}S$ altament eficients per a l'evolució d'hidrogen (H_2) en condicions moderades de pH. A més, el catalitzador mostra una durabilitat sense precedents de quasi un mes en continua reacció.

- També s'estudia la reducció electroquímica de diòxid de carboni (CO_2) amb l'electrocatalitzador de $Cu_{2-x}S$ i es reporten estratègies per a duplicar la selectivitat d'aquest per a la producció de fòrmic.

- Un estudi complet de mesures de caracterització electroquímica, estructural i morfològica incloent *operando SEC* i *EIS*, *ex-situ XPS*, *XRD* i *XANES* i *in-situ Raman* i *XRD* per a investigar les especies catalíticament actives involucrades en les reaccions de generació d'hidrogen i de reducció de diòxid de carboni.

- Tanmateix, s'ha implementat una enginyeria de contactes selectius per al desenvolupament de fotoelectrodes heteroestructurats amb pel·lícules de $CsPbBr_3$ NCs per a dur a terme transformacions orgániques.

Resumen

Para hacer frente a la crisis energética derivada de los modelos energéticos tradicionales basados en el consumo de carbono, se requiere una inmediata implementación de nuevas formas de energía limpia y sostenible. Para este fin, es fundamental la generación y almacenamiento de energías renovables. En este contexto surgen los sistemas (foto)electroquímcos, los cuales conectados a fuentes de energía renovables constituyen una tecnología capaz de almacenar dicha energía en forma de enlaces químicos. Sin embargo, la implementación a gran escala de estos sistemas (foto)electroquímicos aún presenta varios retos. Muchos esfuerzos se centran en el estudio y optimización de catalizadores eficientes, basados en materiales abundantes y aptos para operar por largos periodos de tiempo.

- Con este propósito, la presente tesis doctoral se fija como objetivo el estudio de materiales sostenibles usados como catalizadores para reacciones de conversión (foto)electroquímica. Las principales aportaciones de esta tesis son:

- La optimización de un método sintético sencillo, económico y respetuoso con el medio ambiente para la obtención de electrodos de $Cu_{2-x}S$ altamente eficientes para la evolución de hidrógeno (H_2) en condiciones moderadas de pH. Además, este catalizador de cobre muestra una durabilidad sin precedentes por casi un mes de operación.

- Se estudia la reducción electroquímica de dióxido de carbono (CO_2) mediante el uso del electrocatalizador de $Cu_{2-x}S$. Así mismo se reportan estrategias para duplicar la selectividad de dicho catalizador para la producción de fórmico.

- Se desarrolla un estudio completo técnicas de caracterización composicional, estructural y electroquímica el cual incluye *operando SEC* y *EIS*, *ex-situ XPS*, *XRD* y *XANES* e *in-situ Raman* y *XRD* que permite identificar las especies catalíticamente activas involucradas en la reacción de generación de H_2 y reducción de CO_2.

- Se implementa una ingeniería de contactos selectivos para el desarrollo de fotoelectrodos heteroestructurados de perovskita $CsPbBr_3$ NCs para llevar a cabo trasformaciones orgánicas

List of acronyms, abbreviations and symbols

A	Absorbance
AFM	Atomic Force Microscopy
E_g	Band gap energy
E_c	Conduction band energy
E_v	Valence band energy
CO_2ER	Electrochemical carbon dioxide reduction
CA	Chronoamperometry
CP	Chronopotentiometry
CTEM	Conventional Transmission Electron Microscopy
j-V	Current density-voltage
CE	Counter electrode
CV	Cyclic voltammetry
e^-	Electrons
EDS, EDX, or EDXS	Energy Dispersive X-Ray Spectroscopy
EELS	Electron energy loss spectroscopy
E_F	Fermi level
$E_{F,n}$	Electron quasi-Fermi level
$E_{F,p}$	Hole quasi-Fermi level

Ek	Kinetic energy
GC	Gas chromatography
GIXRD	Grazing beam X-ray diffraction
h^+	Holes
HAADF	High-angle annular dark-field
HER	Hydrogen evolution reaction
HRTEM	High-resolution Transmission Electron Microscopy
IS	Impedance spectroscopy
ISC	Intersystem crossing
I	Outgoing light intensity
I_0	Incident light intensity
LSV	Linear sweep voltammetry
NCs	Nanocrystals
OCP	Open circuit potential
PL	Photoluminescence
PV	Photovoltaic
RE	Reference electrode
Q	Electric charge

Rpm	Revolutions per minute
SCIC	Servei Central d'Instrumentació Científica
SCL	Space charge layer
SEM	Scanning Electron Microscopy
TCD	Thermal conductivity detectors
TRPL	Time resolved photoluminescence
UV-Vis	Ultraviolet-visible light
V_{oc}	Open-circuit voltage
W	Depletion width
XPS	X-Ray Photoelectron Spectroscopy
XRD	X-Ray diffraction
Z	Impedance
n_i	Moles
ω	Frequency
ϕ	Work function

Table of contents

Chapter 1

Introduction

With the economic, social and technological transformation that the Industrial Revolution entailed in the second half of the 18th century, society greatly changed the way they consume energy. Burning fossil fuels, including coal, oil, and natural gas, was stablished as the main energy source releasing large amounts of greenhouse gases (GHG) such as CO_2 during the process. The Energy Institute (EI) published in its 2023 Statistical Review of World Energy[1] the global primary energy consumption by source between 1800-2022, shown in **Figure 1.1**. After more than 200 years of industrial era, traditional biomass consumption remains constant while fossil fuels consumption has exponentially increased in parallel with energy demand and it was not until recent decades that other energy sources have been integrated.

Specifically, since 1950, the consumption of fossil fuels and subsequent CO_2 emissions increased around 7 times, reaching record levels in 2022 (**Figure 1.1, bottom**). The EI reported that the CO_2 emissions from energy consumption, which represent 87% of total global emissions, reached a record high of 39.3 billion tons of CO_2 equivalent, representing a 0.8% increase over 2021.

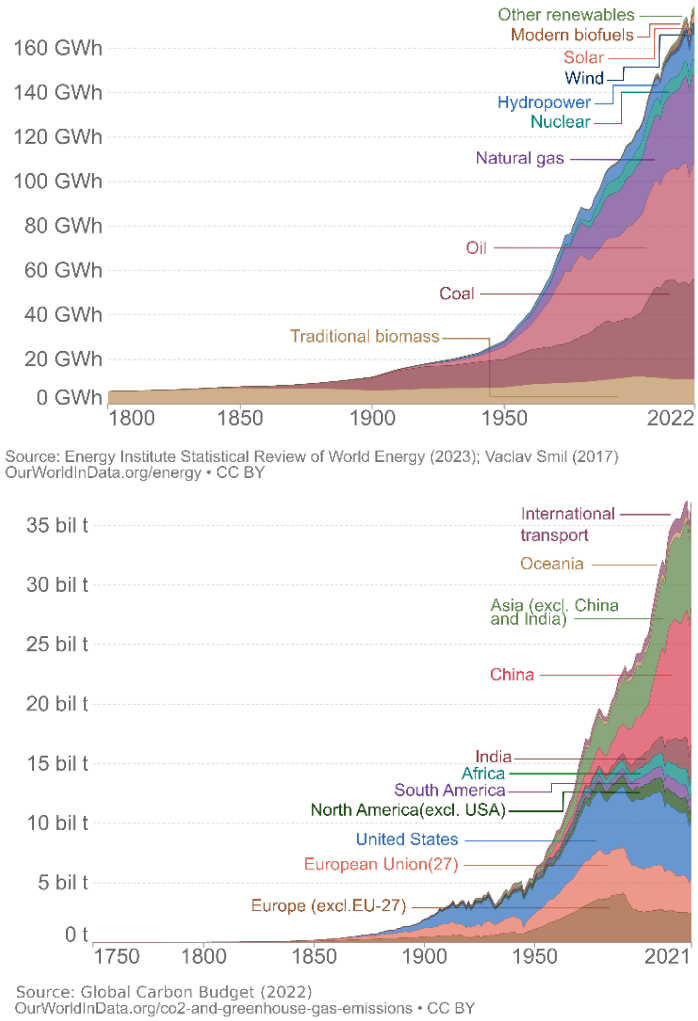

Figure 1.1. Global primary energy consumprion by source[1] (above) and annual total CO_2 emissions, by world region[2] (below).

Large amounts of CO_2 in the atmosphere are directly related to the increase in temperature on the Earth's surface, which results in extreme heat waves, rising sea levels, ocean acidification, changes in precipitation, resulting in flooding and droughts or intense hurricanes.[3] The European Union-funded Copernicus Climate Change Service (C3S) implemented by the European Centre for Medium-Range Weather Forecasts (ECMWF) reported in September 2023 that

Earth just had its hottest three months on record, while global sea surface temperatures are at unprecedented height for the third consecutive month and Antarctic sea ice extent remains at a record low for the time of year. August 2023 was the hottest August on record (estimated to have been around 1.5 °C warmer than the preindustrial average for 1850-1900, according to the C3S monthly climate bulletin)[4] and the second hottest ever month after July 2023.

Human activity has unequivocally caused global warming and limiting these devastating events requires economic and social transformation towards net zero CO_2 emissions. To address this crisis, international treaties on climate change such as the Paris Agreement were established with the overarching goal of keeping the global average temperature increase below 2 °C above pre-industrial levels and pursue efforts to limit the temperature increase to 1.5 °C.[5] Since 2020, each country has been submitting their national climate pledges, known as nationally determined contributions (NDCs) for achieving the Paris Agreement goals.

The Intergovernmental Panel on Climate Change (IPCC) published in the annual Climate Change 2023 report four types of assessed modelled global emissions modelled pathways over 2015–2050 (in **Figure 1.2**).[3] This alarming projection warns that a rapid, deep and immediate reduction of GHG emissions is required for limiting global warming to 1.5 ºC and 2 ºC.

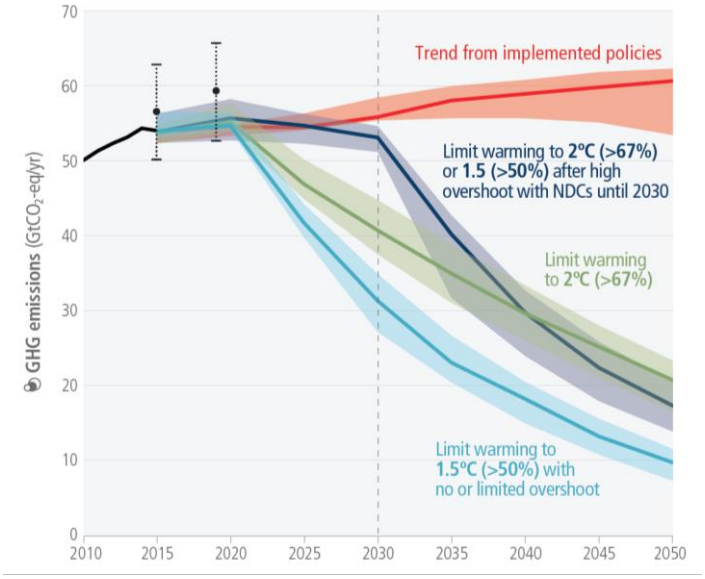

Figure 1.2. Global GHG emissions of modelled pathways by IPCC. In red, pathways with projected near-term GHG emissions in line with policies implemented until the end of 2020 and extended with comparable ambition levels beyond 2030. In dark blue, pathways with GHG emissions until 2030 associated with the implementation of NDCs announced prior to COP26, followed by accelerated emissions reductions likely to limit warming to 2 °C or to return warming to 1.5 °C with a probability of 50% or greater after high overshoot. In green, pathways that limit warming to 2 °C (>67%) with immediate action after 2020. And in light blue, pathways limiting warming to 1.5 °C with no or limited overshoot.

In this context, not only decarbonizing the energy sector, but also tackling other problems derived from the consumption of fossil fuels such as the exploitation of the soil and ecosystems alteration are necessary to mitigate global warming and to reach a more environmental awarded society. Therefore, a radical energy transition of the traditional energy model towards clean, sustainable and renewable energy sources is required.[6-7]

1.1 Energy transition and solar power

The energy transition towards energy sources environmentally and economically viable must be strategically designed to guarantee sustainability (the use of renewable inputs). Some alternatives to the use of fossil fuels such as

nuclear energy were already incorporated into the energy landscape at the end of the 20th century. However, nuclear energy would not be convenient to replace fossil fuels, since it encompasses the use of exhaustible energy sources (such as uranium) and generates radioactive waste. Alternatively, renewable energies such as sunlight, wind, hydropower, geothermal, wave or biomass represent abundant resources, free of greenhouse gases or radioactive waste. Among all the renewables, solar energy is considered the best option, since the sun is the most abundant source of energy, generating approximately 173,000 terawatts of solar power reaching the surface of the Earth, more than 10,000 times the world's total energy use.[8] Moreover, solar installations can be located on a wide variety of surfaces in few months compared to other energy plants. By carefully selecting the installation location, its environmental impact and the effect on the local wildlife is practically zero.[9-10]

The **Figure 1.3** compares the annual energy generation potential of the most common renewables versus traditional fossil fuels. It is apparent from the figure that the sun is the best candidate, inexhaustible and free of GHG emissions at the point of use.

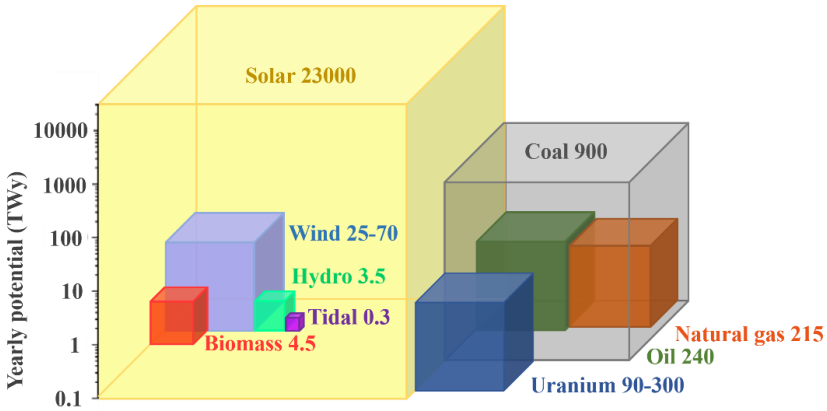

Figure 1.3. **C**omparison of the yearly potential of some renewable energy sources[11] on the left and non-renewable energy sources on the right[12] in a logarithmic scale.

Solar energy has been largely utilized through solar thermal and photovoltaics (PV) to produce thermal energy and electricity, respectively. Photovoltaics is a promising field, which has attracted the interest of the research community in the last century, focused on designing efficient PV cells with sustainable materials.[13] However, one of the main drawbacks of solar energy relates to its intermittency and seasonality. Inspired, but not constrained, by natural photosynthesis, solar-to-fuels or to value-added products (artificial photosynthesis) holds the promise of efficient harnessing of solar energy through energy storage in chemical bonds, and consequently the sustainable production of dense and transportable fuels/chemicals.[14-17]

1.2 From natural to artificial photosynthesis

During natural photosynthesis, schematized in **Figure 1.4**, green plants and photosynthetic organisms can convert light into chemical energy in the form of sugars. First, solar energy is absorbed in a functional and structural unit of protein complexes located at the chloroplasts called photosystem II (PSII), where the antenna molecule chlorophyll P680 is excited. Subsequently, charge carrier separation takes place leading to two consecutive processes: the water oxidation reaction and electron transfer to the photosystem I (PSI). Water oxidation in acidic/neutral conditions entails the conversion of water (H_2O) into molecular oxygen (O_2) and protons (H^+) according to the equation (1.1):

$$2\ H_2O \rightarrow 4\ H^+ + 4\ e^- + O_2 \qquad (1.1)$$

Electrons are transferred from PSII to PSI through an electron transport chain. When the electrons reach PSI, another light absorption process takes place on the Chlorophyll P700. The excited electrons are transported to $NADP^+$ reductase protein, synthetizing two high energy molecules: Nicotinamide adenine

dinucleotide phosphate (NADPH) and adenosine triphosphate (ATP), which participates in the Calvin cycle, where CO_2 fixation takes place.

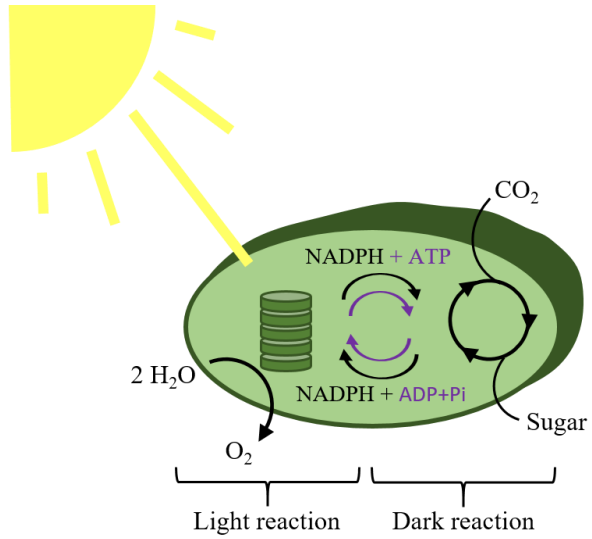

Figure 1.4. Simplified scheme of the natural photosynthesis process inside a chloroplast, where light-dependent processes and light-independent reactions or dark reactions are represented from left to right.

In the same way that photosynthetic organisms use the energy provided by the sun to oxidize water and reduce CO_2 into high energy chemicals, artificial photosynthetic systems, such as photocatalytic systems (PC), photoelectrochemical (PEC) systems or electrochemical systems coupled to photovoltaic cells (PV-EC) are capable of storing solar energy in high energy density chemicals. In addition to the water oxidation reaction, other oxidation reactions of interest can be addressed, such as wastewater treatment[18-19], oxidation of organic compounds[20-21] and biomass oxidation[22-23] to decontaminate and to produce fuels and value-added chemicals. Otherwise, important photoelectrochemical reduction reactions additionally to CO_2 fixation[24-25] such as H_2 generation[26-27] or nitrogen reduction,[28-29] can be performed by (photo)electrochemical systems.[30]

In this PhD thesis, both electrochemical and photoelectrochemical systems have been used to perform oxidation and reduction reactions of wide technological and industrial interest. Electrochemical and photoelectrochemical systems and the materials involved are introduced in the following sections.

1.3 Electrochemical systems

Electrochemical (EC) systems can store energy as chemical bonds *via* redox reactions. Redox or oxidation-reduction reactions involve electrons (e^-) transfer to form a molecule or ion by changing its oxidation state. Redox reactions necessarily involve two simultaneous half-reactions: one species accepts electrons and is reduced (*reduction*) while another species releases electrons and gets oxidized (*oxidation*):

$$Ox_1 + Red_2 \rightarrow Red_1 + Ox_2 \qquad \text{Global reaction}$$

$$Red_2 \rightarrow Ox_2 + n\,e^- \qquad \text{Oxidation half-reaction}$$

$$Ox_1 + n\,e^- \rightarrow Red_1 \qquad \text{Reduction half-reaction}$$

Two electrodes are required to mediate the electron transfer in each half-reaction. Both electrodes arranged in an electrochemical cell (schematized in **Figure 1.5**), are connected to an external electrical source, which provides the energy input. When the electrical source is a photovoltaic cell, the system can be considered as an artificial photosynthetic process. However, another renewable electricity source (wind, hydropower, amongst others) coupled to an electrochemical cell can also provide a sustainable electrosynthetic system.

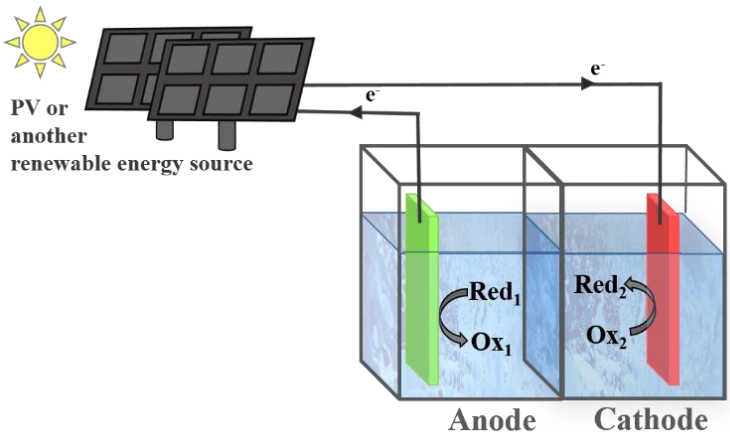

Figure 1.5. Schematic representation of an EC cell coupled to a PV system or other renewable electricity source. The cell is integrated by an anode and a cathode, where the oxidation and the reduction half-reactions occur, respectively. The electrode that mediates the oxidation is the anode and the electrode that mediates the reduction is the cathode.

On the one hand, the electrode where the *oxidation* takes place is termed the anode. The molecule of interest present in the electrolyte is oxidized at this electrode by losing electrons in the process. On the other hand, the electrode where the *reduction* takes place is termed the cathode. The species present in the electrolyte accepts electrons from this electrode and is reduced. These electrodes operate as catalysts, since the electrochemical conversion takes place on the electrode surface, accelerating chemical reactions without being consumed during the process; specifically, the catalyst that participates in electrochemical reactions are called *electrocatalysts*.

1.3.1 Electrocatalytic materials

When defining a good electrocatalyst, some aspects such as earth-abundance, electronic conductivity, activity, selectivity, cost and durability are important.[31] Traditionally, metal and metal-based materials such as metal oxides or metal chalcogenides have been used as electrocatalysts.[32] Some examples of the most efficient electrocatalysts in acid/neutral media are the noble metals Pt and Ru

although other cost-effective and Earth abundant materials such as transition metals have been explored. Depending on the specific properties of each metal or metal-based electrocatalyst (coordination, crystalline facet, structure) the material is selective for a particular reaction product. A rational design of the electrocatalyst is crucial for boosting the efficiency of electrocatalytic reactions.[33]

Two different electrochemical reactions were studied during this thesis: hydrogen evolution reaction (HER) and carbon dioxide reduction (CO_2RR). In the following sections both reactions are introduced, including their fundamentals and the state-of-the-art electrocatalysts.

1.3.2 Hydrogen production

Hydrogen, which is the most abundant chemical substance in the universe, is an energy carrier with a high gravimetric energy density, about 143 *MJ/kg*. This value represents more than three times the energy content per mass compared to gasoline (46.4 *MJ/kg*), which implies that, H_2 possesses the highest energy density per mass of any fuel.[34-35] Contrary to fossil fuels, the use of hydrogen as an energy vector considerably reduces environmental impact. These outstanding features highlight H_2 as a promising alternative to fossil fuels, capable of providing high amounts of energy with net-zero CO_2 emissions, combating climate change. Moreover, it is also used in other sectors as a chemical feedstock, heat source, refining of metals or converted to electricity through fuel cells.[36]

However, there are some challenges to overcome when hydrogen is used as an energy carrier. Since hydrogen gas has much lower volumetric density than most fossil fuels (H_2 has a volumetric energy density of 12.7 MJ m^{-3} compared to 40.0 MJ m^{-3} for natural gas at similar temperature and pressure), large volumes/pressures are needed for its storage.[37-38] Liquefied hydrogen could

improve this, but affecting both energy and infrastructure costs. Nevertheless, on the other hand, hydrogen possesses higher volumetric energy density compared to batteries, and its advantages are significant enough to consider it a promising alternative in terms of energy demand and sustainability.

Different approaches are used to produce hydrogen by utilizing a wide range of methods or directly extracting it from a variety of materials and compounds in the nature. Whilst H_2 is a colourless gas, there is a colour code used within the energy industry to differentiate the methods by which H_2 is obtained. The most common colours reported are grey, green, and blue hydrogen. Grey hydrogen is assigned to the hydrogen produced from natural gas, or methane, through steam methane reforming. Blue hydrogen is essentially the same as grey hydrogen, but including the use of carbon capture and storage (CCS) to trap and store this CO_2. Green hydrogen is the actual alternative to face climate change since no GHG emissions are generated during the hydrogen production process. Large-scale low-emissions hydrogen production plants are being implemented in many countries around the world and can grow enormously by 2030 according to data reported in Global Hydrogen Review 2023 of the IEA.[39] **Figure 1.6** shows the world map of the annually planned low-emissions hydrogen production projects. The EU is clearly leading the race towards setting a comprehensive framework and policy support for clean hydrogen. The annual production of low-emission hydrogen could reach 38 *Mt* in 2030, if all announced projects are completed. However, cost issues are hampering large-scale implementation.

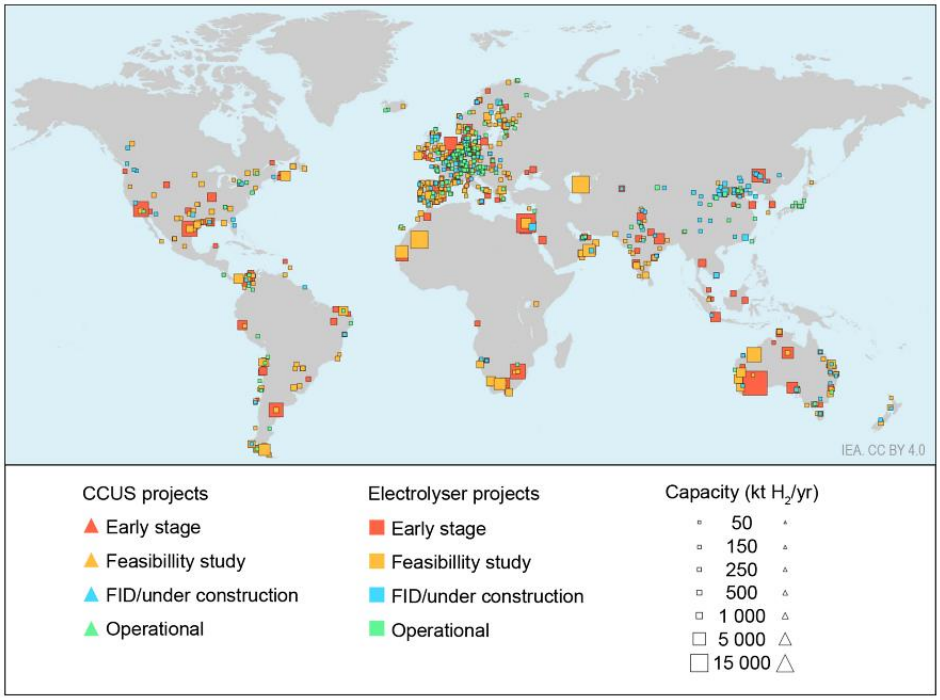

Figure 1.6. Map of planned low-emissions hydrogen production projects from IEA.[39]

Green hydrogen is produced from the electrolysis of water assisted by renewable energy sources, such as solar or wind power.[40] Water electrolysis, or water splitting refers to the electrochemical reaction to split the water molecule into its components of hydrogen (H_2) and oxygen (O_2). It consists of electrodissociation of the water molecule: water is oxidized at the positively charged electrode (anode) to oxygen, releasing protons in the process, while positively charged hydrogen ions migrate to the negatively charged electrode (cathode) where it is reduced to molecular hydrogen, according to the scheme shown in **Figure 1.7**.

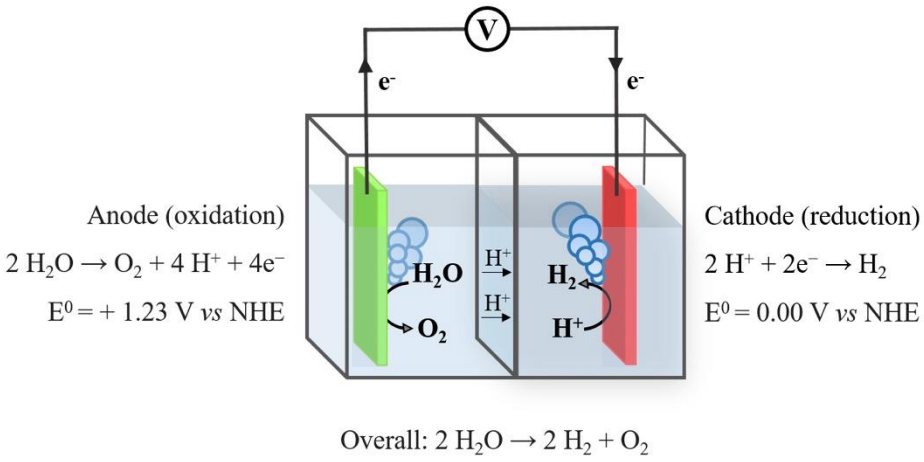

Figure 1.7. Scheme of a water electrolysis cell: water is oxidised to O_2 at the anode, releasing 4 H^+ which are reduced to 2 molecules of H_2 at the cathode.

Water electrolysis, when conducted at standard conditions is thermodynamically unfavourable, since its standard electrochemical cell potential: $E^0_{cell} = E^0_{cathode} - E^0_{anode}$ = -1.23 *V vs* NHE (expressed with respect to the normal hydrogen electrode -NHE-) is negative, which implies a positive Gibbs free energy (ΔG) of + 237 *KJ* mol^{-1} H_2, implying that water splitting is not a spontaneous reaction.[41-42] For this reason, an external bias/potential input is required, ideally electrical energy coming from solar energy (artificial photosynthesis) or other renewable energy source as mentioned above.[43]

Traditionally, precious metals such as Pt, Ru, Ir and their oxides have been the most used electrocatalysts for evolving hydrogen. Particularly, Pt-based cathodes remain the state-of-the-art electrocatalysts for HER owing to their high efficiency, stability and high current densities.[44-47] However, Pt-based cathodes have some important drawbacks, related to their scarcity and high cost. Furthermore they also present limitations regarding the reaction medium, since the HER on the Pt surface displays distinct pH dependent kinetics, being highly efficient only in acidic media.[48]. Therefore, scaling-up green H_2 production

requires materials that *(i)* are highly efficient electrocatalysts, *(ii)* exhibit long-term durability, *(iii)* are based on Earth-abundant elements, *(iv)* implies low-cost and environmental friendly manufacturing techniques, and *(v)* are operative under more sustainable mild pH conditions.[49-50] More recently, electrocatalyst based on Earth-abundant and cost-effective materials such as Co[51], Mo[52-53], Fe[54] or Cu[55-56] have been reported with remarkable efficiencies toward HER performance highlighting Ni-based electrocatalysts for alkaline HER[57-59]. Particularly, Cu-based electrocatalysts are attracting attention, since Cu possesses multiple oxidation states, good redox kinetics and rich coordination chemistry.[60] It has been suggested that HER performance of Cu atoms is enhanced when coordinated with different chalcogen atoms (S, Se, and Te), since it is believed that the increase in covalency and declination of electronegativity favors the superior HER.[61]

In this thesis, a copper sulfide ($Cu_{2-x}S$) electrocatalyst was synthetized and characterized in *Chapter 3* for hydrogen production. *Chapter 4* describes all the electrochemical procedures and mechanistic analysis during HER. The $Cu_{2-x}S$ cathode exhibits high current densities close to 400 $mA\ cm^{-2}$ with Faradaic efficiencies near 100% for HER and a remarkable durability of more than 1 month under continuous operation. These results represent a great progress in the race to scale-up green hydrogen production.

1.3.3 Carbon dioxide reduction

Many carbon dioxide fixation technologies are being explored not only to reduce anthropogenic CO_2 levels, but also to convert it into valuable chemicals.[62-64] Electrochemical CO_2 reduction powered by renewable electricity has received particular attention owing to its mild reaction conditions, simple experimental instruments and low temperature and pressure. Similarly to HER, CO_2 reduction

takes place at the cathode where the CO_2 molecule can be reduced to a wide variety of products (CO, CH_4, HCOOH, CH_3COOH, among others) while at the anode the oxidation half-reaction closes the electronic circuit. **Figure 1.8** shows an electrochemical cell powered by renewables for CO_2 reduction.

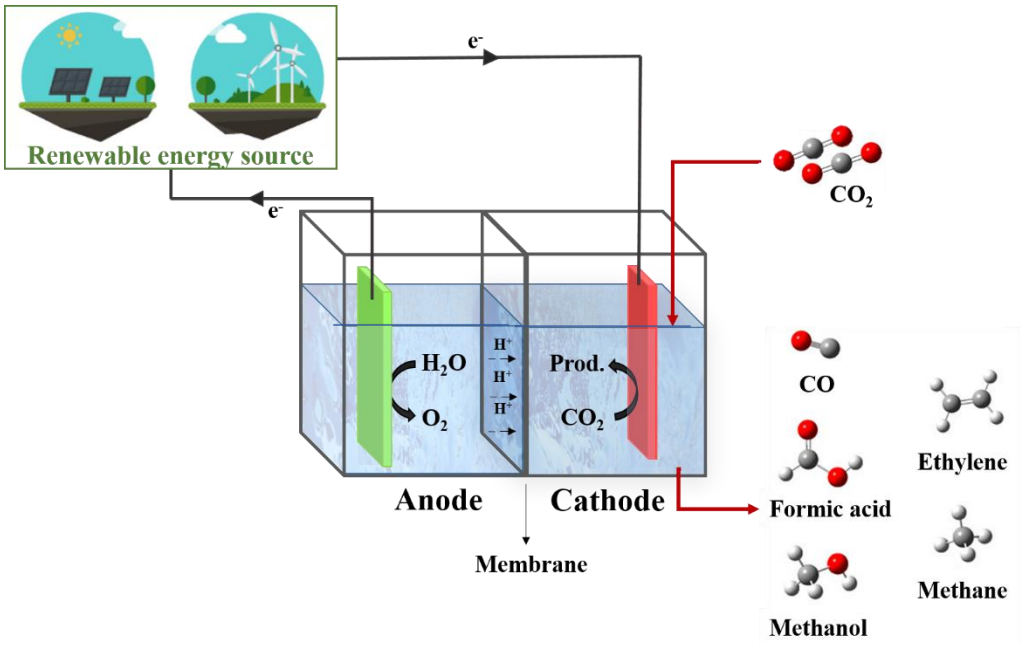

Figure 1.8. Representative scheme of an electrochemical cell powered by renewable energy source. Typically, a polymeric membrane is used for dividing both compartments to avoid cross-contamination.

Efficient CO_2 electrochemical reduction reaction (CO_2ER) is still challenging for the scientific community, due to its high overpotentials and poor selectivity since CO_2ER is a multielectron reaction and highly competitive with HER. Metallic electrocatalyst for CO_2ER are particularly attractive, due to their structural simplicity, easy handling and robustness. As pioneered Hori et al.,[65] copper is a promising catalyst able to reduce CO_2 to diverse C-products, including highly demanded C_{2+}-products. However, the selectivity and industrially-relevant production rate is still challenging and in this regard, various

Cu-based electrocatalysts including Cu alloy, Cu compound (Cu + non-metal), and supported Cu-based catalyst (Cu supported by carbon, metal oxides, or polymers) have been developed.[24, 66-68]

Transition metal sulphides (TMS) and specially Cu-S materials have been widely used as electrocatalysts for CO_2 reduction, due to their ability to control the formation of intermediate products and thus the reaction pathway.[69-71] Further approaches to enhance the reactivity and selectivity of Cu-derived electrocatalysts have been explored via controlling size, facets, morphology, composition, oxidation state or surface reconstruction.[72-77]

Chapter 5 focuses on the study of CO_2ER with nanoporous $Cu_{2-x}S$ electrocatalysts. Particular emphasis is given on determining rational strategies to enhance the electrocatalyst selectivity for carbon dioxide reduction over HER.

1.4 Phototelectrochemical systems

Photoelectrocatalysis is a powerful approach to convert solar energy into fuels or value-added chemicals.[78] In photoelectrochemical (PEC) cells, a photoactive material, capable of carrying out internal electronic transitions when irradiated with electromagnetic radiation, that is, with light, is deposited at one or both electrodes. Therefore, the deposited electrodes, photoanode and photocathode, directly drive the oxidation and the reduction half-reactions, respectively. When the system contains only one photoelectrode, an electrocatalytic material is used as counter electrode.

The first successful demonstration of photoelectrochemical (PEC) reactions was the PEC water splitting pioneered by Fujishima and Honda in 1972, which emerged as a promising approach for driving solar-to-H_2 conversion concurring with the first peak oil crisis. In their experiments, the oxidation of water to molecular oxygen was driven by a titanium dioxide (TiO_2) photoanode while

hydrogen was evolved on a Pt wire at the cathode.[79-80] Although photoelectrocatalysis is a promising method to achieve solar-to-chemical conversion, there are important kinetic bottlenecks, especially in the case of water oxidation due to its high thermodynamic requirement, number of electrons to be transferred and kinetic limitations.[81] Breaking the strong O-H bonds during water oxidation requires a significant amount of energy. This high energy barrier makes the process energetically demanding. Consequently, an external electric input is often needed to carry out the reaction. However, even if the thermodynamic potential is provided, the kinetics of the water oxidation reaction can be slow, leading to low reaction rates. This is often due to the multi-step nature of the process and the involvement of intermediate species.[82] Therefore, more favorable and chemically valuable oxidation reactions have been explored such as the oxidation of biomass or alcohols being eventually combined with the hydrogen production or other reduction reaction of interest such as CO_2.[83-86]

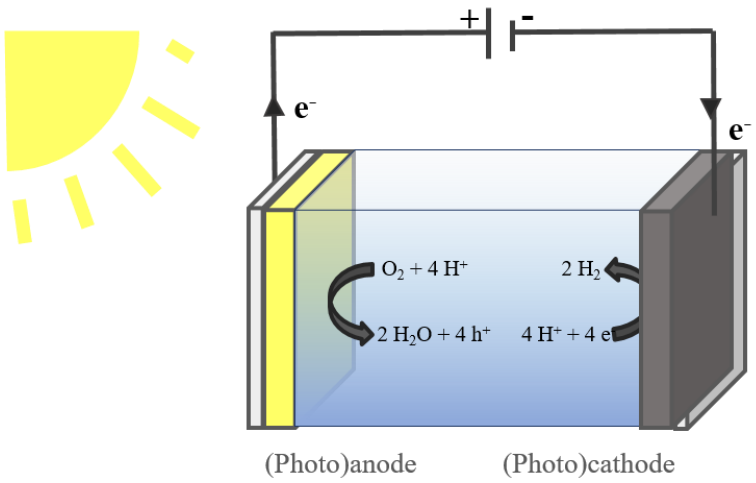

Figure 1.9. Schematic representation of a PEC water splitting cell. The electrode that mediates the water oxidation is the (photo)anode and the electrode that mediates the reduction is the (photo)cathode. Note that, the photo-absorber material is supported on transparent electrodes/substrate to allow light transmission.

The selected photoelectrode for PEC applications is a crucial component that plays a key role in converting light energy into chemical energy. The photoelectrode is typically made of a semiconductor material that ideally has a bandgap matching the energy of the incident light. The next section addresses the operation principles of light-absorber semiconductor materials in solid/liquid interfaces for photoelectrochemical reactions.

1.4.1 Semiconductor materials

Semiconductors are materials with an electrical conductivity value halfway between a conductor and an insulator, due to their characteristic valence band edge of energy E_V and conduction band edge of energy E_C positions. The energy difference between the E_C and the E_V, is the band gap energy E_g ($E_g = E_C - E_V$). A material is typically considered semi-conducting when its band gap is lower than ~4 eV. This peculiarity confers them exceptional electrical and optical properties that make semiconductors suitable materials for various technological applications. Furthermore, their fundamental properties are directly related with efficient light harvesting and subsequent solar to chemical energy conversion.

Additionally, the Fermi level (E_F) is a fundamental concept to understanding the electrical properties of a semiconductor. E_F is defined as the energy corresponding to a 50% probability of electron occupancy in a conducting material, or as the energy of the highest occupied state at absolute zero temperature.[87] Since this definition cannot be rigorously applied to a semiconductor (as E_F could potentially be associated with any energy level within the band gap), it is commonly recognized as the chemical potential for electrons. This chemical potential is defined as the alteration in free energy resulting from the introduction of one electron to the system.

Suitable semiconductor materials used as photoanodes and photocathodes ideally integrate these three main processes*: (i) light absorption, (ii) charge separation* and *(iii) chemical reaction.*

(i) **Light absorption.** The first step in a photoelectrochemical system involves the absorption of light by a photoactive material forming the photoelectrode. When an electromagnetic radiation from sunlight o simulated sunlight strikes onto the photoelectrode, the photoactive material absorbs the incident photons and undergoes an internal electron excitation process (photoexcitation). If the absorbed photons are energetic enough, electrons from the valence band are promoted to the conduction band leaving behind a positively charged hole in the valence band creating electron-hole pairs.

(ii) **Charge separation**. Once the electron-hole pairs are generated through light absorption, the next step is the charge separation. The electrons in the conduction band and the holes in the valence band need to be spatially separated to prevent recombination, which would result in the loss of photo-generated charge carriers.

(iii) **Chemical reaction.** The separated electrons and holes, after reaching the photoelectrode surface, are then involved in a chemical reduction and oxidation reactions, respectively, also commonly referred to as electron transfer process.

Semiconductor materials can be classified as: intrinsic and extrinsic. On the one hand, intrinsic or pure semiconductor materials are those whose impurities do not appreciably affect their electrical behavior. At absolute zero temperature, the Fermi level in an intrinsic semiconductor lies midway between the valence and

conduction bands. As a result, the concentration of holes and electrons is equal in an intrinsic/undoped semiconductor. On the other hand, extrinsic semiconductor materials are tuned to modify their electrical properties by introducing selected impurity atoms through highly controlled doping methods.[88] The doping process introduces foreign atoms into the crystal lattice, leading to the creation of donor or acceptor levels within the band gap. In an extrinsic semiconductor material majority and minority charge carriers can be defined. Extrinsic semiconductors can be classified as n-type semiconductors or p-type semiconductors referring to the majority negative and positive charge carriers, respectively. N-type semiconductors are used as photoanodes and p-type semiconductors as photocathodes.[89] The physical chemistry of the semiconductor/liquid interface in a PEC cell is described below and depicted in **Figure 1.10.**

When an n-type semiconductor material is brought into contact with the liquid solution containing the redox pair of interest, the electrolyte, electrons (majority carriers) flow from the semiconductor to the electrolyte to equilibrate the Fermi level of the semiconductor with the redox potential of the electrolyte (**Figure 1.10a** and **Figure 1.10b**). As a result, the Fermi level moves toward more positive potentials. The decrease of the electron density near the surface leads to the formation of a space charge layer (SCL) also known as depletion layer at the semiconductor/electrolyte interface. The width of the depletion region (*W*) is the distance over which the mobile charge carriers are depleted. *W* is influenced by factors such as the doping concentration of the semiconductor, the illumination or the applied voltage across the junction. At the surface of the n-type semiconductor, an accumulation of positive charges is generated, whereas negative charges are accumulated over a much narrower region known as

Helmholtz layer (H_L) of width W_{HL} in the solution, close to the electrode generating an electric field across the SCL.

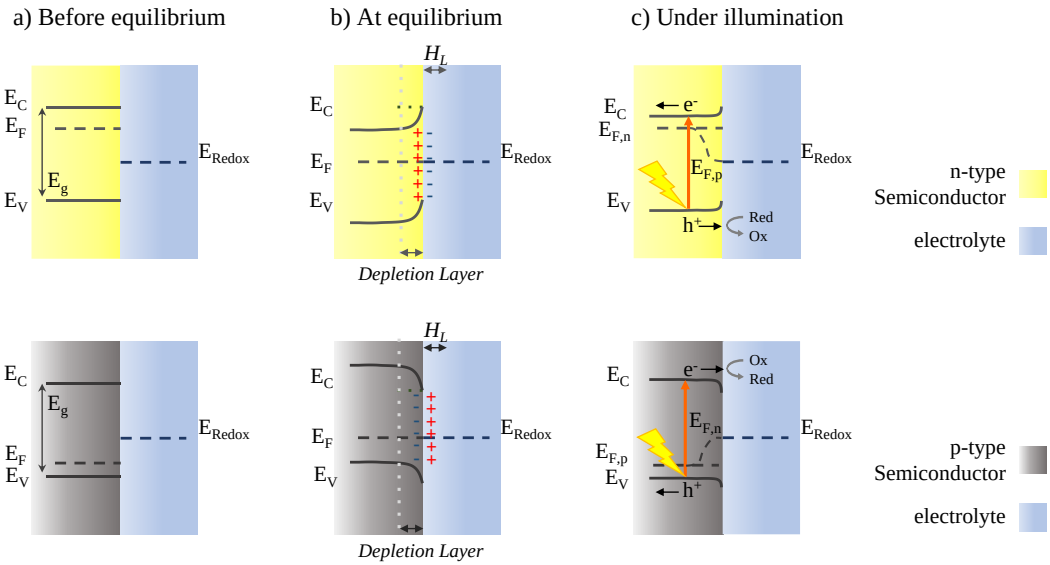

Figure 1.10. Energy band diagrams for an n-type semiconductor/electrolyte interface contact (top) and a p-type semiconductor/electrolyte interface contact from left to right: before equilibration, after equilibration in the dark conditions and in quasi-static equilibrium under steady state illumination.

Under steady state illumination, photons more energetic than the semiconductor bandgap promote the generation of electron-hole pairs. The electric field developed in the quasi-static equilibrium with the redox couple in the electrolyte promotes the band bending effect. Consequently, the photogenerated free minority charge carriers, holes (h^+), move to the surface of the photoelectrode to drive the oxidation reaction and directs electrons away from the surface. Since the photogenerated holes can accept electrons from the electrolyte species (carrying out the oxidation reaction), an electron flow takes place, producing a photocurrent which depends on the generation, collection, and reaction rates.[90] Since n-type semiconductor materials are capable to drive oxidation reactions, they are typically used as photoanodes. Note that under steady-state illumination,

the electron and hole populations are perturbed compared to the dark situation, and consequently the Fermi level splits into electron quasi-Fermi level ($E_{F,n}$) and hole quasi-Fermi level ($E_{F,p}$).[59, 91] The difference between the electron and hole quasi-Fermi levels at net zero current flow is described as the open-circuit voltage (V_{oc}) or open circuit potential (OCP) and can be measured experimentally providing information about the energetics of the material and the system.[92]

Analogous situation takes place when a p-type semiconductor material, commonly used as photocathode, comes into contact with an electrolyte. In this case, holes are the majority carriers and electrons flow from the electrolyte to the E_V for balancing the Fermi level of the semiconductor with the E_{redox} of the electrolyte. Hence, the electrode surface accumulates negative charges, while at the solution, an excess of positive charge is accumulated forming the H_L. A drop of the generated electric field results in a band bending effect, opposite of that of n-type semiconductor. Upon illumination (**Figure 1.10c bottom**), photogenerated electrons (free minority charge carriers) move favorably towards the interface with the electrolyte, enabling reduction reactions.

The performance of the photoelectrodes is commonly evaluated by measuring their (photo)current-potential response or j-V curve (described in *Section 2.3*). **Figure 1.11** shows a simplified j-V curve, obtained when the photoelectrode current response is measured while sweeping a potential range in dark conditions (dark current j_{dark}) and under illumination (photocurrent, j_{ph}). The third green dashed curve in **Figure 1.11** corresponds to the ideal photocurrent (j_G) described by the Gärtner model[93]. The Gartner model for the estimation of photocurrent consists in calculating the total photocurrent as the sum of all carriers photogenerated within the depletion region plus those generated in the bulk which are able to diffuse to the depletion region. Note that, especially under low bias conditions, both the ideal (green) and the experimental (blue) photocurrent

behave differently. This is mainly due to electron-hole recombination, which occurs at the SCL or at the photoelectrode surface. Consequently, the photogenerated carriers are lost before they can mediate in the oxidation and reduction reaction.[90]

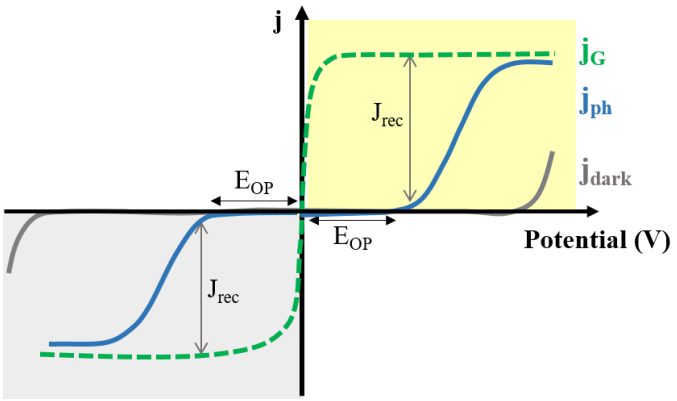

Figure 1.11. Schematic representation of a typical current-voltage plot for photoanode (shaded in yellow) and for a photocathode (shaded in gray). The j_{dark} (solid gray line) is the dark current density, j_{ph} (solid blue line) is the experimental photocurrent density and j_G (dashed green line) is the ideal photocurrent density. The difference between j_G and j_{ph} gives the recombination current density, j_{rec}.

One of the main challenges in PEC relates to the selection of the suitable semiconductor materials to be used as photoelectrodes. The oxidation or reduction reaction to be carried out and their redox potential are key to choose the semiconductor, since as described in **Figure 1.10**, the redox potential must be energetically located within the band gap of the semiconductor: the E_V must lay well below the E_{ox} for oxidation and the E_C must display higher than the E_{red} for reduction reactions.

Traditionally, metal oxides (MO_x) have been deposited on transparent electrodes/substrates and used as photoanodes and photocathodes, due to their tunable optoelectronic properties and Earth abundance. Some of the most commonly used metals for MO_x are Fe, Zn, Ti, Sn, Cu, Mo or W, which can drive different reactions, such as hydrogen production via water splitting,[94] CO_2

reduction reaction,[95] pollutant degradation reaction,[96] or anti-microbial applications.[97]

- *Metal halide perovskite*

Metal halide semiconductor materials presenting the perovskite-type crystal structure (ABX_3), especially those that Pb sits in the B site and I, Br, or Cl in the X site (**Figure 1.12**), have attracted increasing attention in the last years due to their high performance in photovoltaic devices,[98] lasing[99] and light emission[100-101]. Furthermore, owing to their excellent optical and photoelectric properties, cost-effective, simple synthesis method and their halide-dependent tuneable bandgaps, these promising semiconductor materials are emerging in other applications such as PC and PEC.[102] However, halide perovskite materials have some limitations that currently hinder their efficiency, such as the high oxidative instability.[103-104] To address the stability issue, several strategies including compositional modifications, dynamic control of the crystallization process, surface passivation or encapsulation strategies, have been adopted.[105-106] Shape-controlled synthesis of perovskite nanocrystals enables accurate control over the particle size and size distribution and the thermodynamic stability. The hot-injection method pioneered by Protesescu et al.[107] successfully allows to shape-control the synthesis of the nanoparticles (NCs). This synthetic route was used in *Chapter 6* and described in *Section 2.1.3* to synthetize the $CsPbBr_3$ NCs.[108]

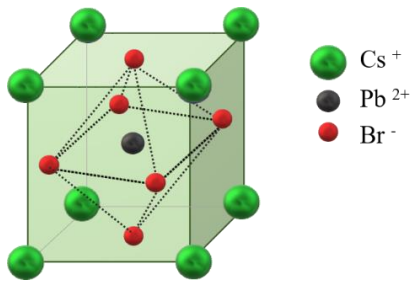

Figure 1.12. Schematic representation of the cubic $CsPbBr_3$ inorganic perovskites crystal structure synthetized in this thesis in *Chapter 6*.

1.4.2 Heterostructures

Several strategies have been investigated in the field of materials science with the aim of enhancing the efficiency of photoelectrodes. Controlling the particle size, introducing dopants, depositing surface co-catalysts or combining two or more semiconductors to form heterostructured photoelectrodes are some of the most used methodologies to boost the PEC performance on the photoelectrode.[109-111]

The rational design of complex architectures such as heterostructuring with different semiconductor materials has emerged as a useful engineering approach to exploit synergistic interactions.[112-113] Combining materials with a favourable energy band alignment for charge separation creates an "energetic cascade", as illustrates **Figure 1.13**, which enhance the solar-to-chemical efficiency by preventing charge recombination.[114-117] For instance, a favourable band engineering results from combining a material with high surface area (host) and good conductivity with a highly dispersed visible light absorber material (guest).[112, 118]

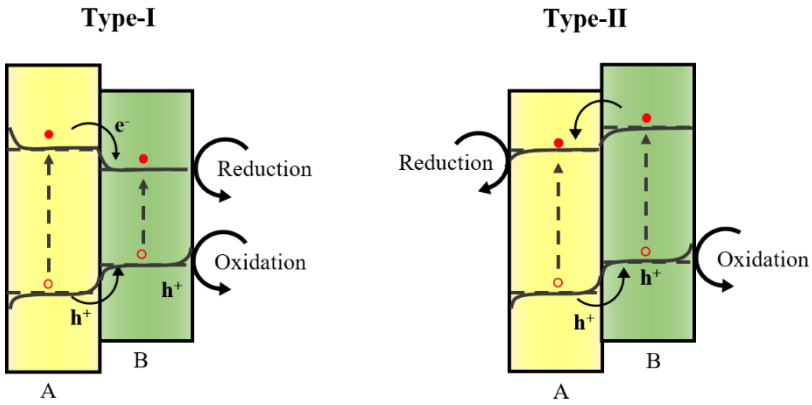

Figure 1.13. Representation of the type-I and type-II band alignments diagram in heterostructured photoelectrodes. The diagrams show possible charge transfer mechanisms throughout the heterojunctions.

In the development of this thesis, heterostructured photoanode and photocathode have been studied to demonstrate that the photoelectrochemical behaviour of inorganic halide perovskite nanocrystals ($CsPbBr_3$ NCs) can be tailored through engineering the selective contacts (e.g. hole and electron transporting layers) as underlayer. Specifically, two different MO_x were selected as underlayers: titanium oxide (TiO_2) and nickel oxide (NiO) as hole and electron transporting materials, respectively.

1.5 References

1. *Statistical Review of World Energy*; Energy Institute (IE): https://www.energyinst.org/statistical-review, 2023.
2. Friedlingstein, P.; O'Sullivan, M.; Jones, M. W.; Andrew, R. M.; Gregor, L.; Hauck, J.; Le Quéré, C.; Luijkx, I. T.; Olsen, A.; Peters, G. P., Global carbon budget 2022. *Earth System Science Data Discussions* **2022,** *2022*, 1-159.
3. *Climate Change 2023 report*; Intergovernmental Panel on Climate Change (IPCC) 2023.
4. ERA5. In *Copernicus Climate Change Service/ECMWF* https://cds.climate.copernicus.eu/cdsapp#!/software/app-c3s-monthly-climate-bulletin-explorer?tab=app, 2023.
5. Agreement, P. In *Paris agreement*, 2015; HeinOnline: p 2017.
6. Ediger, V. Ş., An integrated review and analysis of multi-energy transition from fossil fuels to renewables. *Energy Procedia* **2019,** *156*, 2-6.
7. Olabi, A. G.; Abdelkareem, M. A., Renewable energy and climate change. *Renewable and Sustainable Energy Reviews* **2022,** *158*, 112111.
8. US National Renewable Energy Laboratory Website (NREL). https://www.energy.gov/solar.
9. Kannan, N.; Vakeesan, D., Solar energy for future world:-A review. *Renewable and sustainable energy reviews* **2016,** *62*, 1092-1105.
10. Maka, A. O. M.; Alabid, J. M., Solar energy technology and its roles in sustainable development. *Clean Energy* **2022,** *6* (3), 476-483.
11. International Energy Agency. https://www.iea.org/data-and-statistics/data-browser/?country=WORLD&fuel=Energy%20consumption&indicator=CO2Industry.
12. *BP Statistical Review of World Energy 2018*; BP: 2018.
13. Gong, J.; Li, C.; Wasielewski, M. R., Advances in solar energy conversion. *Chemical Society Reviews* **2019,** *48* (7), 1862-1864.
14. Gust, D.; Moore, T. A.; Moore, A. L., Solar fuels via artificial photosynthesis. *Accounts of chemical research* **2009,** *42* (12), 1890-1898.
15. Qiu, B.; Du, M.; Ma, Y.; Zhu, Q.; Xing, M.; Zhang, J., Integration of redox cocatalysts for artificial photosynthesis. *Energy & Environmental Science* **2021,** *14* (10), 5260-5288.
16. Zhang, J. Z.; Reisner, E., Advancing photosystem II photoelectrochemistry for semi-artificial photosynthesis. *Nature Reviews Chemistry* **2020,** *4* (1), 6-21.
17. Ru Ng, A. Y.; Boruah, B.; Chin, K. F.; Modak, J. M.; Soo, H. S., Photoelectrochemical cells for artificial photosynthesis: alternatives to water oxidation. *ChemNanoMat* **2020,** *6* (2), 185-203.

18. Abdi, F. B.; Samuel, Z. A.; Debela, S. K.; Amibo, T. A., Wastewater treatment using a photoelectrochemical oxidation process for the coffee processing industry optimization of chemical oxygen demand (COD) removal using response surface methodology. *International Journal of Analytical Chemistry* **2022,** *2022*.
19. Pitchaimuthu, S.; Sridharan, K.; Nagarajan, S.; Ananthraj, S.; Robertson, P.; Kuehnel, M. F.; Irabien, Á.; Maroto-Valer, M., Solar Hydrogen Fuel Generation from Wastewater—Beyond Photoelectrochemical Water Splitting: A Perspective. *Energies* **2022,** *15* (19), 7399.
20. Tateno, H.; Chen, S.-Y.; Miseki, Y.; Nakajima, T.; Mochizuki, T.; Sayama, K., Photoelectrochemical oxidation of glycerol to dihydroxyacetone over an acid-resistant Ta: BiVO4 photoanode. *ACS Sustainable Chemistry & Engineering* **2022,** *10* (23), 7586-7594.
21. Lin, C.; Dong, C.; Kim, S.; Lu, Y.; Wang, Y.; Yu, Z.; Gu, Y.; Gu, Z.; Lee, D. K.; Zhang, K., Photo-Electrochemical Glycerol Conversion over a Mie Scattering Effect Enhanced Porous BiVO4 Photoanode. *Advanced Materials* **2023,** *35* (15), 2209955.
22. Pan, Y.; Zhang, H.; Zhang, B.; Gong, F.; Feng, J.; Huang, H.; Vanka, S.; Fan, R.; Cao, Q.; Shen, M., Renewable formate from sunlight, biomass and carbon dioxide in a photoelectrochemical cell. *Nature Communications* **2023,** *14* (1), 1013.
23. Carrai, I.; Mazzaro, R.; Bassan, E.; Morselli, G.; Piccioni, A.; Grandi, S.; Caramori, S.; Ceroni, P.; Pasquini, L., Photoelectrochemical valorization of biomass derivatives with hematite photoanodes modified by co-catalysts. *Solar RRL* **2023**.
24. Woldu, A. R.; Huang, Z.; Zhao, P.; Hu, L.; Astruc, D., Electrochemical CO2 reduction (CO2RR) to multi-carbon products over copper-based catalysts. *Coordination Chemistry Reviews* **2022,** *454*, 214340.
25. Zhang, W.; Jin, Z.; Chen, Z., Rational-Designed Principles for Electrochemical and Photoelectrochemical Upgrading of CO2 to Value-Added Chemicals. *Advanced Science* **2022,** *9* (9), 2105204.
26. Dubouis, N.; Grimaud, A., The hydrogen evolution reaction: from material to interfacial descriptors. *Chemical Science* **2019,** *10* (40), 9165-9181.
27. Marcandalli, G.; Boterman, K.; Koper, M. T. M., Understanding hydrogen evolution reaction in bicarbonate buffer. *Journal of Catalysis* **2022,** *405*, 346-354.
28. Tavella, F.; Giusi, D.; Ampelli, C., Nitrogen reduction reaction to ammonia at ambient conditions: A short review analysis of the critical factors limiting electrocatalytic performance. *Current Opinion in Green and Sustainable Chemistry* **2022,** *35*, 100604.

29. Yang, C.; Zhu, Y.; Liu, J.; Qin, Y.; Wang, H.; Liu, H.; Chen, Y.; Zhang, Z.; Hu, W., Defect engineering for electrochemical nitrogen reduction reaction to ammonia. *Nano Energy* **2020,** *77*, 105126.
30. Yang, J.; Wang, D.; Han, H.; Li, C. A. N., Roles of cocatalysts in photocatalysis and photoelectrocatalysis. *Accounts of chemical research* **2013,** *46* (8), 1900-1909.
31. Ashik, U. P. M.; Viswan, A.; Kudo, S.; Hayashi, J.-i., Nanomaterials as catalysts. In *Applications of nanomaterials*, Elsevier: 2018; pp 45-82.
32. Wang, Y.; Zheng, X.; Wang, D., Design concept for electrocatalysts. *Nano Research* **2022**, 1-23.
33. Linnemann, J.; Kanokkanchana, K.; Tschulik, K., Design strategies for electrocatalysts from an electrochemist's perspective. *ACS Catalysis* **2021,** *11* (9), 5318-5346.
34. Usman, M. R., Hydrogen storage methods: Review and current status. *Renewable and Sustainable Energy Reviews* **2022,** *167*, 112743.
35. Tashie-Lewis, B. C.; Nnabuife, S. G., Hydrogen production, distribution, storage and power conversion in a hydrogen economy-a technology review. *Chemical Engineering Journal Advances* **2021,** *8*, 100172.
36. Oliveira, A. M.; Beswick, R. R.; Yan, Y., A green hydrogen economy for a renewable energy society. *Current Opinion in Chemical Engineering* **2021,** *33*, 100701.
37. Verhelst, S.; Wallner, T., Hydrogen-fueled internal combustion engines. *Progress in energy and combustion science* **2009,** *35* (6), 490-527.
38. Sarmah, M. K.; Singh, T. P.; Kalita, P.; Dewan, A., Sustainable hydrogen generation and storage–a review. *RSC advances* **2023,** *13* (36), 25253-25275.
39. *Global Hydrogen Review 2023*; International Energy Agency: IEA: 2023.
40. Incer-Valverde, J.; Korayem, A.; Tsatsaronis, G.; Morosuk, T., "Colors" of hydrogen: Definitions and carbon intensity. *Energy Conversion and Management* **2023,** *291*, 117294.
41. Millet, P., Fundamentals of water electrolysis. *Hydrogen Production: Electrolysis* **2015**, 33-62.
42. Zhang, L.; Zhao, H.; Wilkinson, D. P.; Sun, X.; Zhang, J., *Electrochemical water electrolysis: fundamentals and technologies*. CRC Press: 2020.
43. Chi, J.; Yu, H., Water electrolysis based on renewable energy for hydrogen production. *Chinese Journal of Catalysis* **2018,** *39* (3), 390-394.
44. Li, X.; Hao, X.; Abudula, A.; Guan, G., Nanostructured catalysts for electrochemical water splitting: current state and prospects. *Journal of Materials Chemistry A* **2016,** *4* (31), 11973-12000.
45. Eftekhari, A., Electrocatalysts for hydrogen evolution reaction. *International Journal of Hydrogen Energy* **2017,** *42* (16), 11053-11077.

46. Mohammed-Ibrahim, J.; Sun, X., Recent progress on earth abundant electrocatalysts for hydrogen evolution reaction (HER) in alkaline medium to achieve efficient water splitting–A review. *Journal of Energy Chemistry* **2019,** *34*, 111-160.
47. Shah, A. H.; Wan, C.; Huang, Y.; Duan, X., Toward Molecular Level Understandings of Hydrogen Evolution Reaction on Platinum Surface. *The Journal of Physical Chemistry C* **2023,** *127* (27), 12841-12848.
48. Zhong, G.; Cheng, T.; Shah, A. H.; Wan, C.; Huang, Z.; Wang, S.; Leng, T.; Huang, Y.; Goddard Iii, W. A.; Duan, X., Determining the hydronium pK α at platinum surfaces and the effect on pH-dependent hydrogen evolution reaction kinetics. *Proceedings of the National Academy of Sciences* **2022,** *119* (39), e2208187119.
49. Wu, H.; Feng, C.; Zhang, L.; Zhang, J.; Wilkinson, D. P., Non-noble metal electrocatalysts for the hydrogen evolution reaction in water electrolysis. *Electrochemical Energy Reviews* **2021,** *4* (3), 473-507.
50. Wu, T.; Sun, M.-Z.; Huang, B.-L., Non-noble metal-based bifunctional electrocatalysts for hydrogen production. *Rare Metals* **2022,** *41* (7), 2169-2183.
51. Kuznetsov, D. A.; Chen, Z.; Kumar, P. V.; Tsoukalou, A.; Kierzkowska, A.; Abdala, P. M.; Safonova, O. V.; Fedorov, A.; Müller, C. R., Single site cobalt substitution in 2D molybdenum carbide (MXene) enhances catalytic activity in the hydrogen evolution reaction. *Journal of the American Chemical Society* **2019,** *141* (44), 17809-17816.
52. Vesborg, P. C. K.; Seger, B.; Chorkendorff, I. B., Recent development in hydrogen evolution reaction catalysts and their practical implementation. *The journal of physical chemistry letters* **2015,** *6* (6), 951-957.
53. Nadar, A.; Banerjee, A. M.; Pai, M. R.; Antony, R. P.; Patra, A. K.; Sastry, P. U.; Donthula, H.; Tewari, R.; Tripathi, A. K., Effect of Mo content on hydrogen evolution reaction activity of Mo2C/C electrocatalysts. *International Journal of Hydrogen Energy* **2020,** *45* (23), 12691-12701.
54. Piontek, S.; Andronescu, C.; Zaichenko, A.; Konkena, B.; Junge Puring, K.; Marler, B.; Antoni, H.; Sinev, I.; Muhler, M.; Mollenhauer, D., Influence of the Fe: Ni Ratio and Reaction Temperature on the Efficiency of (Fe x Ni1–x) 9S8 Electrocatalysts Applied in the Hydrogen Evolution Reaction. *ACS Catalysis* **2018,** *8* (2), 987-996.
55. Wei, Y.; He, W.; Sun, P.; Yin, J.; Deng, X.; Xu, X., Synthesis of hollow Cu/Cu2O/Cu2S nanotubes for enhanced electrocatalytic hydrogen evolution. *Applied Surface Science* **2019,** *476*, 966-971.
56. Shen, Y.; Zhou, Y.; Wang, D.; Wu, X.; Li, J.; Xi, J., Nickel–copper alloy encapsulated in graphitic carbon shells as electrocatalysts for hydrogen evolution reaction. *Advanced Energy Materials* **2018,** *8* (2), 1701759.

57. Popczun, E. J.; McKone, J. R.; Read, C. G.; Biacchi, A. J.; Wiltrout, A. M.; Lewis, N. S.; Schaak, R. E., Nanostructured nickel phosphide as an electrocatalyst for the hydrogen evolution reaction. *Journal of the American Chemical Society* **2013,** *135* (25), 9267-9270.
58. Anantharaj, S.; Kundu, S.; Noda, S., Progress in nickel chalcogenide electrocatalyzed hydrogen evolution reaction. *Journal of Materials Chemistry A* **2020,** *8* (8), 4174-4192.
59. Walter, M. G.; Warren, E. L.; McKone, J. R.; Boettcher, S. W.; Mi, Q.; Santori, E. A.; Lewis, N. S., Solar water splitting cells. *Chemical reviews* **2010,** *110* (11), 6446-6473.
60. Bhat, K. S.; Nagaraja, H. S., Hydrogen evolution reaction at extreme pH conditions of copper sulfide micro-hexagons. *Journal of Science: Advanced Materials and Devices* **2020,** *5* (3), 361-367.
61. Bhat, K. S.; Nagaraja, H. S., Performance evaluation of molybdenum dichalcogenide (MoX2; X= S, Se, Te) nanostructures for hydrogen evolution reaction. *International Journal of Hydrogen Energy* **2019,** *44* (33), 17878-17886.
62. Salehizadeh, H.; Yan, N.; Farnood, R., Recent advances in microbial CO2 fixation and conversion to value-added products. *Chemical engineering journal* **2020,** *390*, 124584.
63. Liu, Z.; Wang, K.; Chen, Y.; Tan, T.; Nielsen, J., Third-generation biorefineries as the means to produce fuels and chemicals from CO2. *Nature catalysis* **2020,** *3* (3), 274-288.
64. Pradhan, S.; Roy, S.; Sahoo, B.; Chatterjee, I., Utilization of CO2 feedstock for organic synthesis by visible-light photoredox catalysis. *Chemistry–A European Journal* **2021,** *27* (7), 2254-2269.
65. Hori, Y.; Murata, A.; Takahashi, R.; Suzuki, S., Electroreduction of carbon monoxide to methane and ethylene at a copper electrode in aqueous solutions at ambient temperature and pressure. *Journal of the American Chemical Society* **1987,** *109* (16), 5022-5023.
66. Huang, J.; Mensi, M.; Oveisi, E.; Mantella, V.; Buonsanti, R., Structural sensitivities in bimetallic catalysts for electrochemical CO2 reduction revealed by Ag–Cu nanodimers. *Journal of the American Chemical Society* **2019,** *141* (6), 2490-2499.
67. Zang, D.; Gao, X. J.; Li, L.; Wei, Y.; Wang, H., Confined interface engineering of self-supported Cu@ N-doped graphene for electrocatalytic CO2 reduction with enhanced selectivity towards ethanol. *Nano Research* **2022,** *15* (10), 8872-8879.
68. Dutta, A.; Rahaman, M.; Hecker, B.; Drnec, J.; Kiran, K.; Montiel, I. Z.; Weber, D. J.; Zanetti, A.; López, A. C.; Martens, I., CO2 electrolysis–Complementary operando XRD, XAS and Raman spectroscopy study on the stability of CuxO foam catalysts. *Journal of catalysis* **2020,** *389*, 592-603.

69. Wen, C. F.; Zhou, M.; Liu, P. F.; Liu, Y.; Wu, X.; Mao, F.; Dai, S.; Xu, B.; Wang, X. L.; Jiang, Z., Highly Ethylene-Selective Electrocatalytic CO2 Reduction Enabled by Isolated Cu− S Motifs in Metal–Organic Framework Based Precatalysts. *Angewandte Chemie International Edition* **2022,** *61* (2), e202111700.
70. He, W.; Liberman, I.; Rozenberg, I.; Ifraemov, R.; Hod, I., Electrochemically driven cation exchange enables the rational design of active CO2 reduction electrocatalysts. *Angewandte Chemie* **2020,** *132* (21), 8339-8346.
71. Chen, Y.; Chen, K.; Fu, J.; Yamaguchi, A.; Li, H.; Pan, H.; Hu, J.; Miyauchi, M.; Liu, M., Recent advances in the utilization of copper sulfide compounds for electrochemical CO2 reduction. *Nano Materials Science* **2020,** *2* (3), 235-247.
72. De Gregorio, G. L.; Burdyny, T.; Loiudice, A.; Iyengar, P.; Smith, W. A.; Buonsanti, R., Facet-dependent selectivity of Cu catalysts in electrochemical CO2 reduction at commercially viable current densities. *ACS catalysis* **2020,** *10* (9), 4854-4862.
73. Rossi, K.; Buonsanti, R., Shaping copper nanocatalysts to steer selectivity in the electrochemical CO2 reduction reaction. *Accounts of Chemical Research* **2022,** *55* (5), 629-637.
74. Grosse, P.; Yoon, A.; Rettenmaier, C.; Chee, S. W.; Cuenya, B. R., Growth dynamics and processes governing the stability of electrodeposited size-controlled cubic Cu catalysts. *The Journal of Physical Chemistry C* **2020,** *124* (49), 26908-26915.
75. Kim, C.; Cho, K. M.; Park, K.; Kim, J. Y.; Yun, G. T.; Toma, F. M.; Gereige, I.; Jung, H. T., Cu/Cu2O interconnected porous aerogel catalyst for highly productive electrosynthesis of ethanol from CO2. *Advanced Functional Materials* **2021,** *31* (32), 2102142.
76. Li, H.; Liu, T.; Wei, P.; Lin, L.; Gao, D.; Wang, G.; Bao, X., High-rate CO2 electroreduction to C2+ products over a copper-copper iodide catalyst. *Angewandte Chemie* **2021,** *133* (26), 14450-14454.
77. Tomboc, G. M.; Choi, S.; Kwon, T.; Hwang, Y. J.; Lee, K., Potential link between Cu surface and selective CO2 electroreduction: perspective on future electrocatalyst designs. *Advanced Materials* **2020,** *32* (17), 1908398.
78. Rajeshwar, K.; Singh, P.; DuBow, J., Energy conversion in photoelectrochemical systems—a review. *Electrochimica Acta* **1978,** *23* (11), 1117-1144.
79. Fujishima, A.; Honda, K., Electrochemical photolysis of water at a semiconductor electrode. *nature* **1972,** *238* (5358), 37-38.
80. Karaca, A. E.; Dincer, I., Development of a new photoelectrochemical system for clean hydrogen production and a comparative environmental impact assessment with other production methods. *Chemosphere* **2023,** *337*, 139367.

81. Amano, F., Photoelectrochemical Oxygen Evolution. *Solar-to-Chemical Conversion: Photocatalytic and Photoelectrochemcial Processes* **2021**, 163-187.
82. Mesa Zamora, C.; Francas Forcada, L.; Yang, K. R.; Garrido-Barros, P.; Pastor Hernandez, E.; Ma, Y.; Kafizas, A.; Rosser, T. E.; Mayer, M. T.; Reisner, E., Multihole water oxidation catalysis on hematite photoanodes revealed by operando spectroelectrochemistry and DFT.
83. Cha, H. G.; Choi, K.-S., Combined biomass valorization and hydrogen production in a photoelectrochemical cell. *Nature chemistry* **2015,** *7* (4), 328-333.
84. Karjule, N.; Phatake, R. S.; Barzilai, S.; Mondal, B.; Azoulay, A.; Shames, A. I.; Volokh, M.; Albero, J.; García, H.; Shalom, M., Photoelectrochemical alcohols oxidation over polymeric carbon nitride photoanodes with simultaneous H 2 production. *Journal of Materials Chemistry A* **2022,** *10* (31), 16585-16594.
85. Lhermitte, C. R.; Plainpan, N.; Canjura, P.; Boudoire, F.; Sivula, K., Direct photoelectrochemical oxidation of hydroxymethylfurfural on tungsten trioxide photoanodes. *Rsc Advances* **2021,** *11* (1), 198-202.
86. Antón-García, D.; Edwardes Moore, E.; Bajada, M. A.; Eisenschmidt, A.; Oliveira, A. R.; Pereira, I. A. C.; Warnan, J.; Reisner, E., Photoelectrochemical hybrid cell for unbiased CO2 reduction coupled to alcohol oxidation. *Nature Synthesis* **2022,** *1* (1), 77-86.
87. Ashcroft, N. W.; Mermin, N. D., Solid state. *Physics (New York: Holt, Rinehart and Winston) Appendix C* **1976**.
88. Balkan, N.; Erol, A.; Balkan, N.; Erol, A., Intrinsic and Extrinsic Semiconductors. *Semiconductors for Optoelectronics: Basics and Applications* **2021**, 37-78.
89. Kittel, C., *Introduction to solid state physics*. John Wiley & sons, inc: 2005.
90. Peter, L. M., Semiconductor electrochemistry. *Photoelectrochemical Solar Fuel Production: From Basic Principles to Advanced Devices* **2016**, 3-40.
91. Bisquert, J.; Cendula, P.; Bertoluzzi, L.; Gimenez, S., Energy diagram of semiconductor/electrolyte junctions. ACS Publications: 2014; Vol. 5, pp 205-207.
92. Einax, M. In *Thermodynamic interpretation of the open-circuit voltage in sustainable energy conversion processes*, 2023; AIP Publishing.
93. Gärtner, W. W., Depletion-layer photoeffects in semiconductors. *Physical Review* **1959,** *116* (1), 84.
94. Nabgan, W.; Nabgan, B.; Jalil, A. A.; Ikram, M.; Hussain, I.; Bahari, M. B.; Tran, T. V.; Alhassan, M.; Owgi, A. H. K.; Parashuram, L., A bibliometric examination and state-of-the-art overview of hydrogen generation from

photoelectrochemical water splitting. *International Journal of Hydrogen Energy* **2023**.
95. Xu, K.; Zhang, Q.; Zhou, X.; Zhu, M.; Chen, H., Recent Progress and Perspectives on Photocathode Materials for CO2 Catalytic Reduction. *Nanomaterials* **2023,** *13* (10), 1683.
96. Brillas, E.; Garcia-Segura, S., Recent progress of applied TiO2 photoelectrocatalysis for the degradation of organic pollutants in wastewaters. *Journal of Environmental Chemical Engineering* **2023**, 109635.
97. Khan, A.; Shkir, M.; Ibrahim, E. H.; Kilany, M.; AlFaify, S.; Sayed, M. A.; El-Toni, A. M.; Aldalbahi, A.; Rahaman, H.; Siddiquei, M. M., Effect of Bi contents on key physical properties of NiO NPs synthesized by flash combustion process and their cytotoxicity studies for biomedical applications. *Ceramics International* **2020,** *46* (12), 19691-19700.
98. Correa-Baena, J.-P.; Saliba, M.; Buonassisi, T.; Grätzel, M.; Abate, A.; Tress, W.; Hagfeldt, A., Promises and challenges of perovskite solar cells. *Science* **2017,** *358* (6364), 739-744.
99. Qin, C.; Sandanayaka, A. S. D.; Zhao, C.; Matsushima, T.; Zhang, D.; Fujihara, T.; Adachi, C., Stable room-temperature continuous-wave lasing in quasi-2D perovskite films. *Nature* **2020,** *585* (7823), 53-57.
100. Fakharuddin, A.; Gangishetty, M. K.; Abdi-Jalebi, M.; Chin, S.-H.; bin Mohd Yusoff, A. R.; Congreve, D. N.; Tress, W.; Deschler, F.; Vasilopoulou, M.; Bolink, H. J., Perovskite light-emitting diodes. *Nature Electronics* **2022,** *5* (4), 203-216.
101. Kim, J. S.; Heo, J.-M.; Park, G.-S.; Woo, S.-J.; Cho, C.; Yun, H. J.; Kim, D.-H.; Park, J.; Lee, S.-C.; Park, S.-H., Ultra-bright, efficient and stable perovskite light-emitting diodes. *Nature* **2022,** *611* (7937), 688-694.
102. Chouhan, L.; Ghimire, S.; Subrahmanyam, C.; Miyasaka, T.; Biju, V., Synthesis, optoelectronic properties and applications of halide perovskites. *Chemical Society Reviews* **2020,** *49* (10), 2869-2885.
103. Pitaro, M.; Tekelenburg, E. K.; Shao, S.; Loi, M. A., Tin halide perovskites: from fundamental properties to solar cells. *Advanced Materials* **2022,** *34* (1), 2105844.
104. Straus, D. B.; Guo, S.; Abeykoon, A. M. M.; Cava, R. J., Understanding the Instability of the Halide Perovskite CsPbI3 through Temperature-Dependent Structural Analysis. *Advanced Materials* **2020,** *32* (32), 2001069.
105. Schileo, G.; Grancini, G., Halide perovskites: current issues and new strategies to push material and device stability. *Journal of Physics: Energy* **2020,** *2* (2), 021005.
106. Dey, A.; Ye, J.; De, A.; Debroye, E.; Ha, S. K.; Bladt, E.; Kshirsagar, A. S.; Wang, Z.; Yin, J.; Wang, Y., State of the art and prospects for halide perovskite nanocrystals. *ACS nano* **2021,** *15* (7), 10775-10981.

107. Protesescu, L.; Yakunin, S.; Bodnarchuk, M. I.; Krieg, F.; Caputo, R.; Hendon, C. H.; Yang, R. X.; Walsh, A.; Kovalenko, M. V., Nanocrystals of cesium lead halide perovskites (CsPbX3, X= Cl, Br, and I): novel optoelectronic materials showing bright emission with wide color gamut. *Nano letters* **2015,** *15* (6), 3692-3696.
108. Cardenas-Morcoso, D.; Gualdrón-Reyes, A. s. F.; Ferreira Vitoreti, A. B.; García-Tecedor, M.; Yoon, S. J.; Solis de la Fuente, M.; Mora-Seró, I. n.; Gimenez, S., Photocatalytic and photoelectrochemical degradation of organic compounds with all-inorganic metal halide perovskite quantum dots. *The Journal of Physical Chemistry Letters* **2019,** *10* (3), 630-636.
109. Yang, W.; Prabhakar, R. R.; Tan, J.; Tilley, S. D.; Moon, J., Strategies for enhancing the photocurrent, photovoltage, and stability of photoelectrodes for photoelectrochemical water splitting. *Chemical Society Reviews* **2019,** *48* (19), 4979-5015.
110. Tan, R.; Sivanantham, A.; Rani, B. J.; Jeong, Y. J.; Cho, I. S., Recent advances in surface regulation and engineering strategies of photoelectrodes toward enhanced photoelectrochemical water splitting. *Coordination Chemistry Reviews* **2023,** *494*, 215362.
111. Ding, P.; Jiang, T.; Han, N.; Li, Y., Photocathode engineering for efficient photoelectrochemical CO2 reduction. *Materials Today Nano* **2020,** *10*, 100077.
112. García-Tecedor, M.; Cardenas-Morcoso, D.; Fernández-Climent, R.; Giménez, S., The role of underlayers and overlayers in thin film BiVO4 photoanodes for solar water splitting. *Advanced Materials Interfaces* **2019,** *6* (15), 1900299.
113. Fareza, A. R.; Nugroho, F. A. A.; Abdi, F. F.; Fauzia, V., Nanoscale metal oxides–2D materials heterostructures for photoelectrochemical water splitting—a review. *Journal of Materials Chemistry A* **2022,** *10* (16), 8656-8686.
114. Yang, J. W.; Ahn, S. H.; Jang, H. W., Crucial role of heterostructures in highly advanced water splitting photoelectrodes. *Current Opinion in Green and Sustainable Chemistry* **2021,** *29*, 100454.
115. Wang, B.; Cao, J.-T.; Liu, Y.-M., Recent progress of heterostructure-based photoelectrodes in photoelectrochemical biosensing: a mini review. *Analyst* **2020,** *145* (4), 1121-1128.
116. Zoli, M.; Guzmán, H.; Sacco, A.; Russo, N.; Hernández, S., Cu2O/SnO2 Heterostructures: Role of the Synthesis Procedure on PEC CO2 Conversion. *Materials* **2023,** *16* (13), 4497.
117. Castellanos-Gomez, A.; Duan, X.; Fei, Z.; Gutierrez, H. R.; Huang, Y.; Huang, X.; Quereda, J.; Qian, Q.; Sutter, E.; Sutter, P., Van der Waals heterostructures. *Nature Reviews Methods Primers* **2022,** *2* (1), 58.

118. Resasco, J.; Zhang, H.; Kornienko, N.; Becknell, N.; Lee, H.; Guo, J.; Briseno, A. L.; Yang, P., TiO2/BiVO4 nanowire heterostructure photoanodes based on type II band alignment. *ACS central science* **2016,** *2* (2), 80-88.

Chapter 2

Experimental methods

This chapter describes the fundamentals of the experimental methods involved in all the studies carried out during this thesis including the synthesis of the materials, their morphological and compositional characterization, the performance and study of the electrochemical reactions and the subsequent product analysis. The specific experimental details such as reagents information or particular experimental conditions, are detailed in the corresponding chapter.

2.1 Samples preparation: synthesis and deposition methods

In this thesis, five different materials were prepared to be studied for different reactions. *Chapter 3* and *Chapter 6* detail each one of the synthetic routes of the materials and the electrodes. In this section, the fundamentals of the synthesis and deposition techniques that were employed are described.

2.1.1 Hydrothermal method

Hydrothermal is one of the most common methods to prepare precursors and nanomaterials directly from an aqueous solution at elevated temperature and pressure conditions.[1] Hydrothermal processes involve the utilization of reactants such as solids, sols, gels, or suspensions. The preparation process can takes place in a wide temperature and pressure ranges, depending on the specification of the

synthesis. Interesting material properties such as particle size or crystallinity can be modified by adjusting experimental parameters such as the temperature.[2]

In this thesis, hydrothermal method was used to prepare sodium polysulfide solution for the synthesis of $Cu_{2-x}S$ electrocatalyst in *Chapter 3*. **Figure 2.1** shows a schematic representation of the experimental process.

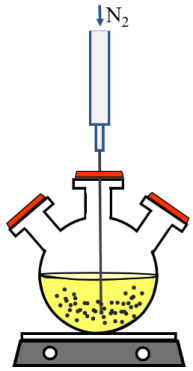

Figure 2.1. Representation of the hydrothermal synthesis for $Cu_{2-x}S$ nanoparticles.

2.1.2 Drop-casting method

Drop-casting or drop-coating method is a facile and rapid technique to deposit a thin film, by impinging droplets on the substrate employed for many applications.[3-8] A solution containing the material of interest is poured drop by drop onto the substrate surface, properly pre-treated, and then dried. The drop first spreads on the surface, due to the interfacial forces that are inclined to drive the droplet outward. When multiple droplets are casted onto the substrate surface, the edges of each droplet come in contact with another droplet, they mix together, forming a noncircular drop with a concave contact line.[9]

This versatile technique allows to adjust the deposition procedure as required by the sample. Thus, depending on the deposited area, the method consists of spreading a single drop or multiple drops of different volumes. To dry the

solution and evaporate the solvent, different temperatures need to be applied depending on the evaporation point of the solvent.

In this thesis, the drop-casting method was used to prepare $Cu_{2-x}S$ films on Cu foil in *Chapter 3*. The dropped sodium polysulfide solution was the sulfur precursor and the metallic substrate was the copper precursor. Upon contact at high temperature, a thin layer of $Cu_{2-x}S$ forms on the surface of the Cu substrate. In this case, the deposition of multiple drops is required to cover the entire area and guarantee the complete reaction of the precursors (see **Figure 2.2**). The whole complete synthetic route is detailed in *Chapter 3*.

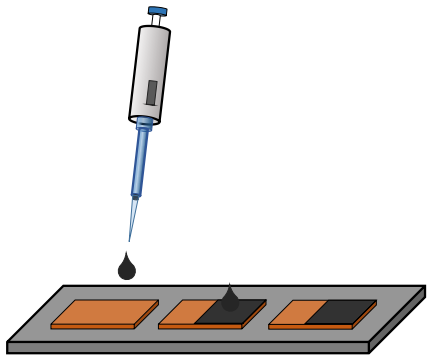

Figure 2.2. Scheme of the drop-casting method used in this thesis to synthesize $Cu_{2-x}S$ electrodes in *Chapter 3.*

2.1.3 Hot-injection method

Hot-injection method is a synthetic route, to produce colloidal nanocrystals, consisting of quickly injecting a cold stock solution containing the precursors into a hot solution containing surfactants and high-boiling point solvents. This method has become very popular for synthetizing colloidal quantum dots due to its good monodispersion, tuneable composition, size, shape and optical, electrical and magnetic properties of the colloidal nanoparticles.[10-11]

In this thesis, the perovskite nanocrystals (NCs) investigated in *Chapter 6* were prepared by using the hot-injection method in collaboration with the Group of Advances Semiconductors (GAS) at INAM. This method was first employed on $CsPbBr_3$ perovskites by Protesescu et al.[12] This synthetic route only takes a few seconds due to the fast nucleation and growth kinetics. The reaction is subsequently quenched to stop the growth of the nanocrystals and then a two-step purification of NCs was completed for isolating the NCs. **Figure 2.3** represents the experimental procedure of hot-injection.

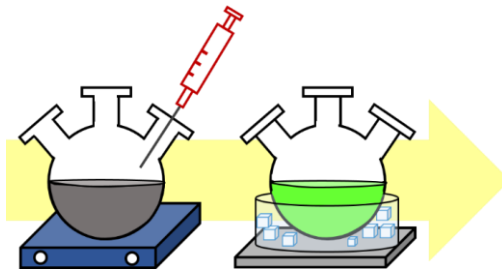

Figure 2.3. Scheme of the hot-injection method.

2.1.4 Spin-coating

Spin-coating is a depositing method to prepare thin films onto a flat functional substrate. Typically, a small amount of the coating solution is deposited on the centre of the substrate with a micropipette. Then, the substrate is rotated at high speeds (usually thousands of revolutions per minute-rpm) to spread the coating material by centrifugal force forming a uniformly thin layer. Thin films ranging from just a few micrometers (μm) in thickness down to a single nanometre (nm) can be obtained with no chemical constraints. The equipment used for spin-coating is called a spin-coater, and it is possible to control parameters such as the centrifugation time, the speed and the acceleration of rotation.[13-14] It is important

to, prior to the deposition, carefully clean the substrates to ensure a homogeneous attachment.

In this thesis, spin-coating was used to prepare multilayered electrodes in *Chapter 6*. Two different metallic oxides were deposited on a FTO (Fluorine-doped tin oxide) glass for a certain time with specific rates and accelerations, and perovskite NCs described in the previous technique were deposited on the top of the oxide layer. The spin-coating process is depicted in **Figure 2.4**.

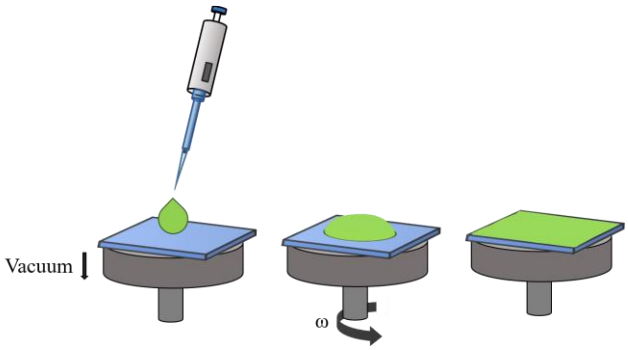

Figure 2.4. Schematic representation of the process of spin-coating of thin films indicating the vacuum to hold the sample and direction of rotation.

2.2 Compositional and morphological characterization

This section describes the different structural, morphological and compositional characterization techniques that have been used to study the materials that are part of this thesis.

2.2.1 Scanning electron microscopy

Fundamentals. Scanning electron microscopy (SEM) is a useful technique to investigate the microstructure morphology and elemental composition of the materials. This technique basically consists of the interaction of an electron beam with a solid sample. Electrons are emitted from a filament and collimated into a

beam in the electron source. Then, the beam is focused on the sample surface by a set of lenses in the electron column. As a result of the interaction between the accelerated electron beam inside the SEM and the sample, two types of electrons are generated: primary or backscattered electrons (high energy) and secondary electrons (low energy, below 50 eV). From the relaxation of the excited atom after interacting with the electron beam, three processes can take place: Auger electrons, X-rays and cathodoluminescence. SEM operates with secondary and/or backscattered electrons, whose signals are collected by different detectors conforming high-resolution topographic images. A fraction of the electrons coming from the beam are absorbed by the sample generating a current. **Figure 2.5** schematizes these scattering processes during a SEM measurement.[15-16]

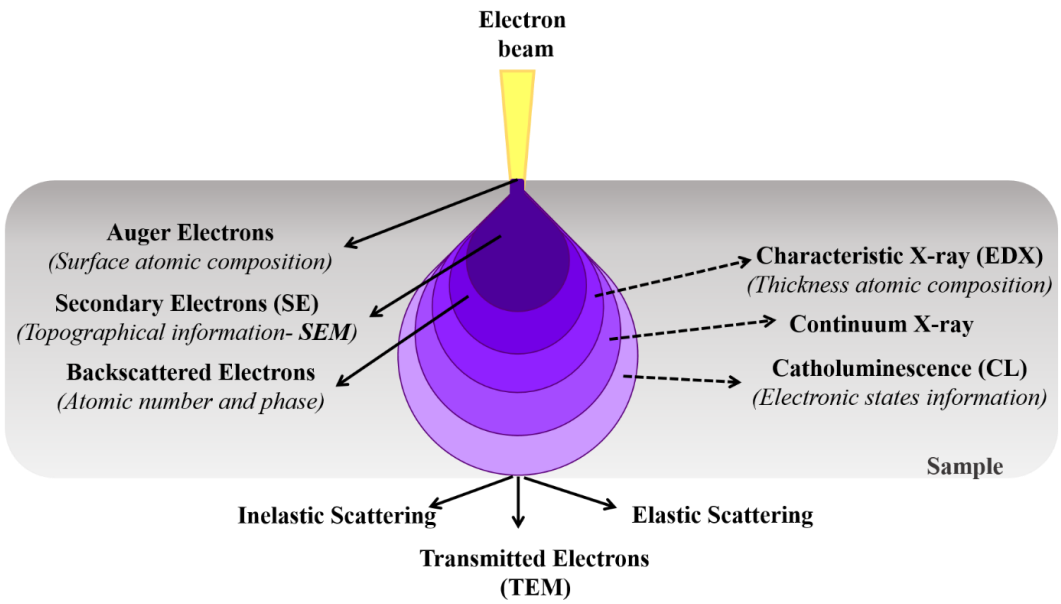

Figure 2.5. Scheme of the interaction of an electron beam with the sample during a SEM measurement.

Each of the materials used in this thesis were characterized by SEM. Not only top-view images but also cross-sectional images allowed us to study the

morphology, porosity and composition of the surface of the material, as well as their thickness.

Sample preparation. The sample is usually coated with a layer of carbon or a thin layer of a metal such as gold or platinum to give the sample conductive properties. Heterostrucured TiO_2 and NiO films (*Chapter 6*) were platinized for SEM characterization while $Cu_{2-x}S$ films did not need Pt coating due to the metallic nature of the substrate.

Equipment. SEM measurements were performed with a JSM-7000F JEOL FEG-SEM system (Tokyo, Japan) equipped with an INCA 400 Oxford EDS analyzer (Oxford, U.K.) operating at 15 kV at the Servei Central d'Instrumentació Científica (SCIC), Universitat Jaume I.

2.2.2 Energy dispersive X-ray spectroscopy

Fundamentals. Energy dispersive X-ray spectroscopy (also known as EDS, EDX, or EDXS) provides information on the elemental composition of the sample at concentration of least 0.1% in typical SEM instrument.[16] When the beam of electrons interacts with the nucleus of an atom of the sample, an electron from deep energetic bands excites and knock the electron out, leaving a hole. An electron from the outer shell replace the hole releasing the increased energy in the form of X-ray. Due to the principle that each element has its characteristic X-rays, the EDS detectors analyse the emitted X-ray signals and are able to differentiate elements.[17]

All the samples characterized by SEM in the following chapters were analysed by EDS. Combining both SEM images and EDS analysis provides a powerful tool to study a new material, extracting relevant information on its morphology

and elemental composition, while guiding for further characterizations such as TEM, XRD or XPS (detailed below).

Sample preparation and *Equipment* the same as for SEM.

2.2.3 High-resolution transmission electron microscopy

Fundamentals. High-resolution transmission electron microscopy (HRTEM) is a particularly suitable technique for structural and analytical nano-characterisation of materials, since it operates at high beam energy (much higher compared to SEM). A beam of electrons of hundreds of keV (typically 60-300 keV) passes through the sample providing high-resolution images with high spatial resolution (<1 Å).[18]

A conventional transmission electron microscopy (CTEM) could be additionally equipped with scanning coils, detectors and necessary circuitry, also allowing scanning transmission electron microscopy (STEM) measurements.[19] In STEM operating mode, the electron beam is focused to a fine spot (with the typical spot size 0.05 – 0.2 nm) suitable for analytical techniques such as high-angle annular dark-field (HAADF) or electron energy loss spectroscopy (EELS).[20]

High-angle annular dark-field imaging (HAADF) is a method of mapping samples in STEM by collecting scattered electrons with an annular dark-field detector formed by very high angle.[21] Electron Energy Loss Spectroscopy (EELS) coupled with HRTEM and STEM provides valuable elemental identification at the nanometer scale. When the sample is exposed to the beam of electrons with a known and narrow range of kinetic energies, inelastic scattering takes place in some electrons, which implies that they lose energy. Finally, these

energy losses are interpreted in an electron spectrometer. *Chapter 3* presents a complete HRTEM characterization of the $Cu_{2-x}S$ including both HRTEM and (HAADF) STEM images, STEM-EELS analysis and EELS composition maps which in addition to showing the composition also show how it is distributed.

Sample preparation. Since the electrons must pass through the sample, an electron transparent sample in powder form is needed (thickness below 30 nm). For this purpose, the electrodes were scraped to obtain powder particles, which were deposited on the TEM grid (more details in *Chapter 3*).

Equipment. These measurements were performed in collaboration with the Catalan Institute of Nanoscience and Nanotechnology (ICN2). High-resolution transmission electron microscopy (HRTEM) and scanning transmission electron microscopy (STEM) investigations were performed on a field emission gun FEI Tecnai F20 microscope. High-angle annular dark-field (HAADF) STEM was combined with electron energy loss spectroscopy (EELS) in a Tecnai microscope by using a GATAN QUANTUM energy filter to obtain compositional maps.

2.2.4 Atomic force microscopy

Fundamentals. Atomic force microscopy (AFM) is a morphological characterization technique able to image almost any type of surface and measure distances on the nanoscale. To obtain the topographic image of a sample by AFM, a cantilever with a sharp tip raster-scan over the area of interest. The transition between elevated and depressed topographic accidents on the sample surface influences the deflection of the cantilever being monitored. Thus, the AFM can generate an exact topographic map of surface characteristics.[22-23]

In this thesis, the characterization by AFM together with SEM and HRTEM complement the morphological study of the synthesized materials. **Figure 2.6** shows the image of an AFM with a schematic drawing of the internal elements.

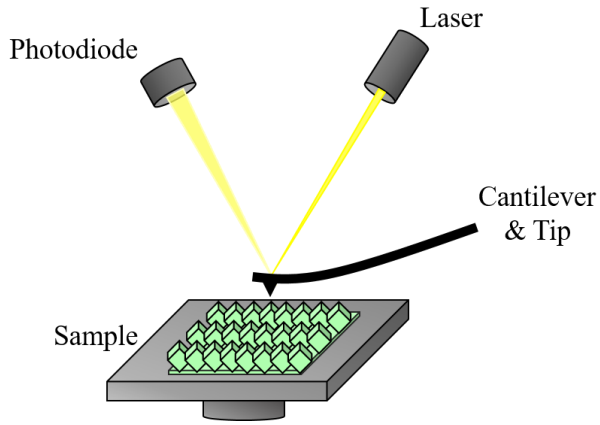

Figure 2.6. Schematic representation of the AFM internal set up.

Sample preparation. AFM is a non-destructive characterization technique and does not require any special preparation of the sample.

Equipment. Topographic images of the $Cu_{2-x}S$ samples in *Chapter 3* were measured by atomic force microscopy (AFM) using an Asylum Research Cypher ES (Oxford Instruments-Asylum Research, Santa Barbara, USA) in tapping mode under ambient conditions with a silicon cantilever AC160TSA-R3 (Olympus, Tokyo, Japan) with spring constant k = 25.4 N/m, resonant frequency f = 291 kHz, and a tip radius of 7 nm in collaboration with Universidad Central in Colombia. The topography of the heterostructured samples in *Chapter 4* was recorded using AFM atomic force microscope (Concept Scientific Instrument) on a relatively large area (10 x 10 μm^2) in Universitat Jaume I.

2.2.5 Profilometry

Fundamentals. Profilometry is a technique used to extract topographical data of a single point or even a full three-dimensional scan from a surface of a material. Two types of profilometers can be used: stylus or optical. Similar to AFM, stylus profilometer explore the surface by using a probe. The probe is physically moved along the study surface in order to acquire the surface height.[24] Optical profilometry uses light instead of a physical probe.[25]

In this thesis, profilometry was employed to determine the thickness of the thin layers in *Chapter 3*, as an alternative to cross section SEM used in *Chapter 6* for the same purpose. This is because the metal substrates synthetized in *Chapter 3* are not suitable for cross sectional SEM, due to its malleability that makes them difficult to break without edge effects, as well as, it is practically impossible to freeze metallic sample to break it due to its ductility.[26]

Sample preparation. No special sample preparation was required in our samples for this technique.

Equipment. Profilometer measurements in *Chapter 3* were performed on a mechanical profilometer Veeco model Dektak 6 provided by Servei Central d'Instrumentació Científica (SCIC) at Universitat Jaume I.

2.2.6 X-Ray diffraction

Fundamentals. X-Ray diffraction (XRD) is a powerful non-destructive technique for characterizing crystalline materials. It allows identifying the crystalline structures, phases, preferred crystal orientations and other structural parameters, such as crystallinity, strain, and crystal defects present in a powder or film. This technique is based on the interaction of a monochromatic beam of

X-rays with the material. As a consequence of the interaction, the beam of X-rays is scattered at specific angles from each set of lattice planes in the material and collected by a detector.[27-28] The geometrical interpretation of this interactions is described in **Figure 2.7** and follows Bragg's law (2.1):

$$n\lambda = 2d\ sin\theta \tag{2.1}$$

Where n is the order of diffraction, λ the wavelength of the incident beam, d the lattice spacing and θ the angle of the diffracted beam.

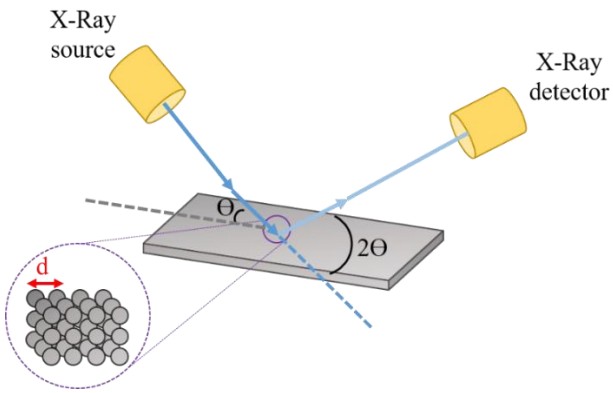

Figure 2.7. A representation of X-Ray Diffraction process.

The crystal structure consists of a set of planes, which are identified by Miller indices (h k l), and each one corresponds to a diffraction peak. Miller indices are often indicated at the top of each peak, as showed in *Chapter 6*. The generated diffraction pattern is the fingerprint of a periodic atomic arrangement in a given material.

Sample preparation. Since X-Ray Diffraction is non-destructive, no alteration or modification of the sample takes place either before or during the measurement. However, it is important to mention that when characterizing thin films, sometimes the depth of the X-ray penetration can be problematic if it is deeper than the thickness of the material. When this is the case, the resulting

diffractogram contains information from a mixture of different layers/materials, which add complexity to study the material. In order to overcome this problem, the films presented in this work were measured by applying the grazing angle configuration. This method is known as Grazing Beam X-Ray Diffraction (GIXRD).

Equipment. X-Ray Diffraction was measured using a Rigaku Miniflex 600 (Rigaku Corporation, Tokyo, Japan) with Cu Kα radiation (λ = 1.5418 Å) at the Servei Central d'Instrumentació Científica (SCIC), Universitat Jaume I.

2.2.7 X-Ray photoelectron spectroscopy

Fundamentals. X-Ray photoelectron spectroscopy (XPS) is a powerful technique widely used for surface characterization. Its bases reside in the photoelectric effect that take place after illuminating the sample with a monochromatic light. This technique allows to identify the elemental composition of the surface of a material, as well as its chemical state, the overall electronic structure and density of the electronic states and also the chemical environment.[29-30] When irradiating the material with soft X-ray photons (200-2000 eV) sufficiently energetic to promote a core level electron to leave the sample, the ejected electron leaves as a photoelectron. Because the energy of an X-ray photon is known, E_v, given that the kinetic energies of the emitted electrons are measured, E_k, and considering the work function of the analyser, ϕ, the electron binding energy of each of the emitted electrons, E_B, can be determined by using the photoelectric effect equation:

$$E_B = E_v - (E_k + \Phi) \quad (2.2)$$

The binding energy of each of the emitted electrons $E_{B,}$ is characteristic for each electronic level for a particular element. The chemical shift is the difference between E_B and the elemental state, and allows identifying both the chemical element and its oxidation state. **Figure 2.8** shows a representation of a XPS measurement.

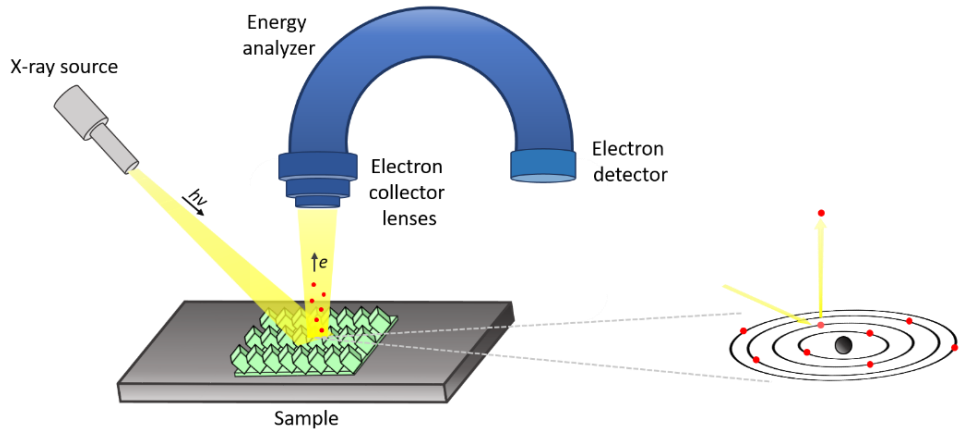

Figure 2.8. A scheme of an experimental XPS setup.

Sample preparation. Some considerations can contribute to better measurements and results, such as washing carefully the sample for post-mortem measurements to eliminate traces of the electrolyte and removing surface contamination on the sample by Ar^+ sputtering procedure.

Equipment. XPS has been carried out holding the sample at room temperature and illuminating it with monochromatized Al Kα light (hν = 1486.6 eV) from a microfocus setup (SPECS Focus 600). The excited photelectrons were collected by a SPECS 150 hemispherical analyzer at emission and incidence angles of 40 and 60°, respectively. The overall experimental resolution was extracted from Fermi edge analysis of a reference gold sample and resulted in 0.4 eV. The measurements included in this thesis were carried out in collaboration with Centro de Física de Materiales, University of the Basque Country UPV/EHU.

2.2.8 X-ray absorption near edge structure

Fundamentals. X-ray absorption near edge structure (XANES) is a valuable spectroscopic technique that provides detailed information about the electronic structure of specific elements in a material. When irradiating a sample with X-rays of equal energy to that required for core-level electron excitation, a sharp increase in absorption takes place i.e. absorption edge. The region immediately following this edge in the X-ray absorption spectrum is known as the near edge structure. It provides detailed information about the oxidation state, coordination environment, and bonding of the absorbing atom

Chapter 5 of this thesis includes XANES characterization for the investigation of the oxidation state of Cu species of $Cu_{2-x}S$ electrocatalysts driving the CO_2ER.

Sample preparation. For the specific investigation of the material presented in this thesis, the catalyst was scratched from the Cu substrate and encapsulated in Kapton under nitrogen atmosphere. Further details are described in *Chapter 5.*

Equipment. The XANES measurements were carried out in B18 general purpose XAS beamline on Diamond Light Source in an energy range of 2.05-35 keV in transmission mode.

2.2.9 Raman spectroscopy

Fundamentals. Raman spectroscopy is a useful characterization technique based on the study of the inelastic scattering of photons in a material, also known as Raman scattering. When a monochromatic light (a laser beam) impinges on a material, elastic and inelastic light scattering occurs.[31-32] The elastic scatterings or Rayleigh takes place when the energy of the scattered light is the same of the energy of the incident laser while, the inelastic scatterings processes, also known

as Raman scattering, have different energy compared to the laser. These latter processes are involved in Raman spectroscopy, and can be produced as *Stokes* shift when the energy of the incident photon is higher than the scattered photon or *Anti-Stokes* shift if the energy of the scattered photon is higher than the incident one. These inelastic scattering processes are related to vibrational, rotational and other low-frequency Raman-active modes. These events are characteristic of chemical bonds and symmetry of a molecule providing a fingerprint for molecular identification.

In this thesis, Raman spectroscopy technique was performed under *operando* conditions (deeper detailed in *section 2.4*) to measure $Cu_{2-x}S$ catalyst for CO_2RR in *Chapter 4.*

Figure 2.9 schematizes the different scattering processes on a molecule when irradiated with a laser and illustrate the energy transitions of each particular process on a diagram of states and energy.

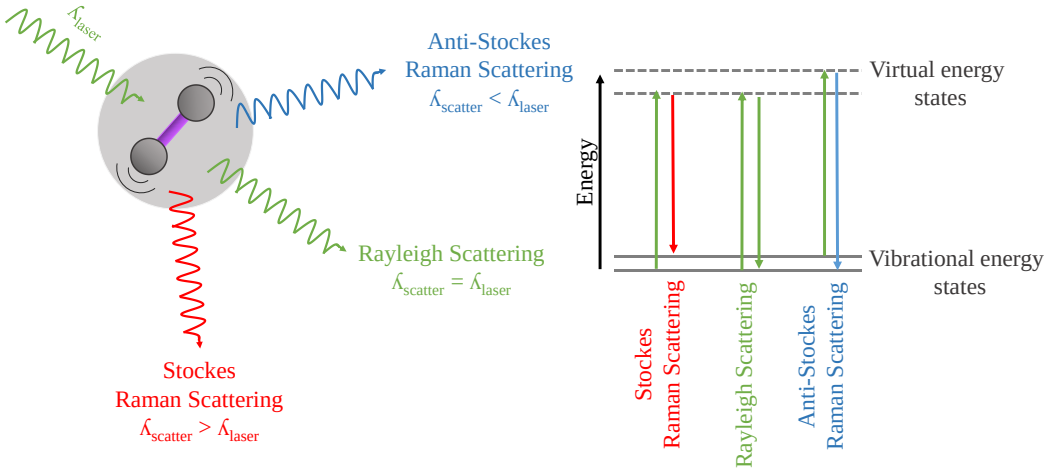

Figure 2.9. From left to right, diagram of the two types of interaction, elastic and inelastic, and diagram of states and energy levels involved in the Raman Effect.

Sample preparation. Raman Spectroscopy do not require specific sample preparation.

2.2.10 UV-Vis spectroscopy

Fundamentals. Ultraviolet-visible (UV-Vis) spectroscopy is an analytical technique for the quantitative determination of diverse samples widely used for materials characterization due to its versatility and moderate cost compared to other spectroscopical techniques. UV-Vis spectroscopy basis relies on the measurement of the amount of discrete wavelengths of UV or visible light that are absorbed by or transmitted through a sample in comparison to a reference or blank sample.[33-34]

The absorbed, transmitted or reflected light is measured as a function of the photon energy. Its theoretical bases are founded on the Beer-Lambert law depicted in equation (2.3), where the absorbance, A, is determined by the logarithmic relation of the measured intensity after the interaction of light with the sample (I) versus the incident light (I_0).

$$A = log \frac{Io}{I} \tag{2.3}$$

Sample preparation. Two different solid and liquid samples were characterized by UV-Vis spectroscopy in *Chapter 4* and *Chapter* 6. Whilst no special sample pretreatment is required, if the sample is liquid, it must be compatible with the cuvette and, if it is solid, with the corresponding support.

Equipment. A UV-Vis spectrophotometer integrated by a light source, wavelength selection (an arrangement of monochromator, absorption filters, interference filters, cutoff filters and bandpass filters), a sample holder and a detector was used for the spectroscopic measurements carried out in this thesis.

All the components are schematized in **Figure 2.10** UV-Vis measurements in *Chapter 4* and *Chapter* 6 were performed on an UV−vis−NIR Perkin Elmer 1050+ spectrophotometer at INAM.

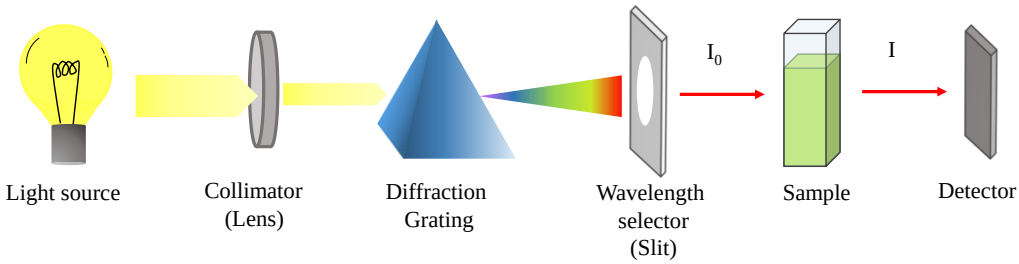

Figure 2.10. Schematic drawing of the optical a UV-Vis spectrophotometer array, in transmission configuration.

2.2.11 Photoluminescence spectroscopy

Fundamentals. Photoluminescence (PL) spectroscopy is a widely employed characterization technique for studying carrier dynamics in semiconductor materials. When a material is irradiated with light and the material absorbs photons, an electron from the ground state is promoted to higher energetic excited states. Then, the electron can relax back to its ground state emitting photons, fluorescence, or it can move to other excited state by intersystem crossing (ISC) and relax back to its ground state emitting phosphorescence. Both fluorescence and phosphorescence constitute the photoluminescence. **Figure 2.11** shows a scheme of the PL process. These radiative relaxation processes can be studied by using a PL spectrophotometer obtaining valuable information about electronic transitions and the structure of the material.[35] Different types of photoluminescence measurements can be combined to gain further insights on the optoelectronic properties. Steady-state PL provides emission spectrum when the material is constantly excited while in Time Resolved PL (TRPL) the material

is excited by a short pulse of light to study the decay of the photoluminescence as a function of time out of excitation to obtain the PL life-time of the sample.[36]

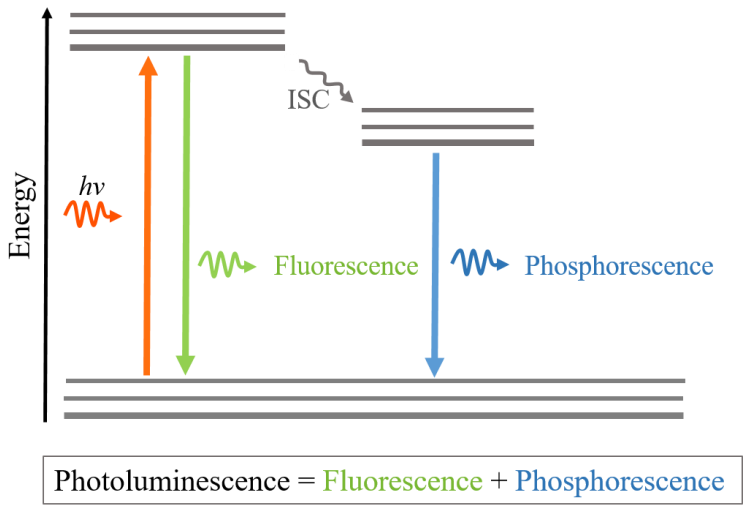

Figure 2.11. Schematic representation describing the PL process.

Sample preparation. No particular preparation of the sample is required beyond adjusting the volume of the measuring cuvette (for liquid solutions) or to the sample holder (for solid samples and thin films).

Equipment. Steady-state and time-resolved PL measurements were conducted through photoluminescence spectrophotometer Fluorolog 3-11, Horiba with an excitation wavelength of 420 nm. Time resolved PL measurements (TRPL) were carried out at 405 nm pulsed laser (NanoLED-405 L, <100 ps of pulse width, 1 MHz frequency) in Univesitat Jaume I.

2.3 Electrochemical and photoelectrochemical characterization

This section aims to describe electrochemical and photoelectrochemical techniques and explore their potential to perform chemical reactions while extracting information from electron transfer processes involved.

2.3.1 Electrochemical and photoelectrochemical fundamentals

Electrochemistry is the branch of chemistry that studies the interrelation of electrical and chemical effects. This relationship can occur in two directions, when an electric current leads to a chemical reaction or when a chemical reaction generates electricity. The former is the case this thesis focuses, by supplying electric current to an electrochemical system a particular chemical reaction is induced generating an electrical response. When the system is composed of a semiconductor with a suitable bandgap (discussed in *Section 1.4.1*), the electrochemical (EC) technique is light-assisted and is termed as photoelectrochemical (PEC) technique. Additionally, the chemical reactions studied by (photo)electrochemical techniques that involve electron transfers are called reduction-oxidation or redox reactions. All the investigation in this thesis focuses on electrochemical or photoelectrochemical processes.

To perform (photo)electrochemical measurements a setup consisting of (i) a simulated light source, (ii) EC or PEC cell and (ii) a potentiostat station is required. In **Figure 2.12** an experimental set up for EC and PEC measurements is schematized.

- *A simulated sunlight source* is the equipment that provides the light for PEC measurements. Typically, the PEC systems are studied under solar AM 1.5 G standard spectrum, referred to the annual average solar irradiance at mid-latitudes, after traveling through 1.5 times the thickness of the Earth atmosphere. The entire AM 1.5 G spectrum has a total integrated intensity of 100 mW cm^{-1} (1 sun).[37] Xenon lamps are widely used as a light source in solar simulators. Sometimes, it is useful to measure the photoelectrochemical response as a function of the light

intensity, filtering UV or interrupting lighting. For these purposes, light filters or a shutter can be used, respectively.

- *EC or PEC cell.* The cell is where the desired reaction occurs. It is configured around two or three electrodes in contact with a conductive solution. The cell could include one or two compartments and in the case of PEC measurements, a quartz window is necessary to maximize the fraction of light that can reach the sample by passing through the cell.
- *Potentiostat station.* The potentiostat is the pertinent equipment to supply the electrical current to the system and subsequently measure the electrical response. The potentiostat is coupled to a computer with an analysis software for data acquisition and processing. The potentiostat used for the experiments in the present thesis were Autolab potentiostat/galvanostat PGSTAT302.

Additional modules may be needed when coupling (P)EC to other techniques for example for the detection of products and quantification, or for *operando* characterization (*Section 2.4*). Other elements are recommended such as a Faraday cage to avoid external electromagnetic interferences.

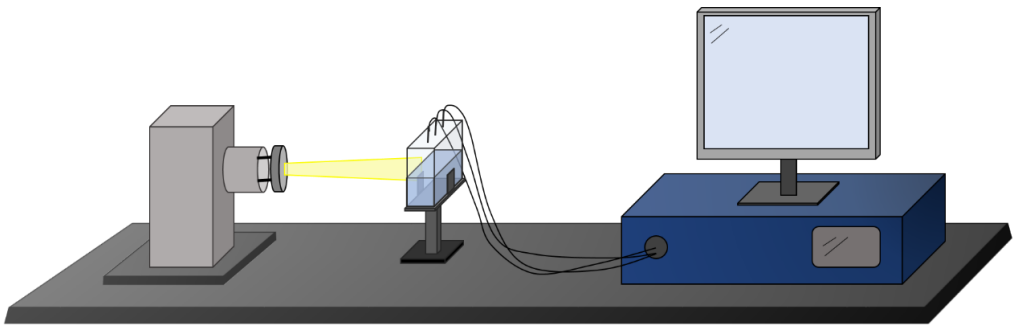

Figure 2.12. A representation of a PEC experimental setup.

2.3.2 (Photo)electrochemical cell

The (photo)electrochemical cell is the core of the electrochemical measurements. To correctly design a measure, it is necessary to know all the cell elements and their fundamentals. An EC or PEC cell consists of at least two electrodes to drive both the oxidation and reduction reactions. The working electrode (WE) is connected to the material of interest, the (photo)electrocatalyst and is where the desired reaction occurs. The counter electrode (CE) is where the opposite redox semirreaction takes place. However, to have a reference electrochemical scale, typically a third electrode called reference electrode (RE) is added. This RE have a fixed potential and negligible potential variations, independently of current to stabilize current fluctuations in the WE.

The electrodes are partially submerged in an ionic solution called electrolyte, the support medium where the reaction takes place. The electrolyte must be conductive, for this reason an inert salt dissolved in a solvent is usually used. The solvent could be an aqueous solvent: water or an organic solvent depending on the desired reaction, the solubility of the active species to be oxidized and reduced (dissolved or in its chemical nature) in it and the stability of the studied material when submerged. Whenever possible, the use of an aqueous medium is recommended since it is more economical and sustainable. The conductive salt will depend on the medium and the reaction, for example, in an aqueous medium, it is important to keep the pH constant, and thus buffers are usually used.

When aqueous electrolytes are used in (photo)electrochemical measurements, the most employed RE is the saturated silver/silver chloride electrode (Ag/AgCl, KCl sat.).[37] To standardize the results, in this thesis the potentials measured vs. Ag/AgCl are conveniently converted to the reversible hydrogen electrode (RHE) by using the following Nernst equation 2.4:

$$V_{RHE} = V_{Ag/AgCl} + V^0_{Ag/AgCl} + \frac{RT}{nF} \cdot pH \quad (2.4)$$

where $V_{Ag/AgCl}$ is the applied/recorded potential versus the reference, $V^0_{Ag/AgCl}$ is the standard potential of the Ag/AgCl redox couple, $\frac{RT}{nF}$ at room temperature is a constant value, 0.0591, and the pH is that of the electrolyte. Due to the potential dependence on the pH, the use of a buffer solution is strongly recommended to ensure a pH as constant as possible during the measurement. To choose the proper buffer, it is necessary to take into account the required pH conditions of each reaction and also the performance and stability.

For electrochemical measurements in organic electrolyte a non-aqueous RE is used. The most employed RE is the Ag/Ag^+ electrode, consisting of an Ag wire immersed in a solution of silver nitrate or perchlorate and a supporting salt in an organic solvent. Voltages vs Ag/Ag^+ can be standardized by converting them to Normal Hydrogen Electrode (NHE) by taking an internal standard Ferrocene/Ferrocenium (Fc/Fc^+) redox couple to calibrate the RE.[38]

In addition to the electrodes and the supporting electrolyte, it is important to choose the appropriate type of electrochemical cell. Although there is an increasing variety of cells and electrocatalytic systems, at least two considerations must be taken into account when designing the experiment. On the one hand, for PEC measurements, the cell or at least one window in the cell must be made of a material that allows light to enter the cell and pass through the working electrode. For the experiments included in this thesis, quartz cells and windows were used. On the other hand, sometimes it is convenient different conditions for each half-reaction (i.e. electrolyte, concentration or composition). To maintain no contact between the electrolyte in the anode (anolyte) and the electrolyte in the cathode (catholyte) and to avoid cross contamination issues a

two-compartment electrochemical cell is employed. A membrane is used as separator element to enhance the separation of reaction products, avoid their re-oxidation and strategically let the appropriate species pass through.[39-40] The specific type of membrane will depend on the specific testing conditions. **Figure 2.13** shows an scheme of a two-compartment electrochemical cell.

The particular cell design and arrangement, RE, CE and electrolytes in each of the investigations reported in this thesis will be detailed in the corresponding chapter.

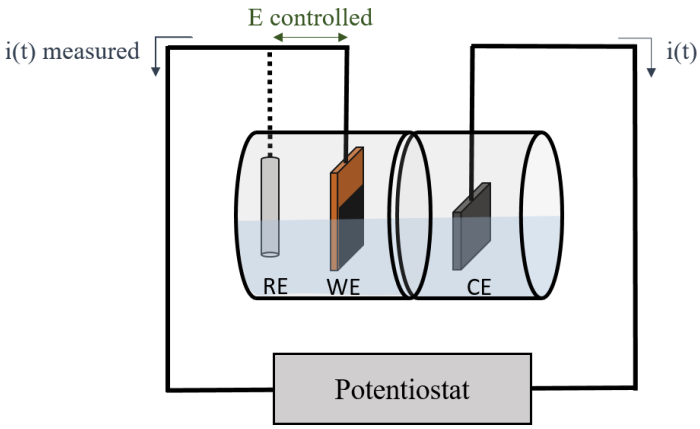

Figure 2.13. Representation of an experimental setup of a potentiostat applying voltage to a two-compartment electrochemical electrochemical cell.

2.3.3 (Photo)electrochemical measurements

In this part, the (photo)electrochemical measurements performed in this thesis are described. Current density-voltage (j-V) methods consists of forcing the electrode to adhere to a potential or current while the respective current or potential that has been generated is recorded respectively.

- **Cyclic voltammetry and linear sweep voltammetry**

Cyclic voltammetry (CV) is the first technique that is generally applied to any electrochemical system to evaluate its performance. It provides useful functional and mechanistic information on the system at stage. The electrode potential is swept from an initial potential V0 to a V1 turn potential and then, it is scanned back to the original potential V0. This gives a triangular potential cycle. In Linear sweep voltammetry (LSV), the electrode potential is only swept from an initial V0 to a final V1 point and no back scan is carried out. When measuring PEC, j-V curves must be performed both with and without illumination (dark current density) to properly study the photoactivity of the material.

- **Tafel slope analysis**

With a convenient LSV it is possible to gain insights on both activity and kinetics of the electrochemical reaction at the same time by means of Tafel slope analysis.[41] Its bases lie on the current–potential relationship for a simple redox reaction which follows the Butler–Volmer equation (2.5):

$$j = j_0 \cdot exp\frac{\alpha F \eta}{RT} \tag{2.5}$$

Where j and j_0 are the current density and exchange current density, respectively, α is the transfer coefficient for the anodic reaction, F the Faraday constant, η is the ovepotential, R is the universal gas constant and T is the absolute temperature. Applying a logarithmic function to equation (2.5), equation (2.6) is obtained:

$$\log(j) = \log(j_0) + \frac{\eta}{b} \tag{2.6}$$

And from (2.6) the lineal equation (2.7):

$$\eta = a + b \cdot \log(j) \tag{2.7}$$

Using equation (2.7) representing the overpotential Ƞ vs log (j), the Tafel slope (b) is obtained expressed in units of millivolts (mV) per decade of current density (dec^{-1}). This value indicates how fast the reaction rate is, the lower the value of the slope, the faster the reaction occurs. In the particular case of the HER, different reaction mechanisms for hydrogen generation have been described and ascribed to specific values of Tafel slope.[42] However, it is important to point out that these assignments were attributed to perfect metallic systems such as Pt, a reference noble metal for H_2 generation, and that when other non-ideal systems are studied it is not convenient to make this assignment of mechanisms.[41, 43-44] Nonetheless, Tafel slope analysis is a simple and effective way to determine reaction rates.

- **Chronoamperometric and chronopotentiometric methodes**

Another well-used electrochemical method is when the potential is fixed and the current is recorded as a function of time: chronoamperometries (CA) or those in which the current is fixed and the voltage is recorded as a function of time: chronopotentiometries (CP). It is during these measurements that the studied reaction is performed. Additionally, CA and CP are also used to evaluate the stability of an electrode. These measurements are important since stability is one of the most important requirements for the scalability of a material.

- **Faraday's law calculations**

By the application of the **Faraday's law** it is possible to quantify the chemical transformations taking place during an electrochemical process. For process where the charge is transferred to the electrolyte and it is not a capacitive/redox process, the moles of the produced/consumed substance (n_i) are directly

proportional to the amount of the measured electric charge (Q) according with the equation (2.8)

$$n_i = \frac{Q}{n_e F} \tag{2.8}$$

where n_e is the number of electrons exchanged in the reaction and F is the Faraday constant (9648 C·mol^{-1}).[45] Since the charge is the product of the intensity of current recorded (during CA) or applied (during CP), the total theoretical moles of product in a (photo)electrochemical reaction is calculated according to the expression (2.9):

$$n_{th} = \frac{Q_T}{n_e F} = \frac{\int I \cdot t}{n_e F} = \frac{\sum I \cdot \Delta t}{n_e F} \tag{2.9}$$

- **Impedance spectroscopy (IS)**

Impedance spectroscopy (IS) or electrochemical impedance spectroscopy (EIS) is a useful complementary tool for understanding charge carrier dynamics and limitations for the performance of (photo)electrochemical reactions. EIS is classified in the group of small perturbation techniques in which, while applying a DC voltage, a small AC signal perturbs the sample scanning multiple frequencies (ω). In other words, a sinusoidal potential is applied to the system and the frequency-dependent complex impedance (Z) is measured. This impedance is expressed:

$$Z(\omega) = \frac{V(\omega)}{I(\omega)} \tag{2.10}$$

Typically, the results are represented as Nyquist and Bode plots (see **Figure 2.14**). The Nyquist plot represents the complex plane −imaginary impedance Z'' *versus* its real-value counterpart Z' while the Bode plots graphs the module of

the capacitance (E') *versus* frequency.[46] Impedances are usually measured at several potential values of the steady-state LSV curve, revealing specific kinetic and charge storage properties under the electrochemical reaction.

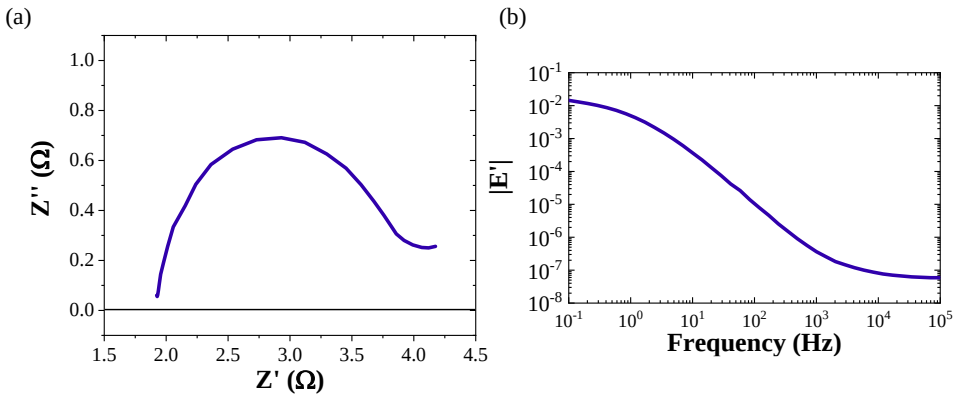

Figure 2.14. Impedance spectra measurements: (a) Nyquist plot and (b) Bode plot obtained with $Cu_{2-x}S$ electrocatalyst for HER.

For EIS analysis, a convenient equivalent circuit model (ECM) needs to be selected integrating the overall processes occurring in the cell, namely, in the catalyst, in the electrolyte and in the catalyst-electrolyte interface. Then, the EIS data are fitted according to the ECM, providing information of basic electronic processes of charge transfer, accumulation and recombination, which are related to circuit elements as resistances and capacitances. The resistances are associated to carrier transport, either inside the semiconductor or at the interfaces. The total dc resistance R_{dc}, corresponds to the real value of the impedance when $\omega = 0$, considering the geometrical area of the electrode (A) according to expression (2.11):

$$R_{dc} = (A\frac{dj}{dV})^{-1} \qquad (2.11)$$

The capacitance, refers to the specific charge storage mechanism and can be a dielectric capacitance, associated to an internal electrical field induced by a spatial charge separation or a chemical capacitance, resulting from varying the chemical potential, or the carrier concentration.

For the EIS analyses carried out in this thesis in *Chapter 4*, the simplest ECM was used named Randles' circuit. This Randles' circuit (**Figure 2.15**) consists of a series resistance (R_s) with a parallel association of a capacitance (C) and a resistance generally accounting for charge transfer processes (R_{ct}).[46-47]

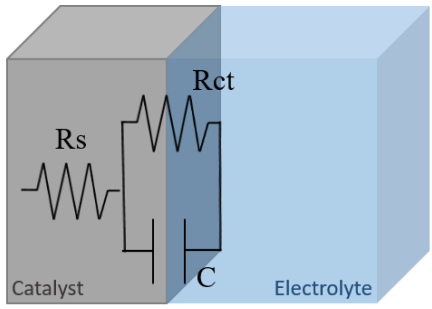

Figure 2.15. Representation of a Randles' circuit integrating its experimental representation: R_s includes the contribution of the electrolyte, contacts and connection wires, and is directly extracted from the high frequency intercept (Z''= 0)., R_{ct} is the resistance that relates to the charge transfer at the interface of the electrode and the electrolyte, and C is the capacity that refers to the accumulation of charges at the electrode.

The capacitances represent a charge storage mechanism. They can be divided into two types: (i) the dielectric capacitance, associated to an internal electrical field produced by a spatial charge separation and (ii) the chemical capacitance, resulting from the variation of the chemical potential, or carrier concentration. Typically, a non-ideal capacitance response is observed, therefore, a constant-phase element (CPE) is used instead of a pure capacitance element.

Note that the interpretation of impedance data implies assuming the assignment of a circuit according to the main reaction but other contributions and phenomena such as corrosion or parasitic reactions may take place. Consequently, although EIS do not provide a phenomenological interpretation of the charge transfer processes involved, it allows to identify and quantify resistances and capacities that are related with the main phenomena occurring during EC.[48]

- **Double-layer capacitance**

As previously described, through EIS analysis it is possible to determine capacitive effects during EC. Between the electrode surface and the electrolyte, a capacitive process takes place as depicted in **Figure 2.15**.[49-50]

By measuring impedance at non-Faradaic region, which means where no apparent Faradaic processes occur, while applying high frequencies, the obtained C is related to the double-layer capacitance. The relationship between the impedance and the capacitance is described by equation (2.12):

$$Z_{CPE} = \frac{1}{Q_0(i\omega)^{1-\alpha}} \tag{2.12}$$

where, $i=(-1)^{1/2}$, Q_0 is a constant with units of F $s^{\alpha-1}$, and $1 \geq \alpha \geq 0$ is related to the phase angle of the frequency response. For the Randles' circuit used in this thesis, the double layer capacitance C_{DL}, is determined by equation (2.13)

$$C_{DL} = [Q_0 \left(\frac{1}{R_S} + \frac{1}{R_{ct}}\right)^{(\alpha-1)}]^{1/\alpha} \tag{2.13}$$

- **Electrochemically active surface area**

The electrochemically active surface area (ECSA) of a catalyst indicates the total electrode surface involved in the electrocatalytic process. Specifically,

ECSA indicates the active catalytic surface of the material, compared to the perfectly flat surface of given catalyst material. ECSA can be extracted by the double layer capacitance (C_{DL}) through the following expression (2.14):

$$ECSA = \frac{C_{DL}}{C_S} \tag{2.14}$$

where C_S corresponds to the specific capacitance of the sample or the capacitance of an atomically smooth planar surface of the material per unit area under identical electrolyte conditions.[51] In real systems, it is generally difficult to obtain a precise C_S value of a material and for this reason, in Chapter 4 an ECSA ratio for subsequent measurements was calculated instead of specific ECSA value. Dividing the expression (2.14) of each measurement with its subsequent one, the denominator is cancelled, being able to quantify an increase or decrease in the ECSA without compromising the C_S value.

2.4 *Operando, in-situ* and *quasi-in-situ* characterization

The characterization of the catalyst structure and composition before and post-reaction is very useful to study the changes in the material, however it is not representative of the dynamic changes that take place during the operation conditions. Therefore, *in-situ*/*operando* characterization provides more reliable information, essential to properly study the overall reaction. The term *in-situ* refers to characterization under reaction conditions while the term *operando* stands for simultaneous measurements under the catalytic operation, while applying current/voltage and producing the desired products. Both of them are powerful tools to understand the reaction mechanisms and electrochemically active species.[52-53]

In this thesis three *operando* techniques were performed to understand the activity of the $Cu_{2-x}S$ electrocatalyst and possible compositional and morphological changes and for studying reaction intermediates and mechanisms. The *operando* techniques used are:

- Spectroelectrochemistry (SEC). For SEC, electrochemical measurements are performed together with UV-Vis spectroscopy (described in section 2.2.9). Through this technique, it is possible to extract very valuable information about intermediates and structural dynamics.[54-55] In Chapter 4, SEC was used to determine the catalytically active species. This easy-to-use and relatively affordable technique provides valuable and consistent insights.
- *Operando XRD*. The correlation between the structure changes and electrochemical performance of the electrocatalyst can be systematically studied by measuring *operando* XRD of the electrocatalyst under bias. From the collection of diffractograms of the electrocatalyst and its immediate surroundings under operation conditions, valuable information can be extracted such as catalyst composition, oxidative states and crystallinity.[56] In this thesis, *operando* XRD is used to characterize the crystalline structure of the catalyst during the reaction. It was carried out by our collaborators from the Université de Montréal in Canada and more information is detailed in *Chapter 4.*
- *Operando Raman*. Raman spectroscopy characterization (section 2.2.8) coupled to electrochemistry is a very useful tool to study the molecular structures and reaction intermediates on the electrode–electrolyte interface with a low scattering cross-section for water.[57] *Operando*

Raman was measured for the carbon dioxide reduction reaction in *Chapter 5* in collaboration with the Université de Montréal in Canada.

Likewise, EIS is also considered an operando technique, since other parameters can be studied simultaneously to the reaction (determination of C_{DL} and ECSA ratio in *Chapter 4*).

Finally, *quasi-in-situ* characterization refers to that characterization of the material performed outside the operating conditions but trying to preserve the sample as it was under operation. This approach allows performing multiple characterization techniques without complex and expensive set-ups.

In the development of this thesis, quasi-in-situ XPS and XRD measurements were carried out after electrochemistry. For this purpose, two types of sample transfer from the electrochemical cell to the characterization equipment were designed isolating the sample from contact with air. On the one hand, the transfer in nitrogen atmosphere was used for *quasi-in-situ* XPS measurements and on the other hand, a sample sealing system was carried out to measure *quasi-in-situ* XRD (conveniently detailed in *Chapters 4* and *Chapter 5* respectively). These transfer strategies protect the catalyst from oxidizing when exposed at air, maintaining its composition as faithful as possible to the specifications.

2.5 Products determination and quantification techniques

All the electrochemical reactions presented in this thesis were analytically monitored by chromatographic techniques to identify and quantify the generated products and therefore the catalyst efficiency.

2.5.1 Gas chromatography

Fundamentals. Gas chromatography (GC) is the most common analytical technique used to separate, identify and quantify volatile compounds in a sample mixture. During the separation process, the gaseous or liquid samples pass through a column (stationary phase) at a certain temperature pushed by a mobile phase, typically called the carrier gas. The carrier gas is usually an inert gas or an unreactive gas such as He, Ar, N or H_2. Commonly, the most used detectors are the thermal conductivity detectors (TCD). The generated chromatograms show a voltage response for each compound eluted from the column as function of retention time.

Additionally, the sample can be injected as an isolated aliquot or in continuous flow when the GC is coupled to a reactor, in our case to an electrochemical cell. Online injection from the cell is the most accurate method to obtain product detection and quantification during the reaction.

Sample preparation. In this section, we consider the sample the gaseous mixture in which we want to detect the products: the headspace in the cell. Before GC measurements for products quantification, it is crucial to properly purge the cell with the carrier gas to start with a blank flat chromatogram.

Equipment. The gas chromatography measurements were carried out in an Agilent Micro-GC gas chromatograph coupled to a sealed cell. More detailed specifications and quantification calculations are provided in *Chapter 4* and *Chapter 5.*

2.5.2 High performance liquid chromatography

Fundamentals. High performance liquid chromatography (HPLC) is an analytical technique employed to separate the individual components of interest present in mixture and/or dissolved in sample liquid solution. The operating principle of HPLC consists of flowing a sample/aliquot through a column packed with a separation medium (stationary phase). The aliquot is pushed through the column by using a stream of solvent (mobile phase) pumped at high pressure. Depending on the affinity of the column for retaining compounds, the components of the sample will be eluted from the column in a specific order and flowing to the detectors, which deliver a voltage response as a function of time called chromatogram. Each of the peaks conforming the chromatogram can be identified and quantified by comparison with a standard.[58]

Sample preparation. In this section we consider the sample the liquid solution in which we want to detect the products: the electrolyte. The sample solution should be carefully filtered with the appropriate filters before measurement to avoid clogging problems.

Equipment. The products quantification in *Chapter 5* and *Chapter 6* were performed on a HPLC Agilent 1260 Infinity II LC System provided with a Diode Array Detector (DAD) and a Refractive Index Detector (RID). With an ion-exchange ligand-exchange column, Agilent Hi-Plex.

2.5.3 Faradaic efficiency

Faradaic efficiency (FE) describes the overall selectivity of an electrochemical process and is defined as the experimental moles (n_{exp}) of evolved product relative to the theoretical moles (n_{th}) expressed as a fraction or a percent.[59-60]

$$\%FE = \frac{n_{exp}}{n_{th}} \cdot 100 \quad (2.15)$$

Theoretical moles (n_{th}) are calculated from the charge (Q) applying faraday law (see *Section 2.3.3),* and experimental moles (n_{exp}), for both chromatographic techniques, are determined integrating the area of the desired peak in the chromatogram and extrapolating from an external calibration curve. Through the FE, it is possible to quantitatively determine the selectivity of a catalyst for a certain reaction.

2.6 References

1. Feng, S.; Xu, R., New materials in hydrothermal synthesis. *Accounts of chemical research* **2001,** *34* (3), 239-247.

2. Gan, Y. X.; Jayatissa, A. H.; Yu, Z.; Chen, X.; Li, M., Hydrothermal synthesis of nanomaterials. *Journal of Nanomaterials* **2020,** *2020*, 1-3.

3. Zuo, C.; Scully, A. D.; Vak, D.; Tan, W.; Jiao, X.; McNeill, C. R.; Angmo, D.; Ding, L.; Gao, M., Self-assembled 2D perovskite layers for efficient printable solar cells. *Advanced Energy Materials* **2019,** *9* (4), 1803258.

4. Zuo, C.; Ding, L., Drop-casting to make efficient perovskite solar cells under high humidity. *Angewandte Chemie* **2021,** *133* (20), 11342-11346.

5. Wang, L.; Wu, L.; Wang, Y.; Luo, J.; Xue, H.; Gao, J., Drop casting based superhydrophobic and electrically conductive coating for high performance strain sensing. *Nano Materials Science* **2022,** *4* (2), 178-184.

6. Shrestha, N. K.; Patil, S. A.; Cho, S.; Jo, Y.; Kim, H.; Im, H., Cu–Fe–NH 2 based metal–organic framework nanosheets via drop-casting for highly efficient oxygen evolution catalysts durable at ultrahigh currents. *Journal of Materials Chemistry A* **2020,** *8* (46), 24408-24418.

7. Patil, S. A.; Shrestha, N. K.; Inamdar, A. I.; Bathula, C.; Jung, J.; Hussain, S.; Nazir, G.; Kaseem, M.; Im, H.; Kim, H., Bimetallic Cu/Fe MOF-based nanosheet film via binder-free drop-casting route: a highly efficient urea-electrolysis catalyst. *Nanomaterials* **2022,** *12* (11), 1916.

8. Ma, J.; Song, C.; Chen, S.; Xu, Y.; Du, H., Drop-casting preparation of a binder-free SiOx anode with micron-sized SiOx particles for high-performance lithium-ion batteries. *Journal of Alloys and Compounds* **2022,** *918*, 165682.

9. Eslamian, M.; Soltani-Kordshuli, F., Development of multiple-droplet drop-casting method for the fabrication of coatings and thin solid films. *Journal of Coatings Technology and Research* **2018,** *15* (2), 271-280.

10. de Mello Donegá, C.; Liljeroth, P.; Vanmaekelbergh, D., Physicochemical evaluation of the hot-injection method, a synthesis route for monodisperse nanocrystals. *Small* **2005,** *1* (12), 1152-1162.

11. Soni, A. K.; Joshi, R.; Ningthoujam, R. S., Hot injection method for nanoparticle synthesis: basic concepts, examples and applications. *Handbook on Synthesis Strategies for Advanced Materials: Volume-I: Techniques and Fundamentals* **2021**, 383-434.

12. Le, Q. V.; Hong, K.; Jang, H. W.; Kim, S. Y., Halide perovskite quantum dots for light-emitting diodes: properties, synthesis, applications, and outlooks. *Advanced Electronic Materials* **2018,** *4* (12), 1800335.

13. Sahu, N.; Parija, B.; Panigrahi, S., Fundamental understanding and modeling of spin coating process: A review. *Indian Journal of Physics* **2009,** *83* (4), 493-502.

14. Ferdaus, M. M.; Rashid, M. M.; Rahman, M. A., Design and fabrication of a simple cost effective spin coater for deposition of thin film. *Adv. Environ. Biol* **2014,** *8* (3), 729-733.

15. Inkson, B. J., Scanning electron microscopy (SEM) and transmission electron microscopy (TEM) for materials characterization. In *Materials characterization using nondestructive evaluation (NDE) methods*, Elsevier: 2016; pp 17-43.

16. Abd Mutalib, M.; Rahman, M. A.; Othman, M. H. D.; Ismail, A. F.; Jaafar, J., Scanning electron microscopy (SEM) and energy-dispersive X-ray (EDX) spectroscopy. In *Membrane characterization*, Elsevier: 2017; pp 161-179.

17. Goldstein, J. I.; Newbury, D. E.; Michael, J. R.; Ritchie, N. W. M.; Scott, J. H. J.; Joy, D. C., *Scanning electron microscopy and X-ray microanalysis*. springer: 2017.

18. Spence, J. C. H., *High-resolution electron microscopy*. OUP Oxford: 2013.

19. Muller, A.; Grazul, J., Optimizing the environment for sub-0.2 nm scanning transmission electron microscopy. *Journal of electron microscopy* **2001,** *50* (3), 219-226.

20. Egerton, R. F., Electron energy-loss spectroscopy in the TEM. *Reports on Progress in Physics* **2008,** *72* (1), 016502.

21. Otten, M. T., High-Angle annular dark-field imaging on a tem/stem system. *Journal of electron microscopy technique* **1991,** *17* (2), 221-230.

22. Eaton, P.; West, P., *Atomic force microscopy*. Oxford university press: 2010.

23. Butt, H.-J.; Graf, K.; Kappl, M., *Physics and chemistry of interfaces*. John Wiley & Sons: 2023.

24. Hu, Y.; Chen, Q.; Feng, S.; Zuo, C., Microscopic fringe projection profilometry: A review. *Optics and lasers in engineering* **2020,** *135*, 106192.

25. Gallagher, J. C.; Mastro, M. A.; Ebrish, M. A.; Jacobs, A. G.; Gunning, B. P.; Kaplar, R. J.; Hobart, K. D.; Anderson, T. J., Using machine learning with optical profilometry for GaN wafer screening. *Scientific Reports* **2023,** *13* (1), 3352.

26. Nayak, B. B.; Jena, H.; Dey, D.; Oda, B. K.; Chetia, A.; Brahma, S. K.; Bordoloi, T.; Chakraborty, D., Materials selection and design analysis of cryogenic pressure vessel: A review. *Materials Today: Proceedings* **2021,** *47*, 6605-6608.

27. Bunaciu, A. A.; UdriŞTioiu, E. G.; Aboul-Enein, H. Y., X-ray diffraction: instrumentation and applications. *Critical reviews in analytical chemistry* **2015,** *45* (4), 289-299.

28. Ali, A.; Chiang, Y. W.; Santos, R. M., X-ray diffraction techniques for mineral characterization: A review for engineers of the fundamentals, applications, and research directions. *Minerals* **2022,** *12* (2), 205.

29. Stevie, F. A.; Donley, C. L., Introduction to x-ray photoelectron spectroscopy. *Journal of Vacuum Science & Technology A* **2020,** *38* (6).

30. Hubbard, A. T., *The Handbook of surface imaging and visualization*. CRC press: 2022.

31. Jones, R. R.; Hooper, D. C.; Zhang, L.; Wolverson, D.; Valev, V. K., Raman techniques: fundamentals and frontiers. *Nanoscale research letters* **2019,** *14*, 1-34.

32. Luo, R.; Popp, J.; Bocklitz, T., Deep learning for Raman spectroscopy: a review. *Analytica* **2022,** *3* (3), 287-301.

33. Rocha, F. S.; Gomes, A. J.; Lunardi, C. N.; Kaliaguine, S.; Patience, G. S., Experimental methods in chemical engineering: Ultraviolet visible spectroscopy—UV-Vis. *The Canadian Journal of Chemical Engineering* **2018,** *96* (12), 2512-2517.

34. Vogt, C.; Wondergem, C. S.; Weckhuysen, B. M., Ultraviolet-Visible (UV-Vis) Spectroscopy. In *Springer Handbook of Advanced Catalyst Characterization*, Springer: 2023; pp 237-264.

35. Handa, T.; Yamada, T.; Kanemitsu, Y., Photoluminescence Characterization of Halide Perovskite Materials and Solar Cells. *ECS Journal of Solid State Science and Technology* **2023,** *12* (5), 056004.

36. Kirchartz, T.; Márquez, J. A.; Stolterfoht, M.; Unold, T., Photoluminescence-based characterization of halide perovskites for photovoltaics. *Advanced energy materials* **2020,** *10* (26), 1904134.

37. van de Krol, R., Photoelectrochemical measurements. In *Photoelectrochemical hydrogen production*, Springer: 2011; pp 69-117.

38. Saheb, A.; Janata, J.; Josowicz, M., Reference electrode for ionic liquids. *Electroanalysis: An International Journal Devoted to Fundamental and Practical Aspects of Electroanalysis* **2006,** *18* (4), 405-409.

39. Merino-Garcia, I.; Alvarez-Guerra, E.; Albo, J.; Irabien, A., Electrochemical membrane reactors for the utilisation of carbon dioxide. *Chemical Engineering Journal* **2016,** *305*, 104-120.

40. Park, J.; Ko, Y.-j.; Lim, C.; Kim, H.; Min, B. K.; Lee, K.-Y.; Koh, J. H.; Oh, H.-S.; Lee, W. H., Strategies for CO2 electroreduction in cation exchange membrane electrode assembly. *Chemical Engineering Journal* **2023,** *453*, 139826.

41. Anantharaj, S.; Noda, S.; Driess, M.; Menezes, P. W., The Pitfalls of Using Potentiodynamic Polarization Curves for Tafel Analysis in Electrocatalytic Water Splitting. *ACS Energy Letters* **2021,** *6* (4), 1607-1611.

42. Murthy, A. P.; Theerthagiri, J.; Madhavan, J., Insights on Tafel constant in the analysis of hydrogen evolution reaction. *The Journal of Physical Chemistry C* **2018,** *122* (42), 23943-23949.

43. Anantharaj, S.; Noda, S., How properly are we interpreting the Tafel lines in energy conversion electrocatalysis? *Materials Today Energy* **2022,** *29*, 101123.

44. Shinagawa, T.; Garcia-Esparza, A. T.; Takanabe, K., Insight on Tafel slopes from a microkinetic analysis of aqueous electrocatalysis for energy conversion. *Scientific reports* **2015,** *5* (1), 13801.

45. Lefrou, C.; Fabry, P.; Poignet, J.-C., *Electrochemistry: the basics, with examples*. Springer Science & Business Media: 2012.

46. Bisquert, J.; Giménez, S.; Bertoluzzi, L.; Herraiz-Cardona, I., Analysis of photoelectrochemical systems by impedance spectroscopy. *Photoelectrochemical solar fuel production: from basic principles to advanced devices* **2016**, 281-321.

47. Macdonald, J. R.; Johnson, W. B., Fundamentals of impedance spectroscopy. *Impedance spectroscopy: theory, experiment, and applications* **2018**, 1-20.

48. Lopes, T.; Andrade, L.; Ribeiro, H. A.; Mendes, A., Characterization of photoelectrochemical cells for water splitting by electrochemical impedance spectroscopy. *international journal of hydrogen energy* **2010,** *35* (20), 11601-11608.

49. Haid, R. W.; Ding, X.; Sarpey, T. K.; Bandarenka, A. S.; Garlyyev, B., Exploration of the electrical double-layer structure: Influence of electrolyte components on the double-layer capacitance and potential of maximum entropy. *Current Opinion in Electrochemistry* **2022,** *32*, 100882.

50. Trasatti, S.; Petrii, O. A., Real surface area measurements in electrochemistry. *Pure and applied chemistry* **1991,** *63* (5), 711-734.

51. McCrory, C. C. L.; Jung, S.; Peters, J. C.; Jaramillo, T. F., Benchmarking heterogeneous electrocatalysts for the oxygen evolution reaction. *Journal of the American Chemical Society* **2013,** *135* (45), 16977-16987.

52. Kornienko, N., Operando spectroscopy of nanoscopic metal/covalent organic framework electrocatalysts. *Nanoscale* **2021,** *13* (3), 1507-1514.

53. Yang, Y.; Xiong, Y.; Zeng, R.; Lu, X.; Krumov, M.; Huang, X.; Xu, W.; Wang, H.; DiSalvo, F. J.; Brock, J. D., Operando methods in electrocatalysis. *ACS Catalysis* **2021,** *11* (3), 1136-1178.

54. Best, S.; Murray, P.; Dhungana, S.; Crumbliss, A. L.; Dunsch, L.; Haga, M.-a.; Hartl, F.; Kubiak, C. P.; Winter, R.; Yellowlees, L. J., *Spectroelectrochemistry*. Royal Society of Chemistry: 2008.

55. Mesa, C. A.; Pastor, E.; Francàs, L., UV-Vis operando spectroelectrochemistry for (photo) electrocatalysis: principles and guidelines. *Current Opinion in Electrochemistry* **2022**, 101098.

56. Wei, X.; Wang, X.; An, Q.; Han, C.; Mai, L., Operando X-ray diffraction characterization for understanding the intrinsic electrochemical mechanism in rechargeable battery materials. *Small Methods* **2017,** *1* (5), 1700083.

57. Chen, M.; Liu, D.; Qiao, L.; Zhou, P.; Feng, J.; Ng, K. W.; Liu, Q.; Wang, S.; Pan, H., In-situ/operando Raman techniques for in-depth understanding on electrocatalysis. *Chemical Engineering Journal* **2023,** *461*, 141939.

58. Akash, M. S. H.; Rehman, K.; Akash, M. S. H.; Rehman, K., High performance liquid chromatography. *Essentials of pharmaceutical analysis* **2020**, 175-184.

59. Fuller, T. F.; Harb, J. N., *Electrochemical engineering*. John Wiley & Sons: 2018.

60. Kempler, P. A.; Nielander, A. C., Reliable reporting of Faradaic efficiencies for electrocatalysis research. *Nature Communications* **2023,** *14* (1), 1158.

Chapter 3

Synthesis of nanoporous $Cu_{2-x}S$ electrocatalyst

Chapter 3 describes the optimized experimental process by which copper sulfide ($Cu_{2-x}S$) films were synthesized for their subsequent application as electrocatalysts driving the hydrogen evolution reaction (*Chapter 4*) and the electrochemical CO_2 reduction reaction (*Chapter 5*). Likewise, a comprehensive compositional and structural characterization of the prepared films is presented. By combining different characterization techniques including EDS, HRTEM, XRD and XPS, the formation of 6 µm thick $Cu_{2-x}S$ electrodes could be confirmed. Interestingly, the SEM images revealed a highly porous $Cu_{2-x}S$ structure, typical of foamy materials, beneficial for electrocatalytic applications.

3.1 Introduction

Traditionally, noble metals such as Pt and Ru are considered the most efficient electrocatalytic materials for the HER.[1-2] However, their scarcity and high cost hinders their large scale deployment.[3] More recently, electrocatalysts based on earth-abundant and cost-effective materials, such as Ni[4-5], Co[6], Mo[7], Fe[8-9] and Cu[10-11] have been reported as suitable electrocatalysts for different applications.

In particular, copper oxides and copper chalcogenides are attracting increasing attention due to the copper multiple oxidation states, good redox kinetics and rich

coordination chemistry. In this chapter, a facile, cost-effective and scalable synthetic route to prepare $Cu_{2-x}S$ electrocatalysts is reported.

3.2 Synthesis optimization

Copper sulfide films were prepared by modifying a previously reported synthetic route.[12] Through the original procedure, Cu_2S is grown on a brass gauze by inmmersing the brass in a 1.3 M sodium tetrasulfide solution. The tetrasulfide solution (Na_2S_4) is obtained by dissolving $Na_2S{\cdot}9H_2O$ in an aqueous NaOH solution and subsequently adding S.[13] To completely dissolve the reagents, the mixture is heated for 3 hours at 313 K with magnetic stirring, while constant bubbling with purified nitrogen. Then, the Na_2S_4 solution is boiled and the brass gauze is immersed for 15 min,[14] where it gradually blackens. Finally, the synthetized electrode is rinsed with deionized water and air-dried. However, with the aim of designing suitable and reproducible electrodes for the reactions addressed in this thesis, some parameters of this synthetic process, which include the selected substrate, the concentration of the reactants and the duration time, were modified and detailed below.

- *The substrate.*

A brass gauze was used as the reactive substrate for the copper sulfide formation in the original synthesis, due to the mechanical integrity that Zn potentially provides in the alloy. However, a bare metallic Cu foil was chosen as the substrate for the modified synthesis for two main reasons. On the one hand, larger copper surface areas expose major density of Cu active sites available for the copper sulfidization facilitating the Cu_2S formation process. On the other hand, metallic Cu has been widely studied for CO_2 electrochemical reduction due to its suitability to form several CO_2 reduction products.[15] Since the electrochemical

reduction of CO_2 is one of the target reactions of this thesis, Cu foil was selected as a suitable substrate for the $Cu_{2-x}S$ synthesis. Additionally, the use of Cu foil triggered a more complete study of the material, by comparing the catalytic performance of the bare Cu foil *versus* $Cu_{2-x}S$ on Cu foil and providing useful Cu blanks in different experimental analyses.

- *Molar Na_2S_4 solution concentration.*

The amounts of the reagents for preparing the polysulfide reaction solution were readjusted by quantitatively minimizing the concentrations, while guaranteeing the formation of the copper sulfide after the synthesis.

- *The reaction time.*

According with the reported 15 min reaction time for the synthesis of the electrodes, initially, the Cu_2S electrodes were synthesized by immersing a copper foil for 15 min in the polysulfide solution, As a result, a black layer of several tens of micrometres thick grew very fast on the Cu substrate. The resulting electrodes were compositionally and structurally characterized by XRD and SEM and electrochemically evaluated for the electrochemical reduction of CO_2.

Figure 3.1 shows the XRD and SEM analysis of the as-synthetized electrodes. The X-ray diffraction spectrum in **Figure 3.1a** exhibits well-defined peaks at 2θ values of 26.1°, 27.84°, 32.23°, 46.17°, 48.85°, 55° in good agreement with the formation of $Cu_{1.8}S$ (JCPDS Card No. 24-61). Two additional minor peaks are observed at 2θ values of 36.5° and 42.4° are assigned to the formation of Cu_2O on the electrodes surface due to air exposure during and after the synthesis (JCPDS Card No. 03-0898). The characteristic peaks from the metallic Cu substrate at 43.25° and 53.35° (JCPDS Card No. #04-0836) are also and indexed to the (111) and (200) crystal planes, respectively.

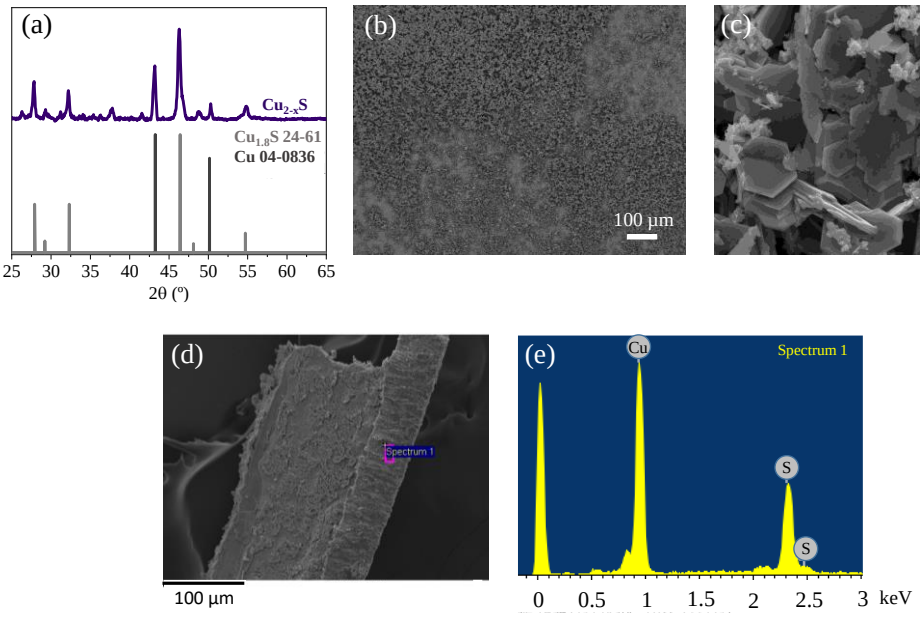

Figure 3.1. Structural, compositional and morphological characterization of the Cu_2S electrodes. (a) Indexed X-ray diffractogram of the as-synthetized electrode measured in grazing incidence mode. (b-c) Top-view SEM images at different magnification. (d) Cross-sectional SEM image and (e) EDS spectrum of the area delimited in (d).

The morphological analysis of the as-synthetized electrodes were investigated by scanning electron microscopy (SEM). **Figure 3.1b** and **Figure 3.1b** show top-view SEM images of the electrode at different magnifications. **Figure 3.1b** offers a global view of the electrode, which shows a rough and porous formation completely covering the surface of the substrate. At a higher magnification, it is possible to distinguish different crystalline structures (**Figure 3.1c**) among which the presence of micro-hexagons consistent with the formation of Cu_2S can be identified.[16] Further cross-sectional SEM images were analysed to estimate the thickness of the Cu_2S layer. Since it was not possible to fracture the copper foil without edge effect due to its malleability, a cross-sectional SEM image of a carefully delaminated piece of the Cu_2S layer was satisfactorily characterized in **Figure 3.1d** and a thickness around 60 µm was determined. Additional energy dispersive X-ray analysis (EDS) was carried out to investigate the elemental

composition of the synthesized material (**Figure 3.1d**). The EDS analysis reveals the presence of Cu and S with a Cu-S ratio of 1.75 (**Figure 3.1e** and **Table 3.1**). According with the XRD, SEM and EDS results, the material was conclusively characterized as $Cu_{2-x}S$, including in this denomination the different forms that the $Cu_{2-x}S$ with small x value ($0 < x < 1$) can exists.[17]

Table 3.1. EDS quantification of the Cu_2S electrodes (spectrum from **Figure 3.1e**).

Element	Weight [%]	Atomic [%]
Cu (L line)	77.63	63.65
S (K line)	22.37	36.35
Totals	100.00	

The as-synthetized $Cu_{2-x}S$ electrodes were tested electrochemically to evaluate their applicability (**Appendix I, Figure A3.1** and **Figure A3.2**). During the electrochemical measurements and subsequent manipulation of the electrode, an overgrowth of the $Cu_{2-x}S$ resulted in large material losses due to mechanical detachment. Consequently, a lack of reproducibility compromised the study of the material and additional modifications of the synthetic process were required. Since the formation and growth of $Cu_{2-x}S$ take place during the time that the copper substrate is immersed in the polysulfur solution, the synthesis time was reduced. Thus, the growth of thinner $Cu_{2-x}S$ layers were expected to be controlled. New $Cu_{2-x}S$ electrodes were synthesized for 5 and 1 minute immersion time and subsequently electrochemically evaluated (**Appendix I, Figure A3.3**). The same effect of physical decay of material was observed as for the samples synthesized for 15 minutes. These results suggest that the formation of $Cu_{2-x}S$ on the substrate potentially occurs very rapidly as soon as the metallic Cu substrate and the polysulfur solution come into contact.

At this point, it is crucial to assess the synthetic method to enhance the electrode performance. A more controlled approach to grow the material arose from pouring the solution over the Cu substrate by a drop casting technique instead of dip coating the Cu foil. Much more reproducible electrodes were synthesized, which were efficiently used to reduce hydrogen in *Chapter 4* and to reduce carbon dioxide in *Chapter 5*.

The overall modified synthesis of the copper sulfide electrodes used in this thesis was finally obtained through a rapid and cost-effective process that consists of three steps depicted in **Figure 3.2** and described below.

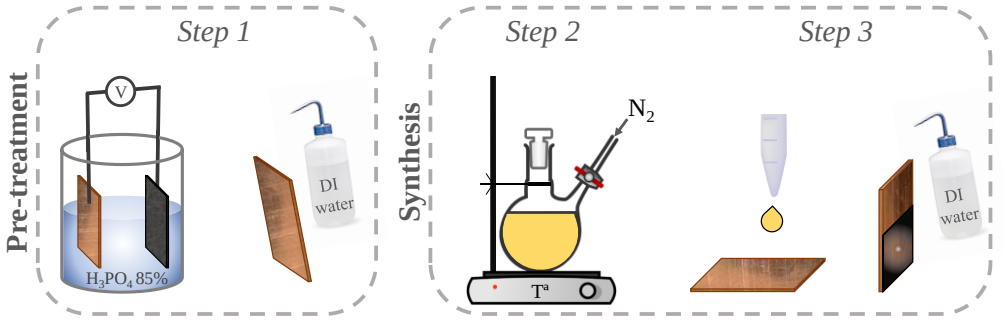

Figure 3.2. Schematic diagram illustrating the synthetic route for preparing copper sulfide electrodes.

Step 1: Substrate pre-treatment. Prior to film preparation, copper foil substrate (Goodfellow, 0.2 mm thick, 99.9%) was cleaned with soap/Milli-Q water, acetone, and ethanol and air dried to subsequently be electrochemically polished. The electropolishing was done in phosphoric acid (Alfa-Aesar, 85%) potentiostatically, for 1 min at 3 V and 10 min at 2 V vs Carbon GDL counterelectrode (FuelCellStore, Sigracet 39 BC) in a two-electrode configuration. Finally, the electropolished copper foil was rinsed with abundant deionized water and dried in air.

Step 2: Sulfide solution preparation. The sodium polysulfide solution was prepared with the modified recipe described previously, by mixing NaOH (Scharlab), $Na_2S \cdot 9H_2O$ (Alfa Aesar, 98%), and S (Sigma-Aldrich, 99.98%) stoichiometrically with deionized (DI) water in a three-neck round bottom flask. The mixture was heated at 313 K with vigorous stirring and constant purified nitrogen bubbling for 3 h and then heated to 373 K.

Step 3: Electrode synthesis. The sodium polysulfide solution in *Step 2* was drop-casted onto the pretreated copper foil substrates. Rapidly, the metal surface turned black as the drop slid across the substrate, leaving a very thin and uniform layer of metallic black appearance. Finally, the electrode was washed with abundant DI water to remove the excess unreacted solution and dried under airflow. The catalyst mass loading was estimated as ~0.400 mg cm^{-2}.

3.3 Compositional and structural characterization

The morphology and structure of the as-synthesized electrodes were investigated by different characterization techniques. Both the electropolished Cu substrate and the copper sulfide electrodes were studied by top-view SEM images at different magnifications in **Figure 3.3a** and **Figure 3.3b** respectively. Whilst the copper substrate has a homogeneous metallic layer after the pre-treatment, the as-synthetized sample features a highly porous structure, characteristic of foamy materials.[18-19] A more in-depth study of the walls of the porous networks shows some nanohexagons, like those observed in the previous synthesis method. This was confirmed by atomic force spectroscopy (AFM), as shown in (**Appendix I, Figure A3.4**. The thickness of the copper sulfide layer was investigated by SEM cross-sectional image and profilometric measurements, which estimated a thickness of 6 µm. This value, in contrast to the 60 µm thin films prepared with the previous synthesis, evidence that a more controlled

growth of the material is obtained when the electrodes are synthetized by the drop-casting modified method.

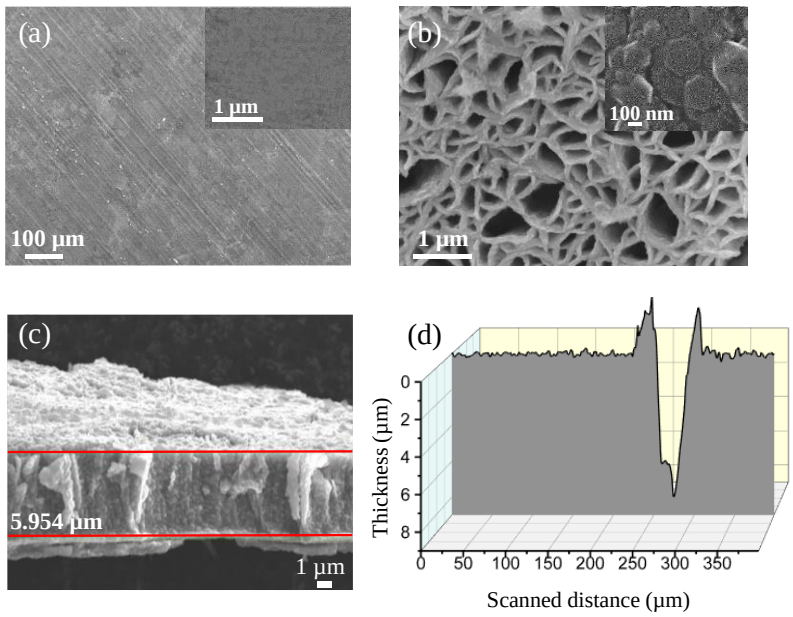

Figure 3.3. Structural and morphological characterization. (a-b) Top view SEM images at different magnitures of the electropolished Cu foil and the copper sulfide electrodes, respectively. (c-d) Thickness characterization of the as-synthetized electrodes. (c) Cross-sectional SEM image and (d) Profilometry of a scratch on the electrode surface. The thickness of the film is in average 6.15 µm. Note that the deeper data is due to a scratch on the copper substrate.

The composition of the as-synthetized electrodes was firstly explored during SEM measurements by microchemical elemental analysis (EDS) revealing the presence of Cu and S in the sample in an approximate stoichiometric Cu:S 2:1 ratio. **Figure 3.4** shows the EDS analysis including the SEM image of the explored area, EDS spectrum and the table containing the elemental quantification.

(a)

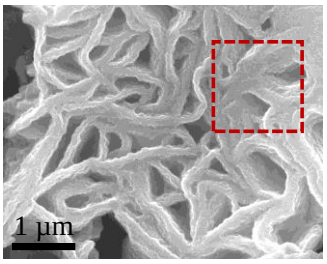

(b)

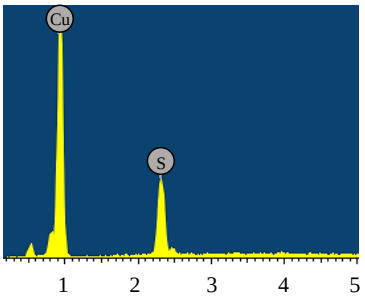

(c)

Element	Weight [%]	Atomic [%]
S (K line)	20.72	34.12
Cu (L line)	79.28	65.88
Totals	100.00	100.00

Figure 3.4. EDS analysis of the as-synthetized electrodes. (a) SEM image of the as-synthesized porous films. (b) EDS spectrum of the red area in (a) and (c) EDS quantification of the spectrum from (b).

Further characterization was performed through high-resolution transmission electron microscopy (HRTEM) in collaboration with the Catalan Institute of Nanoscience and Nanotechnology (ICN2). HRTEM analysis reveals a high-temperature $Cu_{1.8}S$ digenite structure (space group, s.g. 224) containing the family of (211) planes, from a measured interplanar distance of 0.243 nm (**Figure 3.5a**). In addition, the chemical composition of the electrodes was confirmed by electron energy loss spectroscopy (EELS) in scanning transmission electron microscopy (STEM) mode. **Figure 3.5b** sows the extracted STEM-EELS spectrum image composition maps where the S L-edge at 165 eV (green), C K-edge at 284 eV (blue), and Cu L-edge at 931 eV (red) were used. Note that C contribution comes from the composition of the TEM grid and is not present in the electrocatalyst. Furthermore, XRD analysis of the as-synthesized $Cu_{2-x}S$ electrocatalyst showed peaks at 2θ values of 32.3º, 46.7º, and 54.9° that could be indexed to (200), (220), and (311) planes of the $Cu_{1.8}S$ cubic phase, respectively (PDF no. 24-61)[20-21]. Two additional minor peaks are observed at 2θ values of

43.08º and 50.52° assigned to metallic Cu (PDF #04-0836) and indexed to the (111) and (200) crystal planes, respectively. These peaks come from the copper substrate and are much more intense in this diffractogram, compared to the previous synthesis, since the copper sulfide layer obtained in the present synthesis is an order of magnitude thinner. An additional peak appears at the 2θ value of 36.5º, consistent with the formation of superficial Cu_2O, due to the exposure of the samples to air during the synthesis (JCPDS no. 05-0667).[22]

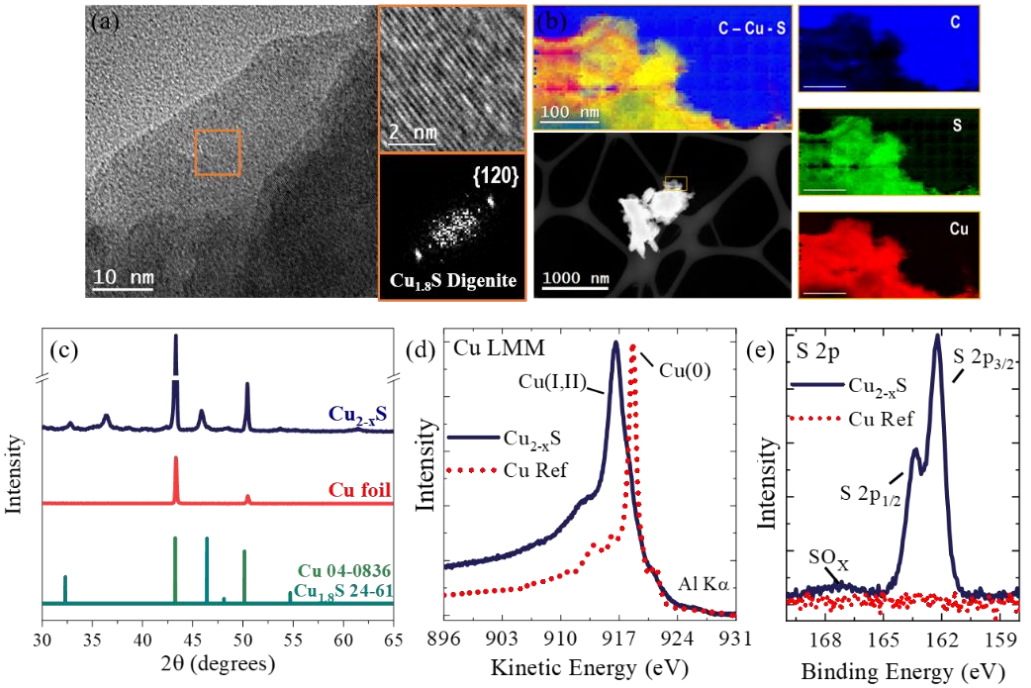

Figure 3.5. Compositional characterization of the as-synthetized $Cu_{2-x}S$. (a) HRTEM image with the indexed power spectrum and a detailed image of the $Cu_{1.8}S$ structure. (b) High-angle annular dark-field (HAADF) STEM general image of the nanostructured $Cu_{1.8}S$ (top left). STEM-EELS analysis (bottom left). EELS compositional maps showing the different elemental distributions: C (blue), S (green), and Cu (red) (right). (c) XRD diffractograms for the electropolished copper foil (red) and the as-synthesized $Cu_{2-x}S$ on the copper substrate (blue) toguether with the XRD reference patterns for $Cu_{1.8}S$ (green petrol) and Cu (green). (d) XPS analysis for Cu LMM and (e) S 2p spectra of the $Cu_{2-x}S$ electrodes. Metallic Cu substrate measured as reference spectra are shown in red dotted lines.

X-ray photoelectron spectroscopy (XPS) was carried out for the chemical analysis of the surface of the $Cu_{2-x}S$ electrode. Since XPS is a technique with a short beam penetration into the material, superficial XPS measurements are usually affected by adsorbed species from air exposure after the synthesis. To enhance the XPS characterization of the sample, the electrodes were sputtered with Ar^+ ions in the analysis chamber in UHV prior to the XPS characterization to remove the oxide layers that form upon exposure of $Cu_{2-x}S$ to air,[23] and the adventitious C that adsorbs exposing the actual material. (**Appendix I, Figure A3.5**) compares of the Cu 2p, Cu LMM, O 1s, C 1s, and S 2p spectra before and after the sputtering showing more intense signals after the treatment.

The representative Cu LMM and S 2p spectra of the $Cu_{2-x}S$ electrodes (blue solid line) shown respectively in **Figure 3.5d** and **Figure 3.5e** include the reference spectra of metallic Cu in red dotted line. The XPS data unveils $Cu_{2-x}S$ stoichiometry of the electrodes.[24] The Cu LMM Auger emission line shape (**Figure 3.5d**) is compatible with the presence of both Cu(I) or Cu(II) chemical states,[25] with the absence of metallic Cu. The Cu 2p spectral region of the as-synthetized electrode exhibits a well-defined 2p2/3 component with a binding energy at 932.7 eV in (**Appendix I, Figure A3.5**). The absence of satellite peaks at ~943.6 eV exclude the presence of Cu(II) species.[25-26] The S 2p spectrum, in **Figure 3.5e**, shows a strong doublet peak correlated with the S 2p3/2 binding energy at 162.2 eV. The observed binding energy is consistent with the presence of S^{2-} species bonded with Cu^+ to form $Cu_{2-x}S$. The presence of a broader and less intense feature at 167 eV may be caused by the presence of residual SO_x species on the electrode surface due to catalyst oxidation at air.

3.4 Conclusions

In this chapter, a simple, fast, environmentally friendly, and cost-effective synthetic route is presented for prepare $Cu_{2-x}S$ films for electrocatalytic applications. The synthetic process was rationally redesigned based on a previously reported process to obtain reproducible electrocatalysts further used to generate hydrogen and to reduce carbon dioxide. The chemical composition, structure and morphology of the as-synthetized electrodes were determined by SEM, EDS, AFM, HRTEM, XRD, XPS and profilomety characterization techniques. All the results are consistent with the formation of 6 µm $Cu_{2-x}S$ thin films with a highly porous microstructure, similar to foamy materials.

3.5 References

1. Liu, X.; Jiao, Y.; Zheng, Y.; Davey, K.; Qiao, S.-Z., A computational study on Pt and Ru dimers supported on graphene for the hydrogen evolution reaction: new insight into the alkaline mechanism. *Journal of Materials Chemistry A* **2019,** *7* (8), 3648-3654.
2. Zhang, J.; Zhao, Y.; Guo, X.; Chen, C.; Dong, C.-L.; Liu, R.-S.; Han, C.-P.; Li, Y.; Gogotsi, Y.; Wang, G., Single platinum atoms immobilized on an MXene as an efficient catalyst for the hydrogen evolution reaction. *Nature Catalysis* **2018,** *1* (12), 985-992.
3. Cao, Q.; Che, R.; Chen, N., Scalable synthesis of Cu2S double-superlattice nanoparticle systems with enhanced UV/visible-light-driven photocatalytic activity. *Applied Catalysis B: Environmental* **2015,** *162*, 187-195.
4. Lepre, E.; Heske, J.; Nowakowski, M.; Scoppola, E.; Zizak, I.; Heil, T.; Kühne, T. D.; Antonietti, M.; Lopez-Salas, N.; Albero, J., Ni-based electrocatalysts for unconventional CO2 reduction reaction to formic acid. *Nano Energy* **2022,** *97*, 107191.
5. Wang, X.; Wang, X.; Zhao, L.; Zhang, H.; Liu, M.; Zhang, C.; Liu, S., Self-reconstruction of cationic activated Ni-MOFs enhanced the intrinsic activity of electrocatalytic water oxidation. *Inorganic Chemistry Frontiers* **2022,** *9* (1), 179-185.
6. Gultom, N. S.; Silitonga, M. Z.; Kuo, D.-H., Bimetallic Cobalt–Nickel Electrode Made by a Sputtering Technique for Electrocatalytic Hydrogen Evolution Reaction: Effect of Nickel Ratios. *ACS Applied Energy Materials* **2022,** *5* (7), 8658-8668.
7. Li, X.; Wang, S.; Wang, G.; Shen, P.; Ma, D.; Chu, K., Mo 2 C for electrocatalytic nitrate reduction to ammonia. *Dalton Transactions* **2022,** *51* (46), 17547-17552.
8. Wang, Y.; Wang, L.; Fu, H., Research progress of Fe-NC catalysts for the electrocatalytic oxygen reduction reaction. *Science China Materials* **2022,** *65* (7), 1701-1722.
9. Fdez-Sanromán, A.; Pazos, M.; Sanromán, M. A.; Rosales, E., Heterogeneous electro-Fenton system using Fe-MOF as catalyst and electrocatalyst for degradation of pharmaceuticals. *Chemosphere* **2023,** *340*, 139942.
10. Ampelli, C.; Giusi, D.; Miceli, M.; Merdzhanova, T.; Smirnov, V.; Chime, U.; Astakhov, O.; Fernandez, A. M.; Veenstra, F.; Garcés-Pineda, F., An artificial leaf device built with earth-abundant materials for combined H2 production and storage as formate with efficiency> 10%. *Energy & Environmental Science* **2023**.

11. Raaijman, S. J.; Arulmozhi, N.; Koper, M. T. M., Morphological stability of copper surfaces under reducing conditions. *ACS Applied Materials & Interfaces* **2021,** *13* (41), 48730-48744.
12. Giménez, S.; Mora-Seró, I.; Macor, L.; Guijarro, N.; Lana-Villarreal, T.; Gómez, R.; Diguna, L. J.; Shen, Q.; Toyoda, T.; Bisquert, J., Improving the performance of colloidal quantum-dot-sensitized solar cells. *Nanotechnology* **2009,** *20* (29), 295204.
13. Hodes, G.; Manassen, J.; Cahen, D., Electrocatalytic electrodes for the polysulfide redox system. *Journal of the Electrochemical Society* **1980,** *127* (3), 544.
14. Zhao, P.; Zhang, H.; Zhou, H.; Yi, B., Nickel foam and carbon felt applications for sodium polysulfide/bromine redox flow battery electrodes. *Electrochimica Acta* **2005,** *51* (6), 1091-1098.
15. Kuhl, K. P.; Cave, E. R.; Abram, D. N.; Jaramillo, T. F., New insights into the electrochemical reduction of carbon dioxide on metallic copper surfaces. *Energy & Environmental Science* **2012,** *5* (5), 7050-7059.
16. Bhat, K. S.; Nagaraja, H. S., Hydrogen evolution reaction at extreme pH conditions of copper sulfide micro-hexagons. *Journal of Science: Advanced Materials and Devices* **2020,** *5* (3), 361-367.
17. Sun, S.; Li, P.; Liang, S.; Yang, Z., Diversified copper sulfide (Cu 2− x S) micro-/nanostructures: A comprehensive review on synthesis, modifications and applications. *Nanoscale* **2017,** *9* (32), 11357-11404.
18. Kim, J.-H.; Kim, R.-H.; Kwon, H.-S., Preparation of copper foam with 3-dimensionally interconnected spherical pore network by electrodeposition. *Electrochemistry Communications* **2008,** *10* (8), 1148-1151.
19. Qazi, U. Y.; Javaid, R.; Tahir, N.; Jamil, A.; Afzal, A., Design of advanced self-supported electrode by surface modification of copper foam with transition metals for efficient hydrogen evolution reaction. *International Journal of Hydrogen Energy* **2020,** *45* (58), 33396-33406.
20. Chen, Y.; Qin, Z.; Wang, X.; Guo, X.; Guo, L., Noble-metal-free Cu 2 S-modified photocatalysts for enhanced photocatalytic hydrogen production by forming nanoscale p–n junction structure. *RSC Advances* **2015,** *5* (23), 18159-18166.
21. An, L.; Zhou, P.; Yin, J.; Liu, H.; Chen, F.; Liu, H.; Du, Y.; Xi, P., Phase transformation fabrication of a Cu2S nanoplate as an efficient catalyst for water oxidation with glycine. *Inorganic chemistry* **2015,** *54* (7), 3281-3289.
22. Kooti, M.; Matouri, L., Fabrication of nanosized cuprous oxide using fehling's solution. *Scientia Iranica* **2010,** *17* (1).
23. Krylova, V.; Andrulevičius, M., Optical, XPS and XRD studies of semiconducting copper sulfide layers on a polyamide film. *International Journal of Photoenergy* **2009,** *2009*.

24. Velásquez, P.; Leinen, D.; Pascual, J.; Ramos-Barrado, J. R.; Cordova, R.; Gómez, H.; Schrebler, R., XPS, SEM, EDX and EIS study of an electrochemically modified electrode surface of natural chalcocite (Cu2S). *Journal of Electroanalytical Chemistry* **2001,** *510* (1-2), 20-28.
25. Biesinger, M. C., Advanced analysis of copper X-ray photoelectron spectra. *Surface and Interface Analysis* **2017,** *49* (13), 1325-1334.
26. Biesinger, M. C.; Lau, L. W. M.; Gerson, A. R.; Smart, R. S. C., Resolving surface chemical states in XPS analysis of first row transition metals, oxides and hydroxides: Sc, Ti, V, Cu and Zn. *Applied surface science* **2010,** *257* (3), 887-898.

APPENDIX I

Electrochemical evaluation of the $Cu_{2-x}S$ electrodes synthetized by dip coating

The $Cu_{2-x}S$ cathodes were further characterized electrochemically. Initially, the electrodes were evaluated for the electrochemical CO_2 reduction reaction. Cyclic voltammetries and chronoamperometric measurements at -0.8 V vs RHE with the subsequent product analysis were carried out to test the activity and selectivity of the material (shown in **Figure A3.1**). Competitive current densities were obtained and formate was qualitatively identified by H^1 NMR as the main CO_2 reduction product after 1 h of reaction, (**Figure A3.2**). However, some troubles with the electrode during the measurements limited the experimentation. Specifically, under reaction conditions, the black $Cu_{2-x}S$ on the Cu substrate grew significantly, leading to material losses due to mechanical detachment, and consequently a lack of reproducibility compromised the study of the material.

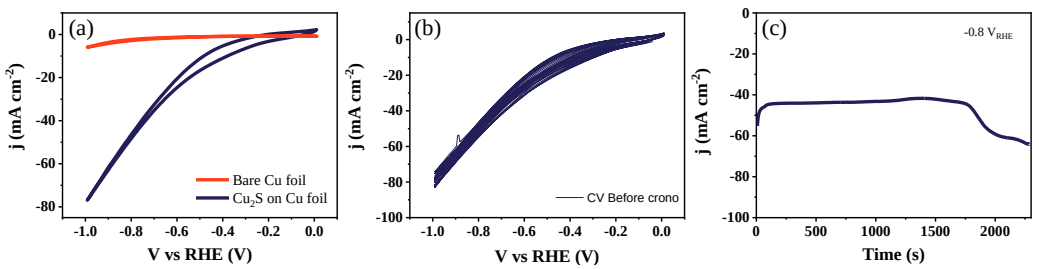

Figure A3.1. Electrochemical characterization of the $Cu_{2-x}S$ cathode for CO_2RR. (a) Comparison between LSV of the bare Cu foil and LSV of the $Cu_{2-x}S$. (b) Cyclic voltammogram for 20 cycles until stabilization of the currents and (c) chronoamperometry at fixed potential of -0.8 V vs RHE. Note that the chronoamperometry ends before 1 hour of reaction, because the excessively transformed material limits the reaction time. All the measurements were performed in 0.1 M $KHCO_3$ saturated with CO_2.

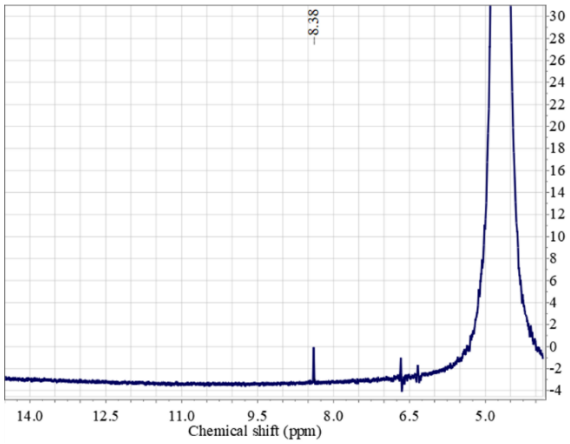

Figure A3.2. H^1 RMN spectrum after the CO_2 reduction reaction with $Cu_{2-x}S$ in **Figure A3.1c** showing the signal of formate.

To address the above-mentioned problems related to film delamination and the lack of reproducibility between samples, the synthetic procedure was modified. Since $Cu_{2-x}S$ grows on Cu when it is immersed in the polysulfide solution, the synthesis time was reduced from 15 min to 5 min and 1 min. Samples very similar to those obtained for 15 min synthesis were obtained, suggesting that a rapid growth of $Cu_{2-x}S$ on the Cu metallic substrate takes place as soon as the substrate and the solution are keep into contact. The electrochemical evaluation of the new electrodes for CO_2 reduction (**Figure A3.3)** exhibits high current densities and selectivity toward formate production, however, the transformation of the material took place during the electrochemical experimentation, directly impacting on the manipulation and reproducibility of the experiments, forcing the reaction to stop before 1 hour.

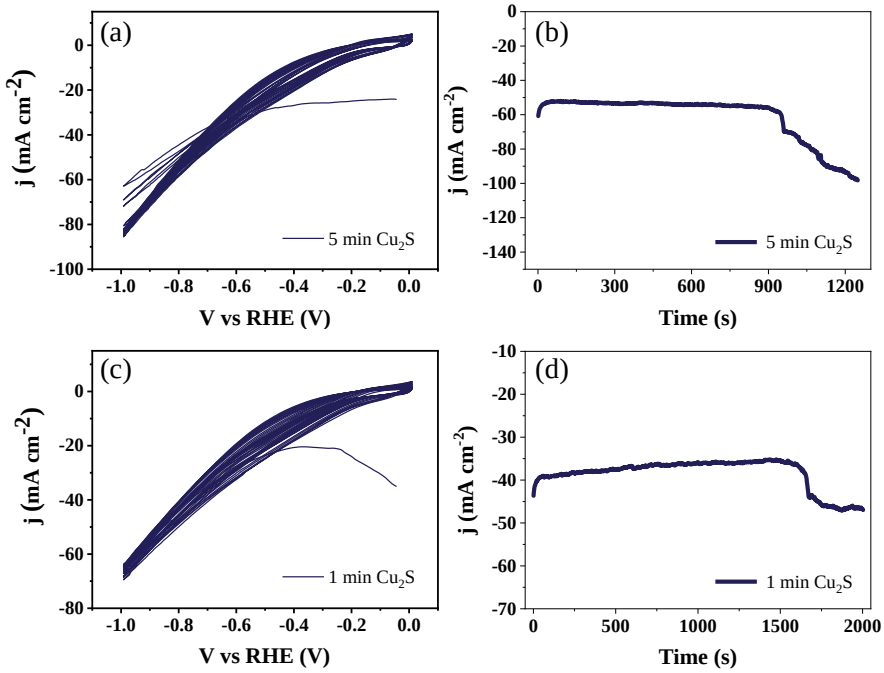

Figure A3.3. Electrochemical evaluation of $Cu_{2-x}S$ electrodes synthetized for 5 min and 1 min for $C0_2RR$ in CO_2 sat. 0.1 M $KHCO_3$. (a-b) Cyclic voltammetries and chronoamperometric measurement at -0.8 V vs RHE performed with $Cu_{2-x}S$ prepared during 5 min and (c-d) Cyclic voltammetries and chronoamperometric measurement at -0.8 V vs RHE performed with $Cu_{2-x}S$ prepared during 1 min.

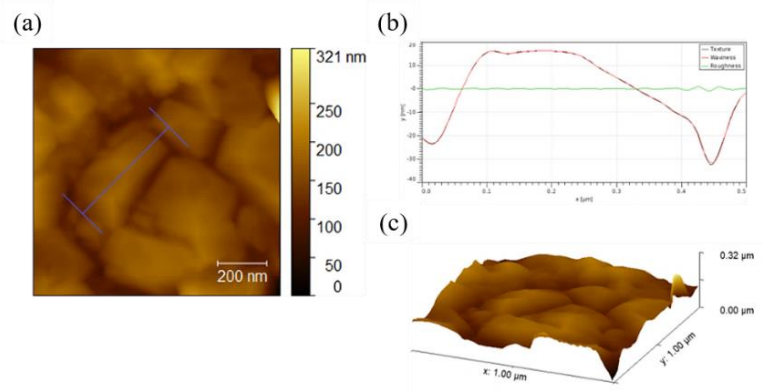

Figure A3.4. AFM analysis of the as-synthetized electrodes. (a) Top view topography. (b) Roughness analysis on a nano-hexagon structure selected in (a) and (c) 3D projection from the top view topography.

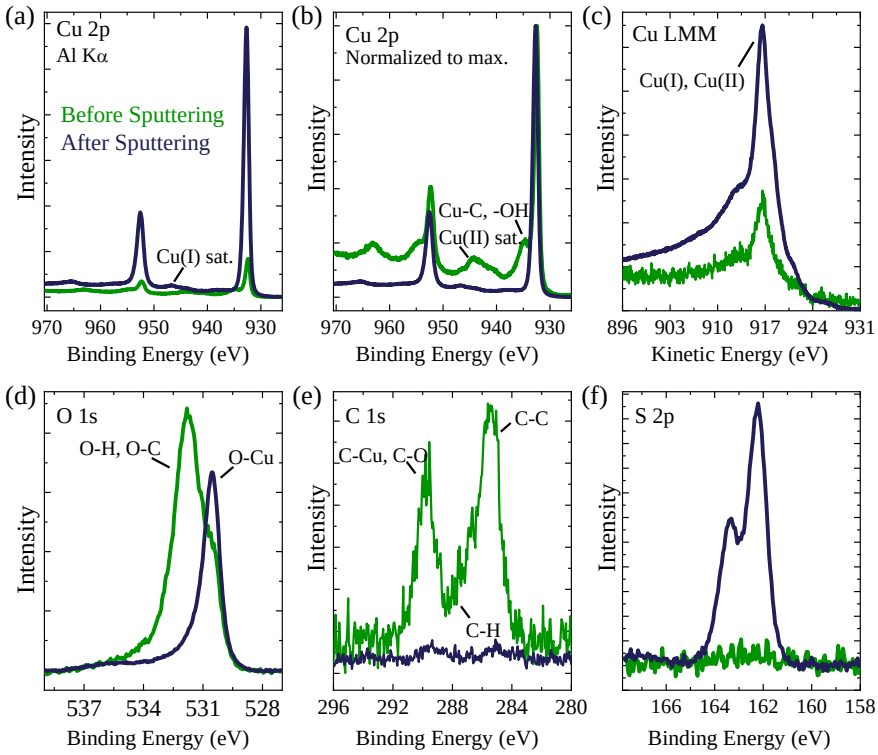

Figure A3.5. XPS analysis of the as-synthetized $Cu_{2-x}S$ electrodes before (green) and after (dark blue) Ar^+ cleaning. (a) Cu 2p spectra, (b) Normalized Cu 2p spectra, (c) Cu Auger spectra, (d) O 1s spectra, (e) C 1s spectra and (f) S 2p spectra.

Experimental section

- Characterization techniques

Scanning electron microscopy (SEM) measurements were performed with a JSM-7000F JEOL FEG-SEM system (Tokyo, Japan) equipped with an INCA 400 Oxford EDS analyzer (Oxford, U.K.) operating at 15 kV.

High resolution transmission electron microscopy (HRTEM) and scanning transmission electron microscopy (STEM) investigations were performed on a field emission gun FEI Tecnai F20 microscope. High angle annular dark-field (HAADF) STEM was combined with electron energy loss spectroscopy (EELS)

in the Tecnai microscope by using a GATAN QUANTUM energy filter in order to obtain compositional maps.

Profilometer measurements were performed on a mechanical profilometer Veeco model Dektak 6 (see Figure S2d).

X-ray diffractograms were recorded using a Rigaku Miniflex 600, (Rigaku Corporation, Tokyo, Japan) with Cu Kα radiation (λ = 1.5418 Å) (see Figure 2d).

Topographic images of the samples were measured by atomic force microscope (AFM) using an Asylum Research Cypher ES (Oxford Instruments-Asylum Research, Santa Barbara, USA) in tapping mode under ambient conditions with a silicon cantilever AC160TSA-R3 (Olympus, Tokio, Japan) with spring constant k = 25.4 N/m, resonant frequency f = 291 kHz and a tip radius of 7 nm (see Figure S3).

X-ray photoemission spectroscopy measurements (XPS) were carried out holding the sample at room temperature and illuminating it with monochromatized Al Kα light (hυ = 1486.6eV) from a microfocus setup (SPECS Focus 600). The excited photelectrons were collected by a SPECS 150 hemispherical analyzer at emission and incidence angles of 40° and 60°, respectively. The overall experimental resolution was extracted from Fermi edge analysis of a reference gold sample and resulted in 0.4 eV. The characterized electrodes were sputtered in UHV to remove the oxide layers that form upon exposure of $Cu_{2-x}S$ to air, and the adventitious C that adsorbs. In order to average inhomogeneities of the electrodes, different positions of the samples were characterized by XPS. The data presented here is the result of averaging multiple spectra of different positions for each sample.

Chapter 4

$Cu_{2-x}S$ electrocatalyst for hydrogen evolution

In this chapter, the results obtained from the investigation of the electrochemical hydrogen evolution reaction (HER) with the nanoporous $Cu_{2-x}S$ electrodes described in *Chapter 4* are presented and discussed. The electrochemical evaluation of the $Cu_{2-x}S$ electrocatalysts, exhibits hydrogen evolution rates that increase during ~1 month of continuous operation. Throughout operation time, $Cu_{2-x}S$ electrodes reach a state-of-the-art current of 400 mA cm^{-2} at -1 V vs RHE at mild conditions (pH 8.6), with practically 100% Faradaic efficiency for H_2 evolution. The current density increased with the electrochemically active surface area of the electrodes. Consistently, improved electrode performance correlated with decreased Tafel slopes. Moreover, a comprehensive structural and chemical characterization of the electrodes before, during and after the HER was carried out, which was crucial for the proper interpretation of the results. Particularly, the analysis of $Cu_{2-x}S$ electrodes by *operando* spectroelectrochemistry (SEC), X-ray diffraction (XRD), and X-ray photoemission spectroscopy (XPS) simultaneously to the electrochemical tests revealed that the catalytic activity is mainly driven by catalytic centers located at Cu species. These results contribute to increase our fundamental understanding of heterogenous electrocatalyst transformation and consequent structure-activity relationship.

4.1 Introduction

Transforming renewable electricity into green hydrogen (H_2), *via* the water splitting process, has emerged as a promising strategy to respond to the increasing energy demand and to decarbonize transportation, heating and fine chemicals sectors.[1-2] Currently, available water splitting electrolyzers work under extreme pH conditions causing environmental pollution and handling hazards. Particularly, Pt-based cathodes, which remain the state-of-the-art catalyst for the HER, are only operative in acidic media. Furthermore, Pt is a scarce and expensive critical raw material.[3] Consequently, scaling-up the HER towards the Gigawatt-scale requires not only highly efficient and durable electrocatalysts, but also operative electrocatalysts at mild pH conditions, produced from Earth-abundant materials and with low-cost, environmental friendly manufacturing techniques. In this context, alternative materials to replace Pt and Ru electrocatalysts based on non-critical materials are attracting increasing attention to scale-up green H_2 production.[4-13] In particular, Cu oxide and chalcogenide electrocatalysts are interesting due to their remarkably low overpotentials (η) and stability compared to other transition metal catalysts towards HER.[14-16]

In this chapter, a comprehensive study of the cost-effective $Cu_{2-x}S$ electrocatalyst is presented. This material shows high efficiency for the HER, with competent overpotential values and record-breaking durability among Cu_xS and Cu_xS–derived electrocatalysts. Several copper sulfide derived electrocatalysts, previously reported and collected in **Appendix II, Table A1** are compared in terms of performance (overpotential) and durability in **Figure 4.1.**

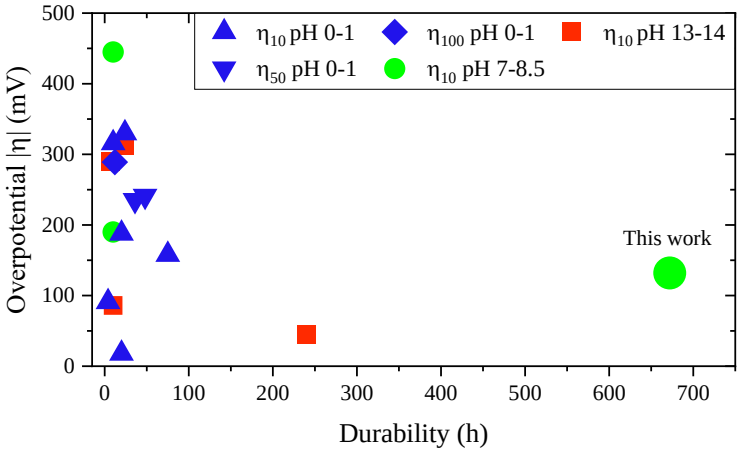

Figure 4.1. Comparative overpotentials at 10 mA cm^{-2} (η_{10}), 50 mA cm^{-2} (η_{50}) and 100 mA cm^{-2} (η_{100}) and durability time benchmark for copper sulfide electrocatalysts in **Appendix I, Table 4.1** and the $Cu_{2-x}S$ electrocatalyst presented in this *Chapter 4* for acidic,[11, 17-20] neutral[21-23] and basic media[18, 24-31].

4.2. Electrocatalytic $Cu_{2-x}S$ evaluation for the HER

The functional evaluation of the $Cu_{2-x}S$ electrocatalyst for the HER evolution was assessed by chronoamperometric (CA) measurements performed at -1 V_{RHE}, simultaneously with the quantification of the evolved H_2 (All experimental details are in **Appendix II, experimental section**). Remarkably, the $Cu_{2-x}S$ electrocatalyst was durable for almost 1 month of continuous operation in a 3-electrode configuration (**Figure 4.3a**). To evaluate the efficiency of the electrocatalyst over time, the evolved H_2 was quantified by gas chromatography (GC) during several days of continuous operation, The resulting Faradaic efficiencies (FE) shown in **Figure 4.2** remain close to 100% for each gas measurement, confirming that the $Cu_{2-x}S$ is highly efficient as hydrogen evolution electrocatalyst. Indeed, it outperforms the best $Cu_{2-x}S$ and $Cu_{2-x}S$-derived electrocatalyst reported to-date (**Figure 4.1** and **Appendix II, Table A4.1** shown the data) [11, 18, 20, 25-29, 32-34]. Specifically, the herein reported $Cu_{2-x}S$ outperforms the best $Cu_{2-x}S$[29] electrocatalyst, measured in 1 M KOH, by 9 times

and the most durable Cu_2S-containing electrocatalyst reported by Bae, *et al.*, with a Cu_2S-Mo_2S electrode[20] measured in 1M H_2SO_4 by almost 3 times. More interestingly, in terms of durability, $Cu_{2-x}S$ outperforms competent noble metal electrodes, such as RuP nanoparticles (~200 h¸ *i.e.*, over a week of operation).[35]

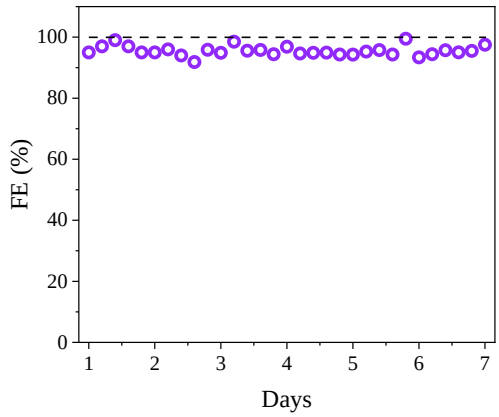

Figure 4.2. Evolution of the Faradaic efficiency of the $Cu_{2-x}S$ electrocatalyst with time, for several days under operation conditions at -1 $V_{RHE.}$

Strikingly, a progressive increase in the recorded current density (J) of the $Cu_{2-x}S$ electrocatalyst was observed during the entire measurement period. The electrocatalyst exhibits initial J values of ~-50 mA cm^{-2} at -1 V_{RHE}, which increase to ~-400 mA cm^{-2} after almost 1 month of continuous operation (**Figure 4.3a**), this is, an 8-fold increase. The increase of J was monitored by systematically interrupting the durability test and performing complementary linear sweep voltammetries (LSVs). **Figure 4.3b** depicts the LSVs measured on different days showing an increasing J, at matched potentials, as a function of time as indicated by the grey arrow. These J values match with the increase observed in the CA (**Figure 4.3a**). Furthermore, the enhanced electrocatalytic performance also correlates with an anodic shift in the overpotential to reach -10 mA cm^{-2}, from ~-530 mV to a benchmark value of ~-130 mV over time (**Figure 4.3b, inset**). Indeed, the herein reported material features among the lowest overpotential values obtained to-date compared to other Cu_xS and Cu_xS-derived

electrocatalysts (**Figure 4.1** and **Appendix II, Table A4.1** for a state-of-the-art comparison).[18, 36] Specifically, compared to a previously reported $Cu_{2-x}S$ cathode for HER in mild pH conditions,[21] the developed $Cu_{2-x}S$ electrocatalyst requires ~60 mV less overpotential. Since faster reaction kinetics are expected at highly acidic or alkaline pH, outstanding η values, as low as ~ 50 mV at 10 mA cm^{-2}, have only been reported when Cu chalcogenides are heterostructured and tested at extreme pH conditions[20]. However, highly acidic or alkaline electrolytes, increase the maintenance costs and the potential risks of environmental pollution when scaling-up H_2 production. In addition, heterostructured Cu-derived electrodes increase the manufacturing costs and increase the complexity of the electrode architectures. Additional blank LSVs measurements were performed in the same conditions with the bare Cu substrate. A comparison of the blank LSVs together with the $Cu_{2-x}S$ electrocatalyst are shown (**Appendix II, Figure A4.1**) revealing negligible HER activity for the bare Cu substrate, which indicates that the HER catalytic activity of the electrode arises from the $Cu_{2-x}S$ material.

This increasing performance of the $Cu_{2-x}S$ electrocatalyst was coincident with a visual increase of the electrode thickness during electrochemistry (**Appendix II, Figure A.4.2**). To investigate a possible correlation between the two phenomena and to rationalize such an increasing performance of our $Cu_{2-x}S$ electrodes, it was proposed that an operando increase of the surface area was taking place. Indeed, larger surface area can facilitate the exposure of more active sites improving the catalytic activity, while minimizing mass transport limitations.[29, 37-38]

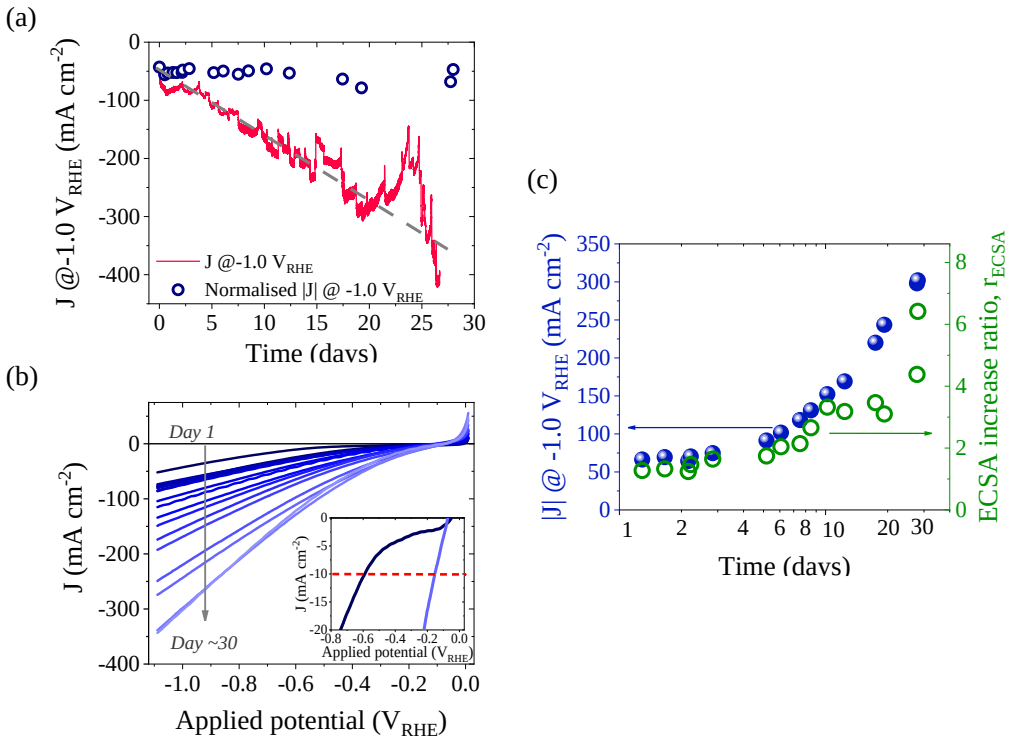

Figure 4.3. Electrochemical response of the $Cu_{2-x}S$ catalyst during 28 days of continuous operation. (a) Chronoamperometric measurement at -1V vs RHE of the $Cu_{2-x}S$ catalyst for 28 days continuous operation. Steady-state currents at -1.0 V vs. RHE normalized by *ECSA* are shown as light blue empty dots. (b) Linear sweep voltammograms (LSV), measured at 20 mV s^{-1}, as a function of operation time between the day #1 to day #28 (from darker to lighter blue). Inset: zoom between the first and the last LSV to compare the overpotential at -10 mA cm^{-2} (dashed red line). (c) Cathodic current densities (|J|) measured at -1.0 V vs. RHE, from Figure 3b (blue filled dots) compared to the electrochemical surface area (*ECSA*) increase ratio (empty green dots, r_{ECSA}) calculated using eq. 1. Note that the time is in log scale.

To explore this plausible correlation, the electrochemical surface area (*ECSA*) of the $Cu_{2-x}S$ electrocatalyst was systematically monitored by electrochemical impedance spectroscopy (EIS) during the whole operation time. Since the *ECSA* is directly related with the double layer capacitance (C_{dl}) according with the Equation (4.1)[39], the C_{dl} extracted from EIS measurements was used to determine the electrochemical surface area increase ratio (r_{ECSA}) by Equation (4.2):

$$r_{ECSA} = \frac{C_{dl}}{C_S} \quad (4.1)$$

$$r_{ECSA} = \frac{ECSA_t}{ECSA_1} = \frac{{}^{(C_{dl})_t}/_{C_S}}{{}^{(C_{dl})_1}/_{C_S}} = \frac{(C_{dl})_t}{(C_{dl})_1} \quad (4.2)$$

where $ECSA_1$ and $ECSA_t$ correspond to the electrochemical surface area (*ECSA*), of day 1 ($ECSA_1$) and that of subsequent measurements as a function of operation time ($ECSA_t$). C_s is the specific capacitance, which is cancelled in Equation (4.2), and similarly to the *ECSA*, $(C_{dl})_1$ and $(C_{dl})_t$ correspond to the double layer capacitance of the 1st day $(C_{dl})_1$ and that of subsequent measurements $(C_{dl})_t$. More specifically, C_{dl} data were obtained from the low-frequency capacitance plateau region (0.5–10 Hz), *i.e.*, Bode plot in **Appendix II, Figure A.4.3**, as previously reported.[38, 40]

Figure 4.3c compares the recorded *J* values at -1 V vs RHE (blue filled dots) from the LSV in **Figure 4.3b** with the calculated electrochemical surface area increase ratio (r_{ECSA}), (green empty dots). It is apparent from **Figure 4.3c** that r_{ECSA} increases by a factor of ~6.5 times from the day 1 to the day 28 of continuous operation. The r_{ECSA} was further used to normalize the *LSVs* from **Figure 4.3b**. Upon normalization, much closer j-V curves were obtained (see **Appendix II, Figure A4.4)**. Additionally, normalized *J* values at -1 vs RHE appears to be almost invariant with time (**Figure 4.3a**, blue empty dots). The observed cathodic increase in *J* can be mostly attributed to a higher density of exposed active sites, as evidenced by the increase in *ECSA* measured by EIS. This surface area increase allows this $Cu_{2-x}S$ catalyst to reach remarkable current densities, while preserving the FE towards H_2 evolution. Interestingly, a similar increased HER performance was reported by Yang and co-workers on CoMnS-based electrodes, where the increased current density was associated with an *ECSA* increase, due to a partial crystallinity loss of the electrocatalyst.[41]

The charge transfer mechanism of the $Cu_{2-x}S$ electrodes for HER was firstly analysed by means of EIS. For this propose, the set of data of day 28, *i.e.*, at the highest current density reported here (~-400 mA cm^{-2}, **Figure 4.3b**) was selected. Series (R_S) and charge transfer (R_{CT}), resistances, fitted to a Randle's circuit (**Appendix II, Figure A4.5 and Figure A4.6**) were analysed. In **Figure 4.4a**, both R_S and R_{CT} are represented together, displaying a crossover-point at ~ -0.3 V *vs.* RHE, where R_{CT} becomes smaller than R_S. This is coincident with the HER catalytic onset potential (in **Figure 4.3b**), indicating that at more cathodic potentials (grey shaded region in **Figure 4.4a**) the delivered current is limited by the device design and engineering (reflected by R_S), rather than by surface electrocatalysis (controlled by R_{CT}). On the other hand, R_S exhibits a constant behaviour with applied bias, but decreasing as a function of the operation time. Additional measurements at different electrolyte concentration were performed to explore possible influences of the ionic concentration of the solution on the R_S value.[42-43] As shown in **Appendix II, Figure A4.7**, the R_S decreases at higher ionic concentration of the electrolyte, potentially attributed to a higher density of mobile charges. This argument supports that the decrease of the R_S values could be motivated by an increase in the ionic concentration of the electrolyte solution after ~1 month continuous measurement in a static electrochemical cell. Specifically, a small local pH variation (basification of 0.5-1 pH units at distance to the cathode < 1 cm) was measured, while the pH of the bulk electrolyte was stable along the measurement. This R_S variation can aid understanding the difference between the 8-fold increase in J, compared to the 6.5-fold increase in *ECSA*. In addition, the extracted capacitances as a function of increasing the negative bias shown in **Figure 4.4a**, exhibit a constant decreasing trend which could be mainly attributed to a decrease in the accumulated species at the catalyst/electrolyte interface during the catalysis, when the charge transfer process is enhanced.[44] Other effects such as the decrease of the electrochemical

surface area due to the evolution of H_2 bubbles, could partially be related with the decreased capacitance values.

Tafel analysis was performed to gain insights into the charge transfer HER kinetics. Steady-state LSVs (**Appendix II, Figure A4.8**) were performed to determine the iR drop corrected Tafel slopes (**Figure 4.4b** and **c**).[45-46] Initially, the electrocatalyst exhibits a Tafel slope of 270 mV dec^{-1}, which gradually decreases during the first ~week plateauing around ~190 mV dec^{-1} until ~one month, indicating that HER kinetics of the $Cu_{2-x}S$ is faster after one month of continuous operation, correlating with the increase in *J* and the decrease in η (**Figure 4.3b** and **inset**, respectively) as well as with the decrease in R_{CT} (**Appendix II, Figure A4.6**). Note that by the time the Tafel slope becomes approximately constant in **Figure 4.4b**, an inflection point in the currents and the *ECSA* ratio occurs and higher *J* values and *ECSA* ratios are observed (**Figure 4.3c**).[47-49] Overall, the evolution of both *ECSA* and Tafel slopes suggests a slight enhancement of the intrinsic activity of our $Cu_{2-x}S$ catalyst over time.

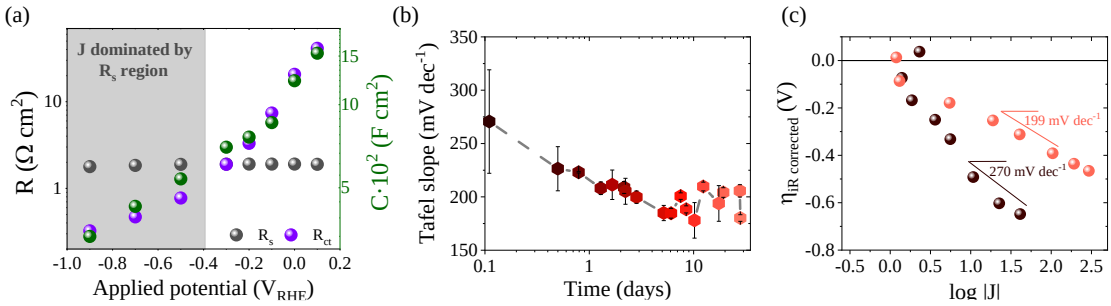

Figure 4.4. HER mechanistic analysis. (a) Series (R_S) and charge transfer (R_{CT}) resistances and capacitance, R_S (grey dots), R_{CT} (magenta dots) and C (green dots) respectively at the 28th day of measurement. (b) Tafel plot, comparing the 1st (dark red data) with the 28th (pink data) day of measurement, of the steady-state catalytic currents and (c) Tafel slope values as a function of operation time obtained from panel b. All measurements were performed in 0.1 M $KHCO_3$ (pH 8.6).

4.3 HER mechanistic analysis

A plausible evolution of the structure and composition of the $Cu_{2-x}S$ electrodes during the HER process was studied by combining a set of complementary *operando* and post-mortem analysis techniques.

4.3.1 *Operando* spectoelectrochemical analysis

Firstly, *operando* spectroelectrochemical (SEC) analysis,[50] was performed on the $Cu_{2-x}S$ electrocatalyst. The UV-Vis-NIR absorption spectra of the $Cu_{2-x}S$ was monitored, while applying to the electrode different potentials. A comparative investigation of the differential spectral fingerprint (in the UV-Vis-NIR range) of the $Cu_{2-x}S$ electrode as a function of applied potential, together with blank spectra of the electrode and the reaction medium are shown in **Figure 4.5**. This information was key for the interpretation of the SEC results (see **Appendix II, Figures A4.9** for the full set of spectra). **Figure 4.5** shows a relatively flat spectra (light green and blue data) for both $Cu_{2-x}S$ and Cu electrodes obtained at low potentials (0.1 V vs RHE), where the current density is close to zero (**Figure 4.3b**). These flat optical fingerprints evolve to spectra with at least two peaks ~1080 and ~1270 nm when applying higher potentials where HER catalytic currents take place.[51-53] With the purpose of assigning the observed peaks, blank measurements were also performed in an inert electrolyte, where hydrogen evolution is not expected. Specifically, when the $Cu_{2-x}S$ electrode is under equivalent applied potentials in acetonitrile (**Figure 4.5** dark red spectrum), these two peaks are not present. This observation suggests that the signals observed at ~1080 and ~1270 nm correspond to protons bound to both $Cu_{2-x}S$ and electropolished Cu surfaces. This optical fingerprint at ~1080 and ~1270 nm in the catalytic region is therefore assigned to accumulated species at the rate determining step of the HER. Note that these signals are only observed while the HER is taking place and are equivalent between both $Cu_{2-x}S$ catalyst and bare Cu

foil substrate (shaded region in **Figure 4.5**). This parallelism between both $Cu_{2-x}S$ and bare Cu electrodes suggests that the HER catalytic activity of $Cu_{2-x}S$ is driven by centers located at Cu species at the $Cu_{2-x}S$ surface.

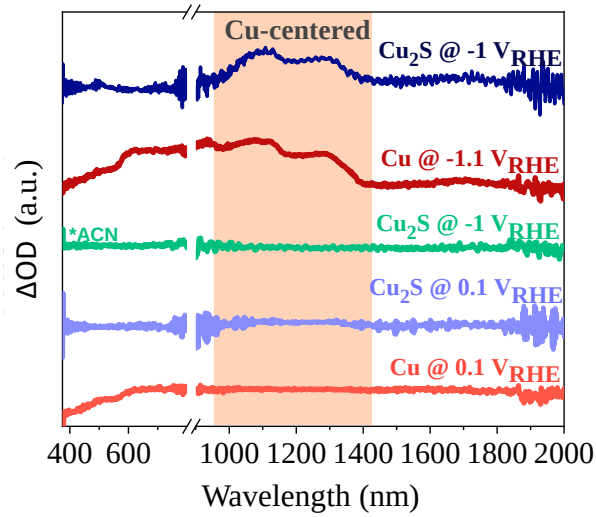

Figure 4.5 *Operando* SEC analysis of the $Cu_{2-x}S$ electrocatalyst for the HER. Differential optical density spectra of the $Cu_{2-x}S$ (light and dark blue) and reference Cu foil (light and dark red) electrodes as a function of potential. For reference, $Cu_{2-x}S$ differential spectra were measured also in 0.1 M TBAP in acetonitrile (green).

To further assign each optical signal observed in the spectra, additional experiments were performed by adding 10% volume of water to the inert electrolyte. **Figure 4.6** shows UV-Vis-NIR absorption spectra of $Cu_{2-x}S$ electrocatalyst measured in 0.1 M $KHCO_3$ (dark blue), 0.1 M TBAP in acetonitrile and water (orange) and 0.1 M TBAP in acetonitrile (dark red) under a strong negative bias. Optical signals ~550 and 1370 nm appear in all spectra, even when no reaction is taking place (dark red spectrum, inert electrrolyte). Both signals are assigned to optical absorptions from the $Cu_{2-x}S$ electrode, consistently with previous reports.[51, 54] Additionally, a NIR absorption band from free H_2O (*i.e.*, water molecules in the solvent not interacting with the catalyst surface) is also observed at ~1500 nm.[55]

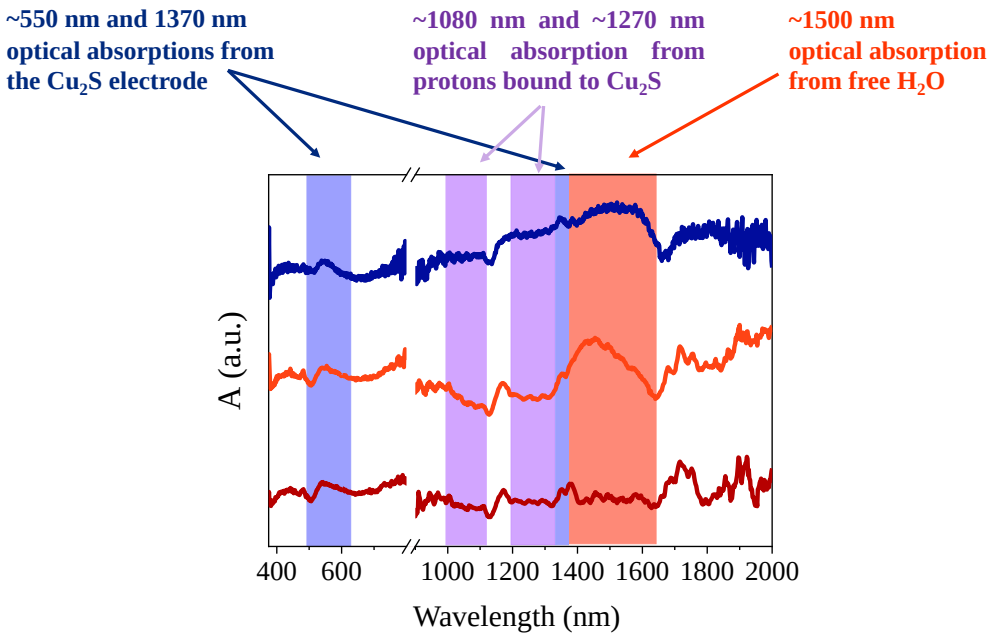

Figure 4.6. UV-Vis-NIR absorption spectra of $Cu_{2-x}S$ electrode in 0.1 M $KHCO_3$ (dark blue) while applying -1 V vs RHE and 0.1 M TBAP in acetonitrile and water (orange) and 0.1 M TBAP in acetonitrile (dark red) while applying -1 V vs NHE.

4.3.2 *Operando* XRD characterization

Operando XRD analysis was carried out on the $Cu_{2-x}S$ electrocatalyst to unveil crystallinity changes taking place under catalytic conditions. **Figure 4.7** shows the evolution of the collected XRD patterns when the potential is progressively increased from open circuit potential (OCP) to -1 V vs RHE. At OCP conditions, characteristic phases of Cu, $Cu_{1.8}S$ and superficial Cu_2O and $CuSO_4$ are observed.

The Cu_2O phase disappeared at -0.4 V vs RHE, matching with the redox peak in the cathodic linear sweep voltammogram (inset in **Figure 4.7)**. At more cathodic potentials (-0.8 and -1 V *vs* RHE), the $Cu_{1.8}S$ and the secondary $CuSO_4$ phase signals also vanished. Notably, the signal corresponding to the $Cu_{1.8}S$ phase disappears at the same potential at which another cathodic wave is featured in the linear sweep voltammogram. Accordingly, it is assigned to the reduction

of the $Cu_{1.8}S$ at -0.8 V *vs* RHE (inset in **Figure 4.7**). The reductions of the Cu_2O, $Cu_{1.8}S$ and $CuSO_4$ are consistent with the growth of the Cu signal around -1.0V *vs* RHE. A more precise quantification of the evolution of the Cu peak was elusive, since the Cu foil underneath results in oscillations in intensity.

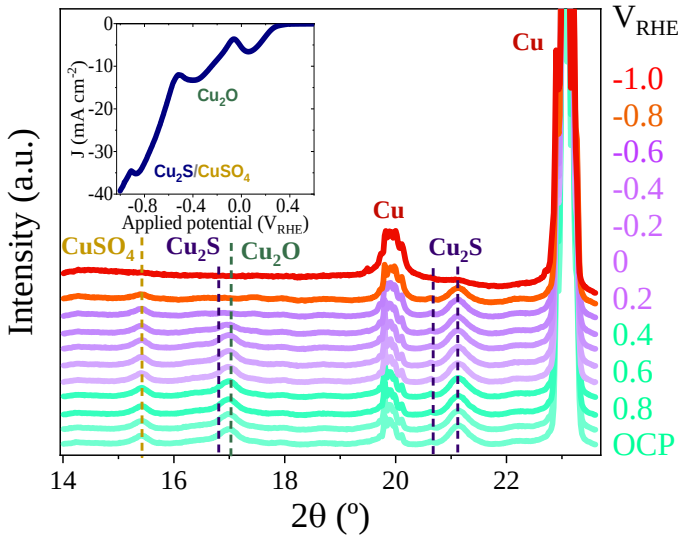

Figure 4.7. *Operando* XRD diffractograms of the $Cu_{2-x}S$ electrocatalyst at different potentials from OCP to -1.0 V vs RHE. Inset: LSV with the assigned redox peaks.

4.3.3 *Quasi-in situ* XPS characterization

Complementary, XPS measurements were performed to probe the chemical state and composition of the surface of the $Cu_{2-x}S$ electrodes immediately after HER. The electrochemical experiments and emersion of the sample were carried out in a glovebox under N_2 (99.999%) inert atmosphere. Then, the sample transfer was conducted using a portable glovebox under N_2, which was adapted to be directly attached to the ultra-high vacuum (UHV, $P<10^{-9}$ mbar) system to avoid air contamination and oxidative effects on the measured sample. Indeed, copper sulfide compounds are known to readily oxidize upon air-exposure.[56-57] A comparison of post-mortem characterization exposing the samples in air vs N_2 in **Appendix II, Figure A4.10** suggests that post-mortem characterization in air

could mislead the interpretation of the actual composition of the surface. Another procedure was added to the measurement protocol to obtain better and more reliable measurements. By an abundant rinsing of the electrode after HER, residues of the bulk electrolyte solution on the sample surface, which might inhibit the photo-emitted signal from the surface of the electrode are removed. **Appendix II, Figure A4.11** shows the XPS spectra comparison of washed versus unwashed samples.

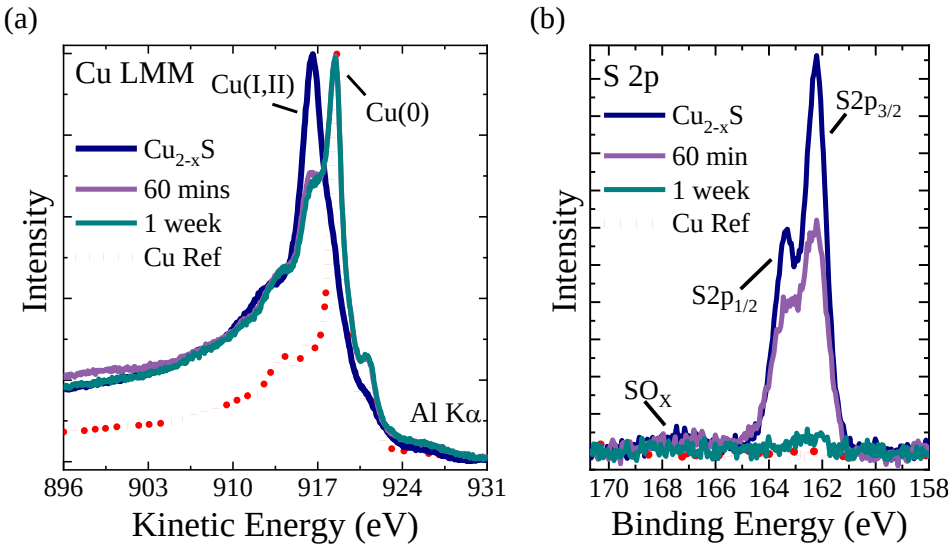

Figure 4.8. *Quasi-in situ* reference and post electrochemical XPS characterization. (a) Cu LMM and (b) S 2p spectra.

Post-electrochemical XPS characterization of the $Cu_{2-x}S$ electrodes obtained after the cleaning protocol and transfer in N_2 atmosphere are shown in **Figure 4.8. Figure 4.8a** and **b** show, respectively, the Cu LMM Auger transition and S 2p core level emission of the electrodes after 60 min (purple solid line) and 1 week (blue petroleum solid line) of operation. The spectra from the as-synthesized electrode (blue lines) and metallic Cu substrate (red dotted lines) were measured and included as reference. As for the XPS characterization of the as-synthetized electrodes in *Chapter 3* after the electrochemistry the surface of

the electrodes was also gently sputtered with Ar^+ ions prior to the XPS characterization. This procedure allows obtaining more accurate signals and eliminating remaining residues from the transfer procedure. The XPS spectra in **Figure 4.8a** evidence that the electrodes have evolved to a reduced metallic state after 60 min and 1 week operation, attributed to the increase of the Cu^0 (K.E. 918.4 eV) component in the Cu LMM spectra, simultaneous to the decrease of the Cu (I, II) (K.E. 917 eV) components observed in the as-synthesized electrodes. Notably, a decrease of the S2p component takes place with operation time (**Figure 4.8b**), observing almost complete depletion of S after 1 week of catalytic activity, in agreement with previously discussed *operando* XRD experiments. Such depletion of S could be associated with an initial formation of S vacancies, which evolve to the dissolution of S to the electrolyte as shown in **Appendix II, Figure A4.12**. The S 2p XPS spectrum of the fresh $Cu_{2-x}S$ electrode (blue line, **Figure 4.8b**) shows two peaks located at 162.2 eV (S $2p_{3/2}$) and 163.37 eV (S $2p_{1/2}$), corresponding to the spin-orbit splitting (ΔE = 1.17 eV) of the 2p orbital. Both components contain equivalent chemical information. The S 2p spectrum of the electrode after 60 min of operation (purple line, **Figure 4.8b**) presents a substantial (about 1/3) reduction of its initial intensity. The deconvoluted analysis of the spectral features reveals the emergence of an additional component at higher binding energies ($E(2p_{3/2})$ = 162.7 eV), which adds up to approximately 38% of the total S signal (**Appendix II, Figure A4.13**). This higher-energy component could be tentatively attributed as the fingerprint of a transient phase at the beginning of the electrocatalytic process, which precludes the total depletion of S from the electrode.

In general, we observe that the increased HER performance correlates with an operando *ECSA* increase of the reported $Cu_{2-x}S$ catalyst. As the HER proceeds, severe changes in crystallinity and a progressive S leaching are detected, leading

to a highly porous and active catalytic micro/nanostructure as shown schematically in **Figure 4.9**. The increase in porosity is consistent with an increase in the *ECSA* resulting in a higher density of exposed active sites that are found to be centered at Cu species.

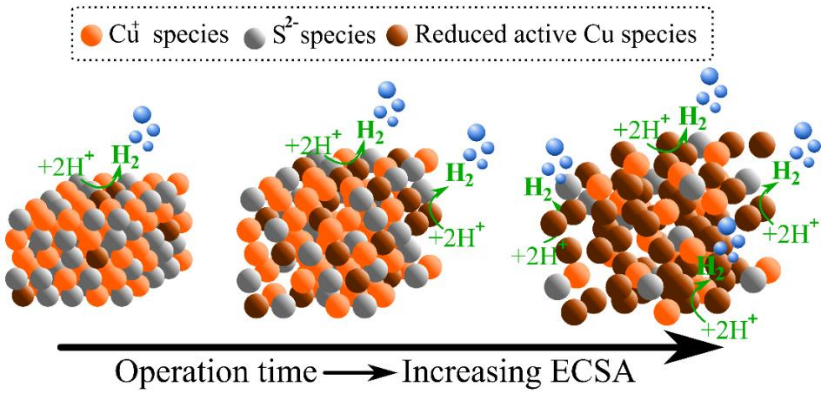

Figure 4.9. Schematic representation of the proposed changes in crystallinity of the $Cu_{1.8}S$ electrocatalyst, concomitant to the S (grey) leaching process that leads to more catalytically active Cu species (brown) to be exposed leading to faster HER.

4.4 Conclusions

In this chapter, a complete investigation of the HER with an Earth-abundant $Cu_{2-x}S$ electrocatalyst has been reported. The study has concluded that this $Cu_{2-x}S$ electrode is highly efficient for H_2 production with FE ~100% and current densities that increase from 50 mA cm^{-2} to ~400 mA cm^{-2}, with remarkably low overpotentials (130 mV at 10 mA·cm^{-2}) in a mild pH electrolyte, for almost one month of continuous operation. All these features make the developed $Cu_{2-x}S$ electrocatalyst a very competitive candidate for the scalability of the HER. Additionally, a comprehensive electrochemical, structural, and chemical analysis on the mechanistic pathway of the reaction and the electrode evolution under *operando* conditions has been presented. The combination of all these characterization techniques unveils a direct relationship between the increase in the current densities and the *ECSA* and establishes a faster HER kinetics with

increasing operation time. SEC analysis reported for the first time for copper-based films for HER, in situ XRD analysis and air-free XPS characterization of the post-mortem electrode demonstrate that the catalytically active sites are located on Cu species. In conclusion, it is demonstrated that Earth abundant, environmental friendly and cost-effective $Cu_{2-x}S$ materials, operating in almost neutral pH conditions are highly efficient, durable, and economically competitive electrocatalysts for the hydrogen evolution.

4.5 References

1. Midilli, A.; Ay, M.; Dincer, I.; Rosen, M. A., On hydrogen and hydrogen energy strategies: I: current status and needs. *Renewable and sustainable energy reviews* **2005,** *9* (3), 255-271.
2. Lewis, N. S.; Nocera, D. G., Powering the planet: Chemical challenges in solar energy utilization. *Proceedings of the National Academy of Sciences* **2006,** *103* (43), 15729-15735.
3. Ayers, K.; Danilovic, N.; Ouimet, R.; Carmo, M.; Pivovar, B.; Bornstein, M., Perspectives on low-temperature electrolysis and potential for renewable hydrogen at scale. *Annual review of chemical and biomolecular engineering* **2019,** *10*, 219-239.
4. Vesborg, P. C. K.; Seger, B.; Chorkendorff, I. B., Recent development in hydrogen evolution reaction catalysts and their practical implementation. *The journal of physical chemistry letters* **2015,** *6* (6), 951-957.
5. Yu, P.; Wang, F.; Shifa, T. A.; Zhan, X.; Lou, X.; Xia, F.; He, J., Earth abundant materials beyond transition metal dichalcogenides: a focus on electrocatalyzing hydrogen evolution reaction. *Nano Energy* **2019,** *58*, 244-276.
6. Popczun, E. J.; McKone, J. R.; Read, C. G.; Biacchi, A. J.; Wiltrout, A. M.; Lewis, N. S.; Schaak, R. E., Nanostructured nickel phosphide as an electrocatalyst for the hydrogen evolution reaction. *Journal of the American Chemical Society* **2013,** *135* (25), 9267-9270.
7. Anantharaj, S.; Kundu, S.; Noda, S., Progress in nickel chalcogenide electrocatalyzed hydrogen evolution reaction. *Journal of Materials Chemistry A* **2020,** *8* (8), 4174-4192.
8. Kuznetsov, D. A.; Chen, Z.; Kumar, P. V.; Tsoukalou, A.; Kierzkowska, A.; Abdala, P. M.; Safonova, O. V.; Fedorov, A.; Müller, C. R., Single site cobalt substitution in 2D molybdenum carbide (MXene) enhances catalytic activity in the hydrogen evolution reaction. *Journal of the American Chemical Society* **2019,** *141* (44), 17809-17816.
9. Nadar, A.; Banerjee, A. M.; Pai, M. R.; Antony, R. P.; Patra, A. K.; Sastry, P. U.; Donthula, H.; Tewari, R.; Tripathi, A. K., Effect of Mo content on hydrogen evolution reaction activity of Mo2C/C electrocatalysts. *International Journal of Hydrogen Energy* **2020,** *45* (23), 12691-12701.
10. Piontek, S.; Andronescu, C.; Zaichenko, A.; Konkena, B.; Junge Puring, K.; Marler, B.; Antoni, H.; Sinev, I.; Muhler, M.; Mollenhauer, D., Influence of the Fe: Ni Ratio and Reaction Temperature on the Efficiency of (Fe x Ni1–x) 9S8 Electrocatalysts Applied in the Hydrogen Evolution Reaction. *ACS Catalysis* **2018,** *8* (2), 987-996.

11. Wei, Y.; He, W.; Sun, P.; Yin, J.; Deng, X.; Xu, X., Synthesis of hollow Cu/Cu2O/Cu2S nanotubes for enhanced electrocatalytic hydrogen evolution. *Applied Surface Science* **2019,** *476*, 966-971.
12. Shen, Y.; Zhou, Y.; Wang, D.; Wu, X.; Li, J.; Xi, J., Nickel–copper alloy encapsulated in graphitic carbon shells as electrocatalysts for hydrogen evolution reaction. *Advanced Energy Materials* **2018,** *8* (2), 1701759.
13. Zignani, S. C.; Faro, M. L.; Carbone, A.; Italiano, C.; Trocino, S.; Monforte, G.; Aricò, A. S., Performance and stability of a critical raw materials-free anion exchange membrane electrolysis cell. *Electrochimica Acta* **2022,** *413*, 140078.
14. Anichini, C.; Czepa, W.; Aliprandi, A.; Consolaro, V. G.; Ersen, O.; Ciesielski, A.; Samorì, P., Synthesis and characterization of ultralong copper sulfide nanowires and their electrical properties. *Journal of Materials Chemistry C* **2021,** *9* (36), 12133-12140.
15. Shinagawa, T.; Larrazábal, G. O.; Martín, A. J.; Krumeich, F.; Perez-Ramirez, J., Sulfur-modified copper catalysts for the electrochemical reduction of carbon dioxide to formate. *ACS Catalysis* **2018,** *8* (2), 837-844.
16. Ampelli, C.; Giusi, D.; Miceli, M.; Merdzhanova, T.; Smirnov, V.; Chime, U.; Astakhov, O.; Fernandez, A. M.; Veenstra, F.; Garcés-Pineda, F., An artificial leaf device built with earth-abundant materials for combined H2 production and storage as formate with efficiency> 10%. *Energy & Environmental Science* **2023**.
17. Durairaj, A.; Sakthivel, T.; Ramanathan, S.; Obadiah, A.; Vasanthkumar, S., Hierarchical Cu2Se nanostructures film for peroxymonosulfate activation and electrocatalytic hydrogen evolution. *Journal of the Taiwan Institute of Chemical Engineers* **2019,** *99*, 66-73.
18. Bhat, K. S.; Nagaraja, H. S., Hydrogen evolution reaction at extreme pH conditions of copper sulfide micro-hexagons. *Journal of Science: Advanced Materials and Devices* **2020,** *5* (3), 361-367.
19. Zhang, L.; Guo, Y.; Iqbal, A.; Li, B.; Gong, D.; Liu, W.; Iqbal, K.; Liu, W.; Qin, W., One-step synthesis of the 3D flower-like heterostructure MoS2/CuS nanohybrid for electrocatalytic hydrogen evolution. *International Journal of Hydrogen Energy* **2018,** *43* (3), 1251-1260.
20. Bae, C.; Ho, T. A.; Kim, H.; Lee, S.; Lim, S.; Kim, M.; Yoo, H.; Montero-Moreno, J. M.; Park, J. H.; Shin, H., Bulk layered heterojunction as an efficient electrocatalyst for hydrogen evolution. *Science advances* **2017,** *3* (3), e1602215.
21. Fan, M.; Gao, R.; Zou, Y.-C.; Wang, D.; Bai, N.; Li, G.-D.; Zou, X., An efficient nanostructured copper (I) sulfide-based hydrogen evolution electrocatalyst at neutral pH. *Electrochimica Acta* **2016,** *215*, 366-373.
22. Li, M.; Qian, Y.; Du, J.; Wu, H.; Zhang, L.; Li, G.; Li, K.; Wang, W.; Kang, D. J., CuS nanosheets decorated with CoS2 nanoparticles as an efficient

electrocatalyst for enhanced hydrogen evolution at all pH values. *ACS Sustainable Chemistry & Engineering* **2019,** *7* (16), 14016-14022.
23. Marimuthu, T.; Yuvakkumar, R.; Ravi, G.; Zheng, Y.; Bi, Z.; Xu, X.; Xu, G.; Velauthapillai, D., One-step fabrication of copper sulfide catalysts for HER in natural seawater and their bifunctional properties in freshwater splitting. *Fuel* **2022,** *322*, 124073.
24. Ma, B.; Yang, Z.; Yuan, Z.; Chen, Y., Effective surface roughening of three-dimensional copper foam via sulfurization treatment as a bifunctional electrocatalyst for water splitting. *International Journal of Hydrogen Energy* **2019,** *44* (3), 1620-1626.
25. Yang, D.; Cao, L.; Huang, J.; Liu, Q.; Li, G.; He, D.; Wang, J.; Feng, L., Vanadium-doped hierarchical Cu2S nanowall arrays assembled by nanowires on copper foam as an efficient electrocatalyst for hydrogen evolution reaction. *Scripta Materialia* **2021,** *196*, 113756.
26. Zhou, Q.; Li, T.-T.; Wang, J.; Guo, F.; Zheng, Y.-Q., Hierarchical Cu2S NRs@ CoS core-shell structure and its derivative towards synergistic electrocatalytic water splitting. *Electrochimica Acta* **2019,** *296*, 1035-1041.
27. Wang, X.; Wang, J.; Zhang, X.; Tian, Q.; Liu, M.; Cai, N.; Xue, Y.; Chen, W.; Li, W.; Yu, F., Nitrogen-Doped Cu2S/MoS2 Heterojunction Nanorod Arrays on Copper Foam for Efficient Hydrogen Evolution Reaction. *ChemCatChem* **2019,** *11* (4), 1354-1361.
28. Wang, D.; Li, J.; Zhao, Y.; Xu, H.; Zhao, J., Bifunctional Cu2S–Co (OH) 2 nanotube array/Cu foam electrocatalyst for overall water splitting. *Electrochimica Acta* **2019,** *316*, 8-18.
29. Xu, F.; Lu, J.; Luo, L.; Yu, C.; Tang, Z.; Abbo, H. S.; Titinchi, S. J. J.; Zhu, J.; Kang Shen, P.; Yin, S., Cu2S-Cu3P nanowire arrays self-supported on copper foam as boosting electrocatalysts for hydrogen evolution. *Energy Technology* **2019,** *7* (4), 1800993.
30. Xie, Y.; Huang, J.; Xu, R.; He, D.; Niu, M.; Li, X.; Xu, G.; Cao, L.; Feng, L., Mo-doped Cu2S multilayer nanosheets grown in situ on copper foam for efficient hydrogen evolution reaction. *Molecules* **2022,** *27* (18), 5961.
31. Marimuthu, T.; Yuvakkumar, R.; Kumar, P. S.; Ravi, G.; Xu, X.; Velauthapillai, D.; Dai Viet, N. V., Cost effective and facile low temperature hydrothermal fabrication of Cu2S thin films for hydrogen evolution reaction in seawater splitting. *International Journal of Hydrogen Energy* **2022,** *47* (72), 30819-30829.
32. Zuo, Y.; Liu, Y.; Li, J.; Du, R.; Han, X.; Zhang, T.; Arbiol, J.; Divins, N. r. J.; Llorca, J.; Guijarro, N. s., In situ electrochemical oxidation of Cu2S into CuO nanowires as a durable and efficient electrocatalyst for oxygen evolution reaction. *Chemistry of materials* **2019,** *31* (18), 7732-7743.

33. Wang, Y.; Ge, Z.; Li, X.; Zhao, J.; Ma, B.; Chen, Y., Cu2S nanorod arrays with coarse surfaces to enhance the electrochemically active surface area for water oxidation. *Journal of colloid and interface science* **2020,** *567*, 308-315.
34. He, L.; Zhou, D.; Lin, Y.; Ge, R.; Hou, X.; Sun, X.; Zheng, C., Ultrarapid in situ synthesis of Cu2S nanosheet arrays on copper foam with room-temperature-active iodine plasma for efficient and cost-effective oxygen evolution. *ACS Catalysis* **2018,** *8* (5), 3859-3864.
35. Yu, J.; Guo, Y.; She, S.; Miao, S.; Ni, M.; Zhou, W.; Liu, M.; Shao, Z., Bigger is surprisingly better: agglomerates of larger RuP nanoparticles outperform benchmark Pt nanocatalysts for the hydrogen evolution reaction. *Advanced Materials* **2018,** *30* (39), 1800047.
36. Roger, I.; Shipman, M. A.; Symes, M. D., Earth-abundant catalysts for electrochemical and photoelectrochemical water splitting. *Nature Reviews Chemistry* **2017,** *1* (1), 1-13.
37. Lu, J.; Yin, S.; Shen, P. K., Carbon-encapsulated electrocatalysts for the hydrogen evolution reaction. *Electrochemical Energy Reviews* **2019,** *2* (1), 105-127.
38. Zhao, G.; Rui, K.; Dou, S. X.; Sun, W., Heterostructures for electrochemical hydrogen evolution reaction: a review. *Advanced Functional Materials* **2018,** *28* (43), 1803291.
39. McCrory, C. C. L.; Jung, S.; Peters, J. C.; Jaramillo, T. F., Benchmarking heterogeneous electrocatalysts for the oxygen evolution reaction. *Journal of the American Chemical Society* **2013,** *135* (45), 16977-16987.
40. Safshekan, S.; Herraiz-Cardona, I.; Cardenas-Morcoso, D.; Ojani, R.; Haro, M.; Gimenez, S., Solar Energy Storage by a Heterostructured BiVO4–PbO x Photocapacitive Device. *ACS Energy Letters* **2017,** *2* (2), 469-475.
41. Li, Q.; Xing, Z.; Wang, D.; Sun, X.; Yang, X., In situ electrochemically activated CoMn-S@ NiO/CC nanosheets array for enhanced hydrogen evolution. *ACS Catalysis* **2016,** *6* (5), 2797-2801.
42. Verma, S.; Lu, X.; Ma, S.; Masel, R. I.; Kenis, P. J. A., The effect of electrolyte composition on the electroreduction of CO 2 to CO on Ag based gas diffusion electrodes. *Physical Chemistry Chemical Physics* **2016,** *18* (10), 7075-7084.
43. Marcandalli, G.; Goyal, A.; Koper, M. T. M., Electrolyte Effects on the Faradaic Efficiency of CO2 Reduction to CO on a Gold Electrode. *ACS catalysis* **2021,** *11* (9), 4936-4945.
44. López, N.; Garcés-Pineda, F. A.; Nguyën, H. C.; Blasco-Ahicart, M.; García-Tecedor, M.; de Fez Febré, M.; Tang, P.-Y.; Arbiol, J.; Giménez, S.; Galan-Mascaros, J. R., Push-pull electronic effects in surface active sites enhance electrocatalytic oxygen evolution on transition metal oxides. *ChemSusChem* **2021**.

45. Anantharaj, S.; Noda, S.; Driess, M.; Menezes, P. W., The Pitfalls of Using Potentiodynamic Polarization Curves for Tafel Analysis in Electrocatalytic Water Splitting. *ACS Energy Letters* **2021,** *6* (4), 1607-1611.
46. Murthy, A. P.; Theerthagiri, J.; Madhavan, J., Insights on Tafel constant in the analysis of hydrogen evolution reaction. *The Journal of Physical Chemistry C* **2018,** *122* (42), 23943-23949.
47. Zhou, L.; Han, Z.; Li, W.; Leng, W.; Yu, Z.; Zhao, Z., Hierarchical Co–Mo–S nanoflowers as efficient electrocatalyst for hydrogen evolution reaction in neutral media. *Journal of Alloys and Compounds* **2020,** *844*, 156108.
48. Liu, C.; Zhang, G.; Yu, L.; Qu, J.; Liu, H., Oxygen doping to optimize atomic hydrogen binding energy on NiCoP for highly efficient hydrogen evolution. *Small* **2018,** *14* (22), 1800421.
49. Gupta, S.; Patel, N.; Miotello, A.; Kothari, D. C., Cobalt-boride: An efficient and robust electrocatalyst for hydrogen evolution reaction. *Journal of Power Sources* **2015,** *279*, 620-625.
50. Mesa, C. A.; Pastor, E.; Francàs, L., UV-Vis operando spectroelectrochemistry for (photo) electrocatalysis: principles and guidelines. *Current Opinion in Electrochemistry* **2022**, 101098.
51. Xie, Y.; Riedinger, A.; Prato, M.; Casu, A.; Genovese, A.; Guardia, P.; Sottini, S.; Sangregorio, C.; Miszta, K.; Ghosh, S., Copper sulfide nanocrystals with tunable composition by reduction of covellite nanocrystals with Cu+ ions. *Journal of the American Chemical Society* **2013,** *135* (46), 17630-17637.
52. Salzemann, C.; Lisiecki, I.; Brioude, A.; Urban, J.; Pileni, M. P., Collections of copper nanocrystals characterized by different sizes and shapes: optical response of these nanoobjects. *The Journal of Physical Chemistry B* **2004,** *108* (35), 13242-13248.
53. Wieder, H.; Czanderna, A. W., Optical properties of copper oxide films. *Journal of Applied Physics* **1966,** *37* (1), 184-187.
54. Van Der Stam, W.; Gudjonsdottir, S.; Evers, W. H.; Houtepen, A. J., Switching between plasmonic and fluorescent copper sulfide nanocrystals. *Journal of the American Chemical Society* **2017,** *139* (37), 13208-13217.
55. Wave, G., An Introduction to Online NIR Water Measurements in Liquid Samples. *AZo Materials* **2019**.
56. Krylova, V.; Andrulevičius, M., Optical, XPS and XRD studies of semiconducting copper sulfide layers on a polyamide film. *International Journal of Photoenergy* **2009,** *2009*.
57. Kundu, A.; Adak, M. K.; Kumar, Y.; Chakraborty, B., Electrochemically derived crystalline CuO from covellite CuS nanoplates: a multifunctional anode material. *Inorganic Chemistry* **2022,** *61* (12), 4995-5009.

APPENDIX II

Table S1. Comparison of the HER performance of the Cu_2S electrocatalyst presented in this work with other Cu_2S and Cu-based materials reported in the literature.

Materials	Solution	Overpotentials(ŋ)	Stability	Tafel slope	Ref.
Cu_2S	0.1 M $KHCO_3$	132 mV @10 mA cm^{-2}	30 days	199 mV dec^{-1}	This work
γ-Cu_2S	1 M PBS	190 mV @10 mA cm^{-2}	10 h	98.8 mV dec^{-1}	21
CuS	0.5 M PBS	550 mV @10 mA cm^{-2}	-	149 mV dec^{-1}	22
Cu_2S@Cu	1 M KOH	316 mV @10 mA cm^{-2}	10 h	76 mV dec^{-1}	24
V-Cu_2S- NW	1 M KOH	188 mV @10 mA cm^{-2}	20 h	82.6 mV dec^{-1}	25
Cu_2S	1 M KOH	330 mV @10 mA cm^{-2}	24 h	106.93 mV dec^{-1}	18
Cu_2Se	0.5 M H_2SO_4	320 mV @10 mA cm^{-2}	-	79 mV dec^{-1}	17
Cu_2S NRs	1 M KOH	352 mV @ 50 mA cm^{-2}	-	141 mV dec^{-1}	26
Cu_2S NRs@CoS	1 M KOH	235 mV @ 50 mA cm^{-2}	36 h	121 mV dec^{-1}	26
Cu_2S-$Co(OH)_2$ NT	1 M KOH	241 mV @ 50 mA cm^{-2}	48 h	92 mV dec^{-1}	28
Cu_2S/MoS_2/CF	1 M KOH	91 mV @ 10 mA cm^{-2}	4 h	41 mV dec^{-1}	27
Cu_2S- Cu_3P	1 M KOH	158 mV @10 mA cm^{-2}	75 h	45 mV dec^{-1}	29
Cu/Cu_2O/Cu_2S NT	0.5 M H_2SO_4	86 @10 mA cm-2	10 h	107 mV dec^{-1}	11
Cu_2S	0.5 M H_2SO_4	312 mV @ 10 mA cm^{-2}	24 h	49.79 mV dec^{-1}	18
MoS_2/CuS	0.5 M H_2SO_4	290 mV @ 10 mA cm^{-2}	6.6 h	63 mV dec^{-1}	19
Cu_2S/CF	1 M KOH	277 mV @ 10 mA cm^{-2}		420 mV dec^{-1}	30
Mo-Cu_2S/CF		18 mV @ 10 mA cm^{-2}	20 h	171 mV dec^{-1}	
Cu_2S	Seawater	445 mV @ 10 mA cm^{-2}	10 h	136.1 mV dec^{-1}	23
Cu_2S	1 M KOH seawater	289 mV @ 100 mA cm^{-2}	12 h	128 mV dec^{-1}	31
$Cu_xS/MoS_2/TiO_2$	0.1 M H_2SO_4	~45 mV @ 10 mA cm^{-2}	10 days	~39 mV dec^{-1}	20

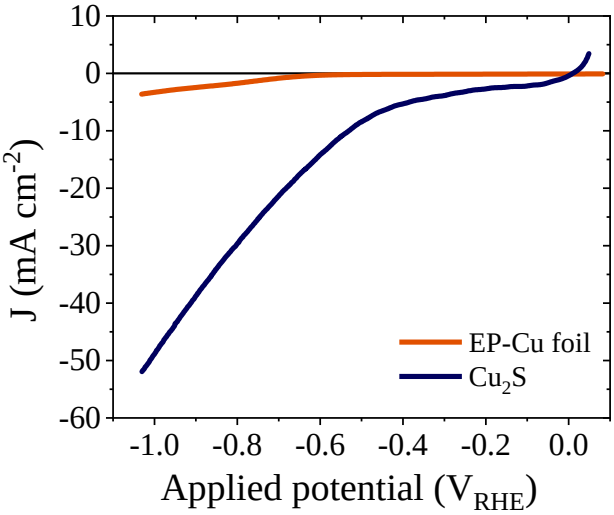

Figure A4.1 Linear sweep voltammetries comparison between the electropolished copper substrate (EP-Cu foil) and the copper sulfide electrocatalyst.

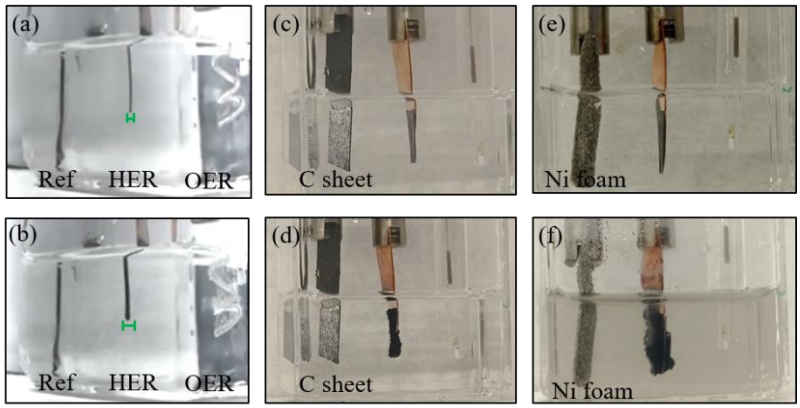

Figure A4.2. Comparative pictures of the $Cu_{2-x}S$ electrodes before (above) and after (bottom) applying potential. (a) Before and (b) after 1 h of chronoamperometric measurement vs Pt wire showing the visual increase of the surface of the electrode. Additional measurements vs C sheet (c-d) and Ni foam (e-f) were performed to verify that the electrode behaved the same.

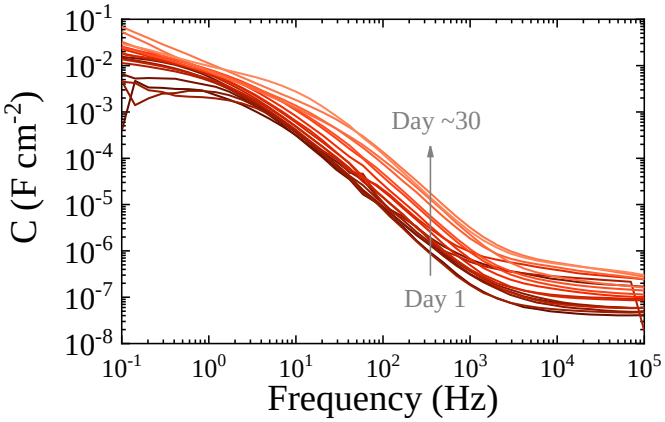

Figure A4.3. Real part of the complex capacitance measured as a function of frequency (Bode plots) of our $Cu_{2-x}S$ electrodes a function of operation time measured at -0.1 V *vs* RHE (non-faradaic region). The C_{dl} values were taken at ~5 Hz.

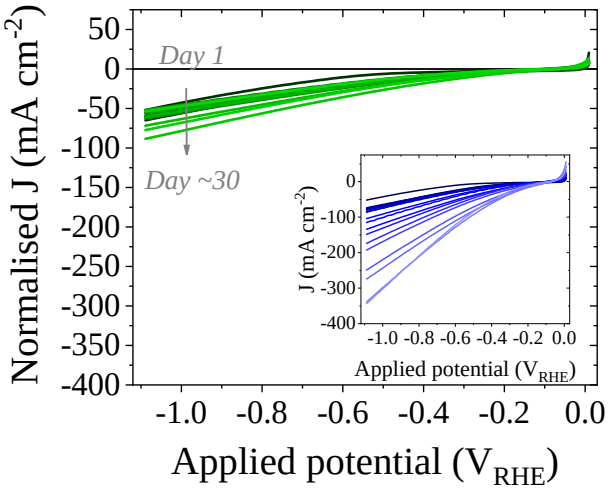

Figure A4.4. Normalized linear sweep voltammograms (LSV) by the r_{ECSA} values from **Figure 4.3c** of the $Cu_{2-x}S$ electrode as a function of operation time. The LSV were measured at 20 mV s-1 in 0.1 M KHCO3.

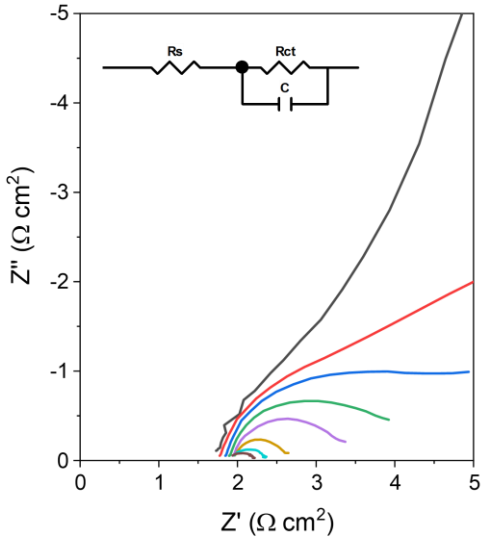

Figure A4.5. Nyquist plots. Real versus imaginary part of the complex impedance for $Cu_{2-x}S$ electrocatalyst at different applied voltages and the employed Randles' equivalent circuit for EIS analysis.

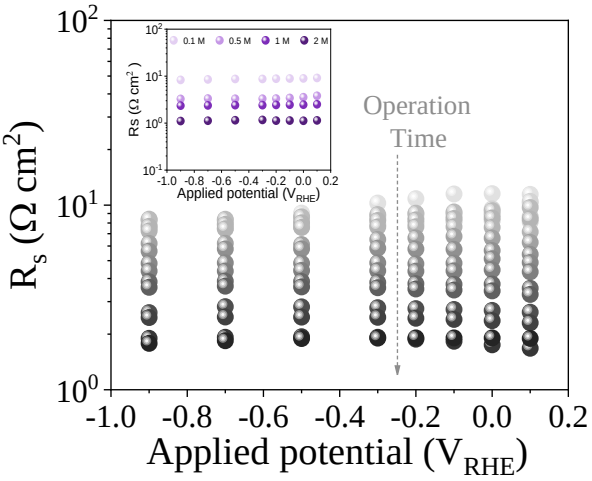

Figure A4.6. R_s values of the $Cu_{2-x}S$ catalysts extracted from electrochemical impedance spectroscopy (EIS) analysis as a function of operation time (indicated by the grey arrow), inset: R_s values of the Cu_2S catalysts measured as a function of concentration of $KHCO_3$ electrolyte. A 20-fold increase of the $KHCO_3$ concentration results in a decrease of ~1 order of magnitude in the R_s, thus, the observed ohmic drop decrease can be attributed to an increase in ionic concentration in the electrolyte.

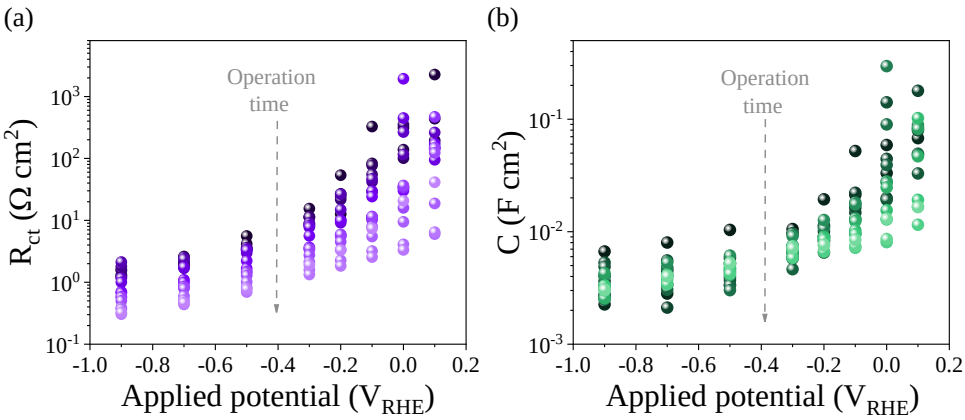

Figure A4.7. Different extracted parameters from EIS measurements: a) Charge transfer resistances (R_{ct}) b) Capacitances values as a function of operation time from the $Cu_{2-x}S$ electrocatalysts.

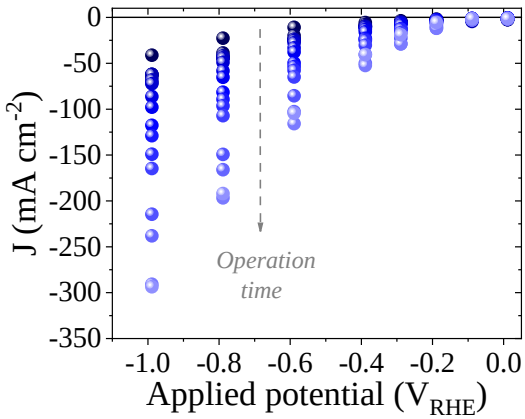

Figure A4.8. Steady-state LSVs of the $Cu_{2-x}S$ electrode as a function of operation time. Every data point corresponds to the average current of the last 60 s of a 5-minute chronoamperometric measurement at every measured potential.

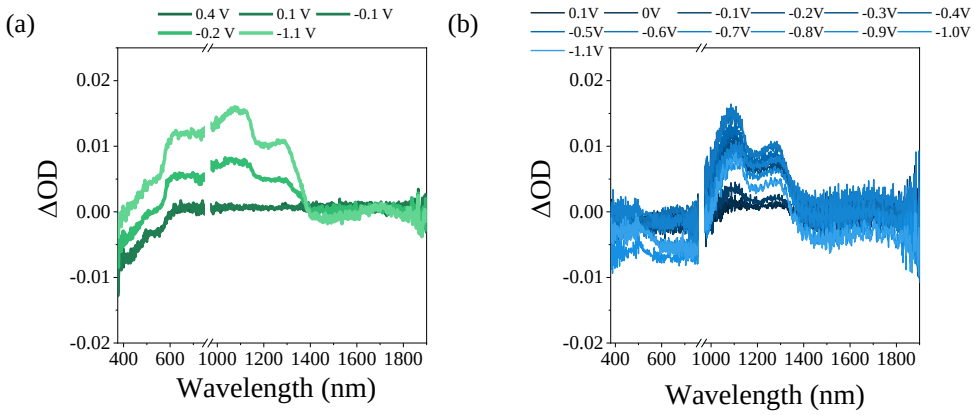

Figure A4.9. Differential spectra of the (a) reference Cu foil and (b) $Cu_{2-x}S$ and reference electrodes as a function of applied potential.

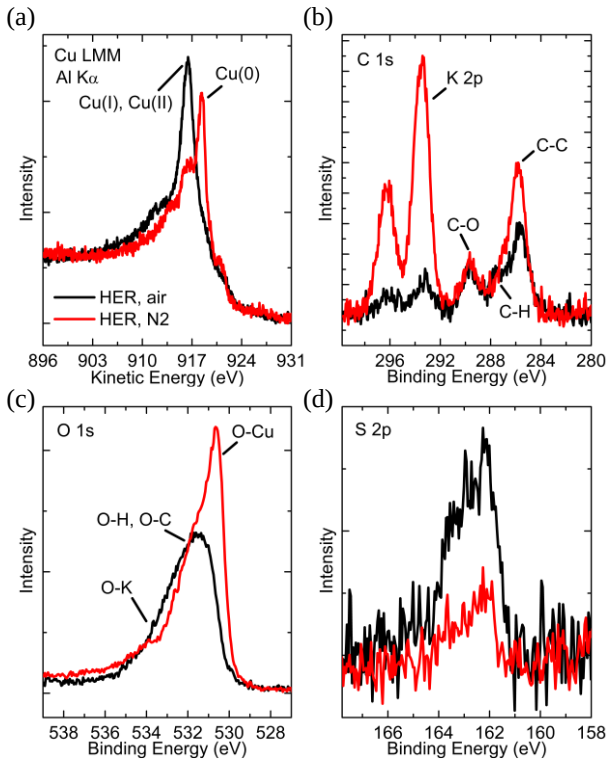

Figure A4.10. XPS analysis of the $Cu_{2-x}S$ electrodes after the electrochemical measurements (a) Cu Auger spectra, (b) C 1s spectra, (c) O 1s spectra and (d) 2p spectra when transferred under air (black) and under N_2 atmospheres (red).

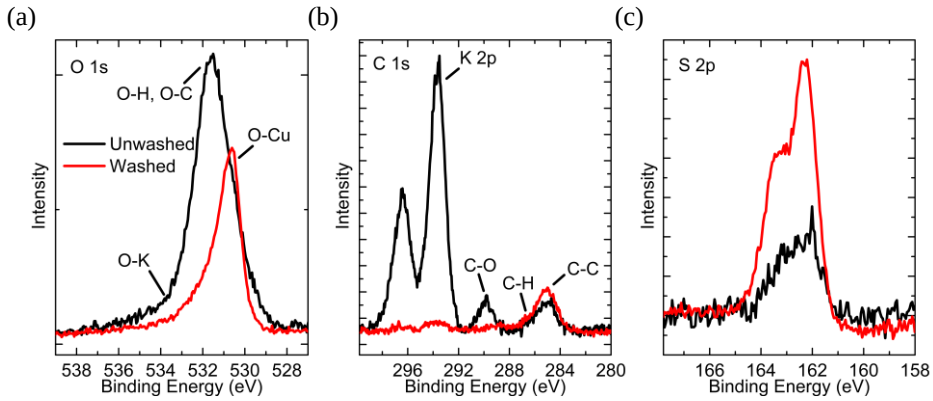

Figure A4.11 XPS analysis of the $Cu_{2-x}S$ electrodes after the electrochemical measurements with and without washing with water.

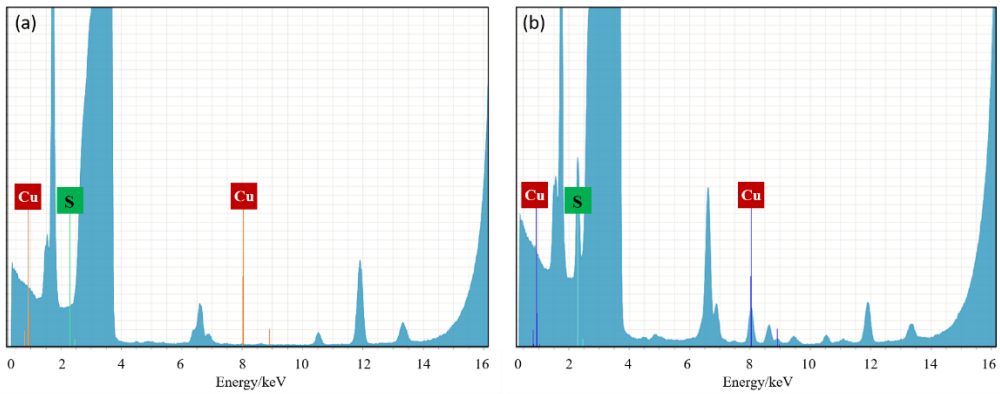

Figure A4.12. Total reflection X-rays fluorescence (TXRF) analysis of the electrolyte (a) before and (b) after the electrochemical test.

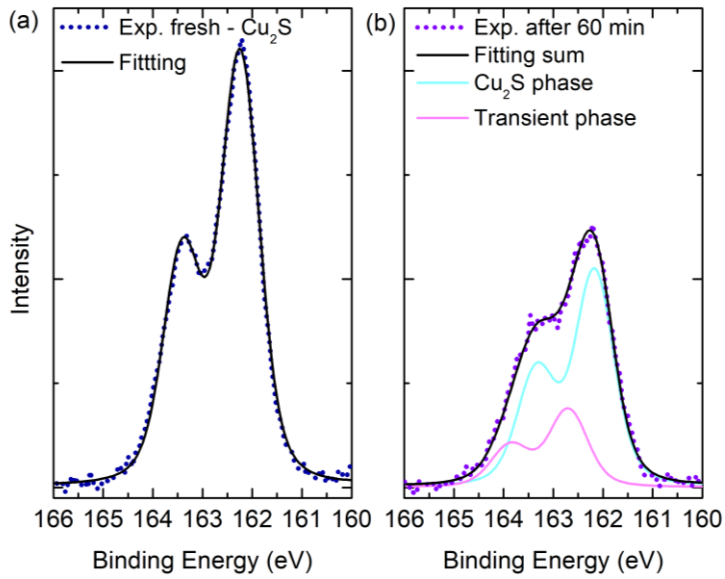

Figure A4.13. Deconvoluted analysis of the spectral features in the S 2p spectrum of the (a) fresh $Cu_{2-x}S$ electrode, and (b) after 60 min of operation. The S 2p region of the fresh $Cu_{2-x}S$ represents a single doublet function at 162.2 eV with a spin-orbit splitting of 1.17 eV and a 0.53 intensity ratio. The S 2p spectrum of the electrode after 60 min of electrochemical treatment reveals an important reduction of its initial intensity and present a second chemical component at higher binding energies, with the described doublet at 162.7 eV. This component adds up to approximately 38% of the total S signal.

Experimental section

- Electrochemical measurements

The electrochemical performance of the electrodes was evaluated by linear sweep voltammetry (LSV) and chronoamperometry (CA) using an Autolab potentiostat/galvanostat PGSTAT302 in a three-electrode homemade sealed electrochemical cell suitable for gas chromatography. Aqueous Ag/AgCl (0.3M KCl, ALS, Japan) and a Pt wire (Alfa Aesar) were used as reference and counter electrode, respectively and a 1 cm^2 geometrical area $Cu_{2-x}S$ film as working electrode. Potassium bicarbonate ($KHCO_3$) was chosen as electrolyte due to its moderate pH, electrode performance (compared to KPi electrolyte) and the

potential implementation of our electrocatalysts in sea water reduction. All the potentials reported herein refer to the reversible hydrogen electrode (RHE) and were calculated through the Nernst equation: VRHE = VAg/AgCl + 0.199 + 0.059·pH. Data has not been iR corrected unless otherwise stated. LSV were performed between 0.1 and -1 V vs RHE with a scan rate of 0.02 V/s and step of 0.002V and CA was measured at a constant voltage of -1 V vs RHE with an interval of 10 s. The irregular line obtained from the chronoamperometric measurement (Figure 4.3a) is due to a volume change of electrolyte given the constant evaporation and reaction of it and subsequent refilling to 20 mL.

Electrochemical Impedance Spectroscopy (EIS) measurements were performed between 0.1 Hz and 0.1 MHz with 10 mV of amplitude perturbation. The EIS raw data were analyzed with ZView software (Scribner Associates), fitting the raw data to an equivalent circuit model (see **Figure A4.5 inset**) for extracting both capacitances and resistances. To investigate the dependence between the Series Resistance (Rs) and the concentration of the electrolyte, equivalent EIS data was obtained, using fresh samples, as a function of $KHCO_3$ concentration.

Tafel analyses were performed by measuring considering that the required experimental conditions for a valid analysis were met (i.e., no Ohmic distortions, no background currents and at least one decade of linearity in the Tafel curve).[46] Since Tafel slope are overpotential-dependent, Tafel analysis must to be done with data acquired in a steady state and free of iR drop.[45] Steady state LSV (ssLSV) were built by measuring subsequent 5-minute chronoamperometries, and averaging the last 60 s of the current vs time response, at each applied potential (**Figure A4.8**). Then, the iR drop corrected overpotentials were plotted vs log [J] extracting from these curves the Tafel slopes (**Figures 4.4b and c**). Although the obtained Tafel slopes are higher than expected for Tafel, Heyrovsky

or Volmer mechanisms, the observed trends are still informative for the evolution of the intrinsic activity of our catalyst.

Spectroelectrochemical (SEC) analysis was performed coupling electrochemical and spectroscopic techniques. Chronoamperometric measurements were carried on for the copper sulfide electrocatalyst and on a bare copper substrate in a three-electrode Raman electrochemical flow cell (RedoxMe) at different potentials while taking optical absorption spectra on a spectrophotometer UV-Vis-NIR (Perkin Elmer 1050+). To obtain additional data, the reactions were carried out both in bicarbonate electrolyte and in dry acetonitrile with and without adding water. Data was acquired in diffuse reflectance mode using an integrating sphere and the data was further converted into absorbance by the Kubelka-Munk equation. The measured spectra showed in Figure 4.5 are presented as differential spectra (ΔO.D.) from the absorption data.

- Products determination and quantification

The H_2 generation was monitored by gas chromatography measurements coupling the sealed cell to an Agilent Micro-GC gas chromatograph. Chronoamperometric measurements were carried on at three different potentials (-0.5 V, -0.8 V, -1 V) for half an hour each one. The faradaic efficiency (FE) was estimated through the relation: FE (%) = H2(exp)/ H2(theo), where H_2(exp) is the amount of evolved H_2 in mol, monitored every 5 min and H_2(theo) corresponds to the theoretical H_2 evolved calculated by the Faraday's law: n(mol) = jH_2t/nF, where jH_2 is the current density recorded during the chronoamperometry measurement, t is the time in seconds, n is the number of electrons transferred in the reaction and F is the Faraday constant, 96485.33 C mol-1. Furthermore, using the same procedure, long-term H_2 Faradaic efficiency

was determined by monitoring the evolved H_2 every 6 hours over 1 week of reaction.

Total reflection X-rays fluorescence (TXRF) analysis of the electrolyte before and after the electrochemical test was carried out using a S4 TSTAR, Bruker, equipped with a 17.5 keV Molybdenum primary excitation source (Figure A4.12).

Chapter 5

$Cu_{2-x}S$ electrocatalyst for the electrochemical reduction of CO_2

This chapter reports the electrocatalytic reduction of CO_2 using $Cu_{2-x}S$ films (presented in *Chapter 3*). Particularly, this study focuses on the use of this copper-derived electrocatalyst for the conversion of CO_2 to formate ($HCOO^-$), which is a high hydrogen density chemical, widely used in the chemical industry. More interestingly, a two-fold increase of the selectivity of the $Cu_{2-x}S$ electrocatalyst toward formate is reported here, reaching a ~ 75% Faradaic efficiency, when reusing the same electrode under chronopotentiometric conditions. The nature of this improvement was investigated by taking advantage of a combined powerful compositional and structural characterization including XRD, XPS, XANES, and *in-situ* XRD and Raman analyses of the Cu-based electrocatalyst after each catalytic use. Therefore, the reduced Cu species and their crystalline structure showed to be key for the evolution of the selectivity toward formate. Particularly, the amorphization of the Cu (111) facet after the electrochemical tests was determined crucial to supress the HER favouring the CO_2 reduction reaction selectivity toward formate. The conclusions shown in this chapter represent a step forward towards the design of Cu-based electrocatalysts for the electrochemical reduction of CO_2 to formate.

5.1 Introduction

The electrochemical reduction of carbon dioxide (CO_2ER) arises from the imperative need to reduce the high atmospheric CO_2 levels, thus simultaneously

producing fuels and feedstoks.[1-2] This multi-product synthetic process is appealing for industry due to its tunable selectivity, its mild reaction conditions and because it is easy to combine with other renewable energy sources. However, the implementation and scalability of the CO_2 electroreduction process is still challenging, due to its highly demanding thermodynamics, slow reaction kinetics and low current densities.[3-4] Therefore, the efforts to achieve efficient and scalable electrochemical systems for CO_2 reduction require targeted strategies to overcome their energy and selectivity barriers. Common strategies to control the reaction pathway consist of adjusting external parameters, such as electrolytes and applied voltages. However, the most explored approaches focus on the functional design of highly selective electrocatalysts.[5]

Current state-of-the-art Cu and Cu-based catalysts have garnered significant attention for the CO_2ER, due to their remarkable catalytic activity and selectivity.[6] Cu is the only metal capable of reducing CO_2 into various products including C_1 and C_{2+} (multi-carbon) compounds. Nevertheless, its selectivity for a specific product is still challenging.[7] The CO_2ER product distribution on Cu electrocatalysts has been identified to be dependent on various surface factors, including the exposed Cu facet, morphology, chemical states, chemical composition, doping, etc., which can alter the binding strength of key intermediates such as *CO and *OCCO during the electrorreduction reaction.[8] By introducing other elements into Cu metal electrodes, different bonding modes with Cu and multiple binding sites for intermediate species are activated, which have proven to have a big influence on the performance of the electrocatalyst.[9-11] Particularly, copper sulfides have emerged as promising electrocatalysts for CO_2ER, since the presence of S atom appears to effectively suppress the hydrogen evolution reaction (HER), and significantly influences the adsorption and desorption strength of CO_2 reduction intermediates.[12-13]

In this chapter, the catalytic activity and selectivity of $Cu_{2-x}S$ catalysts for the CO_2-to-formate electrochemical conversion are investigated. By reusing the electrocatalyst and selecting the appropriate measurement conditions, a remarkable Faradaic Efficiency for formate (FE_{HCOO^-}) of ~75% was achieved, (doubling that of the as-synthesized material) [12, 14-15]. Additionally, a comprehensive chemical and structural post electrochemical characterization of the electrodes including XPS, XANES, XRD, *in-situ* XRD and *in-situ* Raman revealed the formation of Cu (0) as the catalytically active species during CO_2 and suggests the influence of Cu (111) facet amorfization on the $HCOO^-$ selectivity.

5.2 Electrochemical CO_2 reduction

The electrochemical evaluation of the $Cu_{2-x}S$ electrocatalyst (*Chapter 3*) for the CO_2 reduction reaction was carried out in a two-compartment electrochemical cell (Redoxme) with a Nafion membrane separating both anode and cathode. The cathodic reaction was performed in the state-of-the-art CO_2-saturated 0.1 M $KHCO_3$ electrolyte,[16] while in the opposite side, 1 M KOH was employed as the anolyte. All the experimental details are described in **Appendix III, Experimental section**. The electrochemical transformation of CO_2 on $Cu_{2-x}S$ electrocatalyst was first tested by chronoamperometric (CA) measurements, for 1 hour, at four different fixed potentials, ranging from -0.4 to 1.0 V vs RHE (**Figure 5.1a**). Hydrogen (H_2) was estimated in these initial tests as the main product, since HER kinetics are highly competitive with that of CO_2ER. Formate ($HCOO^-$) was determined as the main CO_2ER product, while traces of carbon monoxide (CO) and methane (CH_4) were only detected at -1 V *vs* RHE. According to these results, -0.8 V *vs* RHE was selected as the optimum electrochemical potential to carry out the chronoamperometric tests.

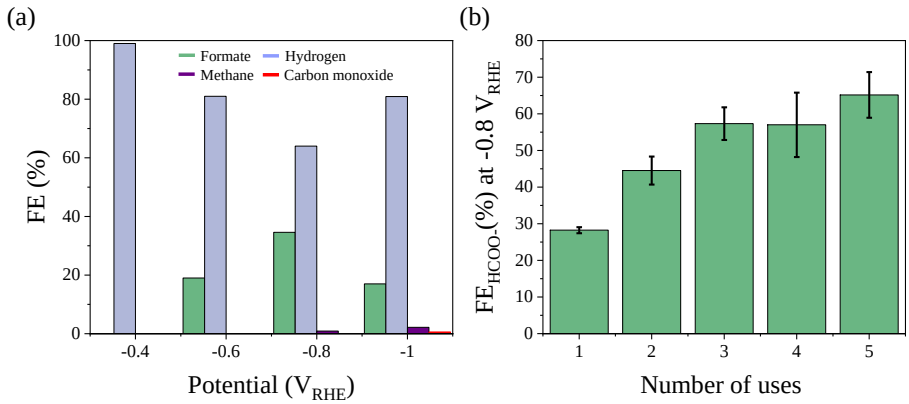

Figure 5.1. Evaluation of the Faradaic efficiencies towards formate after 1 hour of chronoamperometric measurements at different fixed potentials (a) and after several uses at the optimal potential (-0.8 V *vs* RHE).

To further investigate the CO_2 reduction with $Cu_{2-x}S$ electrodes, the reuse of the electrocatalyst was stablished as a study variable. With this purpose, a population of 30 samples was measured for five times each one and the generated $HCOO^-$ was monitored by HPLC after each use. **Figure 5.1b** shows the averaged Faradaic efficiency for formate (FE_{HCOO^-}) along with their standard deviation. The FE_{HCOO^-} reaches a plateau from the third to fifth use, showing the highest values at the fifth use, doubling the initial value. Additionally, blank experiments were performed, replicating the experiments with the electropolished copper substrates (**Appendix III, Figure A5.1**). Metallic copper electrocatalyst, exhibits FE_{HCOO^-} of 20%, slightly lower compared to that for $Cu_{2-x}S$, but more interestingly, these values do not grow with the catalyst use, but rather decreases. These results evince that the improvement in selectivity, when reusing the same $Cu_{2-x}S$ electrocatalyst, comes from a possible evolution of the $Cu_{2-x}S$ electrode and is not related to the Cu substrate.

Interestingly, within the entire sample population assessed, the best FE_{HCOO^-} values were obtained at a current density around -6.5 $mA \cdot cm^{-2}$ (**Figure 5.2a**). These findings suggest a kinetic dependence between the current density and the

product distribution during the electrochemical reduction of CO_2. Specifically, the favourable electrocatalytic reduction of CO_2 has been observed at low current densities, due to its slow electron transfer kinetics.[17] According to these findings, the catalytic activity of the $Cu_{2-x}S$ electrodes for the CO_2ER was subsequently evaluated by 1 h chronopotentimetric (CP) measurements at four different current densities: -4.5 mA·cm^{-2}, -6.5 mA·cm^{-2}, -8.5 mA·cm^{-2} and -10.5 mA·cm^{-2} (**Figure 5.2b**). From this figure, -6.5 mA·cm^{-2} was confirmed as the optimal current density for the selective CO_2-to-formic conversion. Further electrochemical tests were performed at -6.5 mA·cm^{-2} for 1 h exhibiting slightly enhanced FE_{HCOO^-} that also tended to improve with the number of uses (solid bars in **Figure 5.3**). Note that when controlling the reaction kinetics through CP measurements, only 2 uses are required to reach~75% FE_{HCOO^-}.

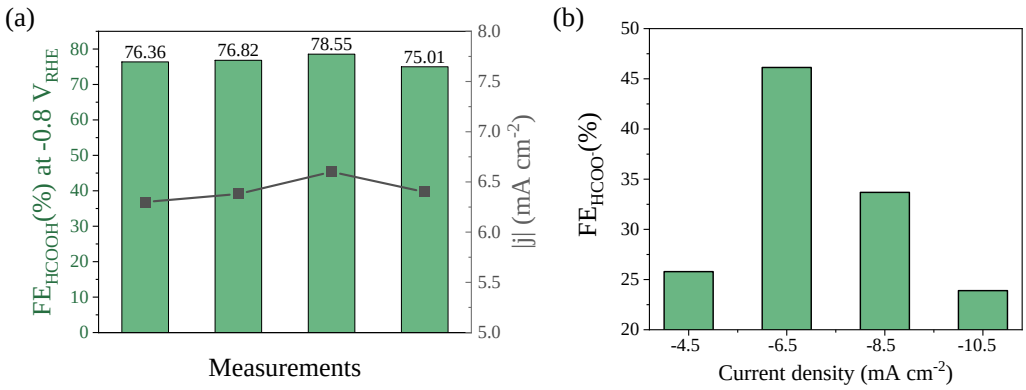

Figure 5.2. (a) A compilation of the best FE_{HCOO^-} values of chronoamperometric measurements at -0.8 V *vs* RHE for 1 hour and (b) evaluation of the FE toward formate at different fixed current density for 1 hour reaction.

To investigate the nature of this enhanced selectivity, the $Cu_{2-x}S$ electrodes were structurally and compositionally characterized by SEM, EDS and XRD after the first, second and third use, since it is between these uses where the greatest change in FE_{HCOO^-} takes place. A comparison of the top-view SEM images of the $Cu_{2-x}S$ electrocatalyst before and after the electrochemistry (**Appendix III,**

Figure A5.2) exhibits the formation of different nanocrystalline structures including nanocubes, previously reported to correspond to CuO/Cu_2O phases.[18-21] Further, EDS analysis on theses nanocubes confirms their Cu-O composition (**Appendix III, Figure A5.3**). Post-mortem X-ray diffractograms exhibit an intense peak at the 2Θ value of 36.48°, which corresponds to the formation of CuO (PDF #892531). Another minor peak at 61.4° is assigned to the formation of Cu_2O (PDF #653288), (**Appendix III, Figure A5.4**). These results may suggest that these observed Cu_xO nanocrystals may play a role on the catalysis, enhancing the selectivity toward formate.

To control the oxidation of the electrocatalyst and investigate its plausible relation with the increase of the selectivity toward formate, several electrodes were measured three times in inert atmosphere conditions. For this propose: (i) the electrolyte was purged for 1 h with N_2 to evacuate as much oxygen as possible from the solutions and (ii) a portable glovebox with N_2 flow was employed as an oxygen-free transfer platform between uses. The measurements conducted under N_2 conditions yielded a selectivity toward $HCOO^-$ slightly superior to the results obtained in the presence of oxygen (patterned bars in **Figure 5.3**). Both experiments, under air and N_2 atmosphere, exhibit a more significant improvement in the selectivity between the first and second use, from ~42% to ~68% and from ~44% to ~75%, respectively. However, the FE_{HCOO^-} values in the second and third use remain almost constant. The similarity in the evolution of selectivity between the second and third use, suggests that the most significant evolution in the electrocatalyst, affecting the change in the selectivity of the reaction, occurs mainly after measuring the electrode once.

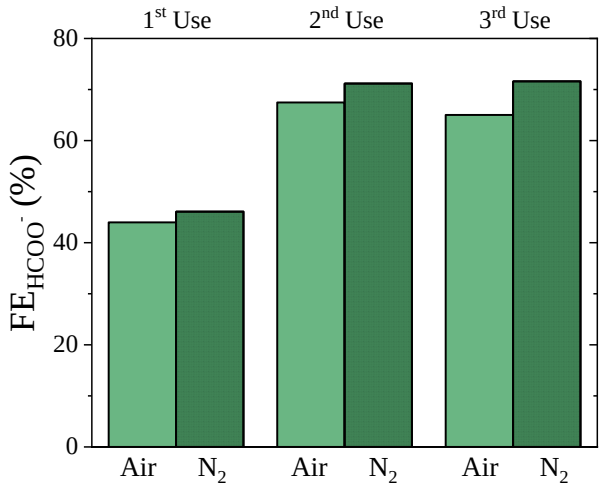

Figure 5.3. Comparison of the evolution of the FE_{HCOO^-} for three cycles measured in air (green solid bars) and in N_2 atmosphere (dark green patterned bars).

5.3 Compositional and morphological characterization

The chemical composition of the electrodes after the N_2-experiments was investigated by XPS and XANES. Analogously to the quasi-in situ XPS measurements in *Chapter 4*, the electrodes were washed, dried and transferred for the XPS analysis under a nitrogen flow. The Ar^+ sputtering protocol was also reproduced to enhance beam penetration and avoid surface contamination. **Figures 5.4a** and **b** show, respectively, the Cu LMM Auger transition and S 2p core level emission of the electrocatalyst before (blue line) and after the first and second electrochemical test (green and violet lines, respectively). The XPS spectra in **Figure 5.4a** show an evolution of the Cu (I, II) (K.E. 568.21 eV) components in the Cu LMM spectra towards reduced Cu, attributed to the increase of the Cu (0) (K.E. 5.70.16 eV) component after the electrochemical measurements. On the other hand, a decrease of the S2p component takes place with cycles (**Figure 5.4b**), observing almost complete depletion of S after the

second use, in agreement with previously discussed HER experiments in *Chapter 4*.

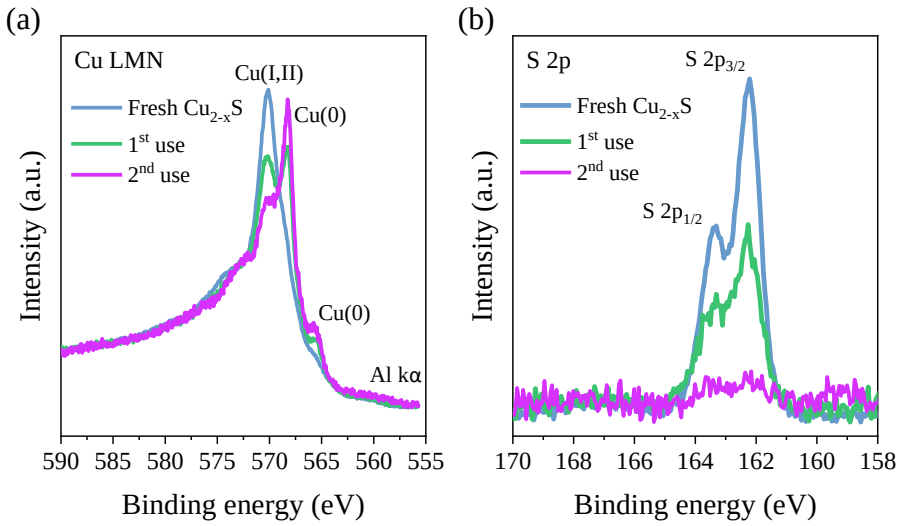

Figure 5.4. XPS characterization of the electrodes before (blue line) and after the first (green line) and the second (violet line) use. (a) Cu LMM and (b) S 2p spectra.

To gain further insights into the composition of the electrodes, XANES characterization of the electrocatalyst before and after the electrochemical tests was conducted. To properly characterize the Cu species, the electrocatalysts were scraped and sealed with kapton tape to preserve the inert atmosphere. **Figure 5.5** shows the XANES spectra of the $Cu_{2-x}S$ electrocatalyst, fresh and after 1 and 2 uses, as well as Cu foil and CuO powder as standards (black and red line, respectively). The Cu foil shows its typical edge of absorption around 8980 eV with the maximum absorption normalised at 1, whilst the as-prepared $Cu_{2-x}S$ filmshows the most oxidised Cu atoms. Interestingly, after the electrochemistry, the scraped electrocatalysts look slightly more reduced (left shifted peak). The edge of the samples after 1 and 2 uses in CO_2ER catalysis appears at a similar energy compared to that for CuO, signifying that the samples display a significant character of reduced copper, similarly to Cu (I), species. The presence of these reduced copper species could arise from either (i) a mixture Cu (II) and Cu (0)

from the as-prepared material and the metallic Cu after catalysis as observed by XPS, or (ii) from the presence of a significant amount of Cu (I). However, given that the XANES spectra of the samples after 1 and 2 uses do not exhibit the peak at 8995 eV, shown by the CuO standard (suggesting they do not have an oxide character), and have a small peak at 8986 eV (similar to the Cu foil 8983 eV peak), the presence of Cu (0) is suggested as a plausible component of the samples.[22-23] The higher derivative spectra of copper XANES normalized spectra were introduced in order to improve copper XANES resolution and facilitate the analysis (**Figure 5.5**, inset). These spectra clearly show that the edge of the Cu (0) is the most reduced, whilst the edge of the $Cu_{2-x}S$ is the most oxidised (towards the right). From these derivative spectra it is more evident that after reaction, the $Cu_{2-x}S$ samples show a mixture of Cu (II)/Cu (0) oxidation states. These results are consistent with the XPS spectra shown in **Figure 5.4** after the first and second uses in CO_2ER catalysis.

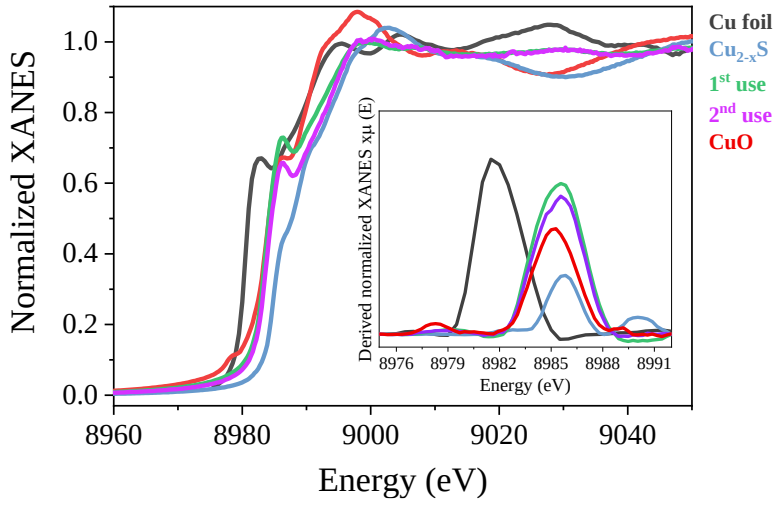

Figure 5.5. Normalized copper K-edge XANES spectra for the Cu metal foil (black line), the as-synthetized $Cu_{2-x}S$ (blue line), after the first use (green line) and after the second use (violet line) and the CuO pattern (red line). **Inset:** derivative normalized XANES spectra showing the characteristic Cu (0) absorption peak around 8980 eV and right shifted Cu (I) absorption peaks around 8986 eV.

XANES and XPS analyses on the electrocatalysts after the first and second electrochemical cycle reveal (i) their Cu (0)/Cu (I) composition and (ii) no evidences of oxides formation. Therefore, the hypothesis of improved selectivity with the formation of Cu_xO is ruled out. Thus, to gain further insights on the catalytically active species involved in the selectivity enhancement, *operando* XRD, *in-situ* Raman and *ex-situ* XRD analysis were conducted on the electrodes.

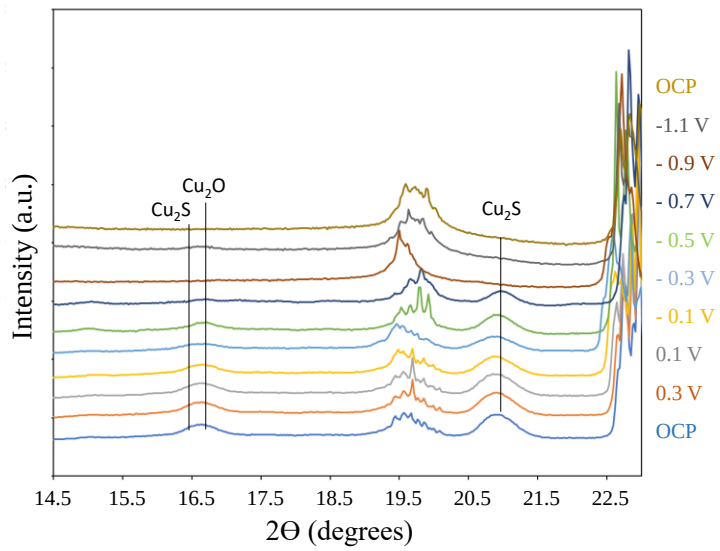

Figure 5.6. Operando XRD diffractograms of the $Cu_{2-x}S$ electrocatalyst from OCP to -1.0 and to back to OCP.

Figure 5.6 shows the evolution of the collected XRD patterns when the potential is progressively increased from open circuit potential (OCP) to -1.1 V vs RHE and returned to the OCP. At OCP conditions, characteristic phases of Cu, Cu_2S and superficial Cu_2O are observed. At more negative potentials, the Cu_2S and Cu_2O peaks disappear, while the Cu (0) peak grow, analogously to the HER (*Chapter 4*). Interestingly, when returning to OCP, the electrode exhibits only the Cu (0) signal and no oxidized Cu species are present. These results confirm that (i) Cu (0) are the catalytically active species that lead the CO_2ER and (ii) oxidized

Cu (**Appendix III, Figure A5.2**) have their nature in the transition between electrochemical cycles.

Moreover, *in-situ* Raman characterization of the $Cu_{2-x}S$ electrode was carried out on as-synthetized samples, in OCP conditions at the beginning and after successive linear sweep voltametries (LSV) and upon applying -0.8 V *vs* RHE (**Figure 5.7**). The spectra show the HCO_3^- and CO_3^{2-} bands of the electrolyte at 1020 and 1070 cm^{-1}, respectively[24]. After the first LSV, the bands assigned to Cu-O and S-O disappear, consistent with the formation of Cu (0) species, as soon as cathodic currents are generated. When futher LSV scans are carried out, an incipient band around 1550 cm^{-1},related to the formation of formate, appears. These findings suggest that controlled measurement cycles can presumably activate the catalyst for the formation of formate, thus modulating its selectivity.

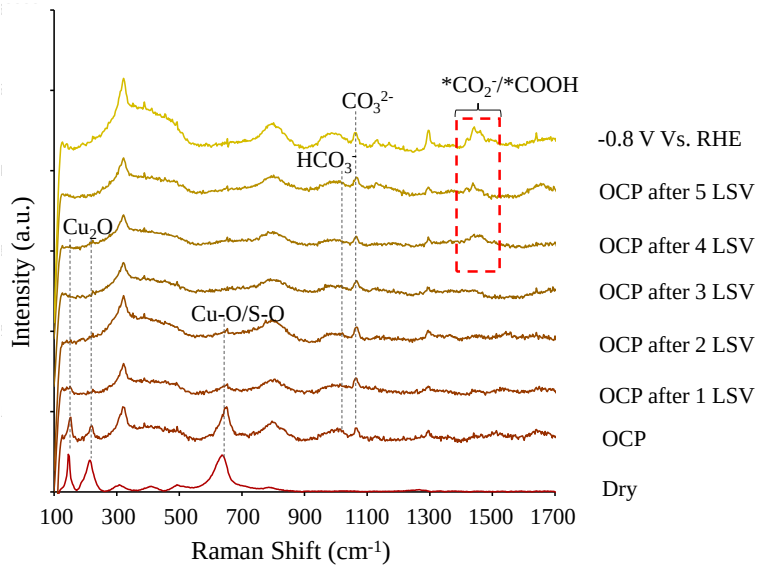

Figure 5.7. *In-situ* Raman characterization. LSVs were carried out from OCP to -0.8 V vs RHE at 10 mV/s in 0.1 M $KHCO_3$ (CO_2 saturated). Experiments performed from bottom to top.

Complementary *ex-situ* XRD characterization of the electrodes was carried out after the first, second and third use. To prevent oxidative effects from air

exposure, the electrodes were manipulated under nitrogen atmosphere and sealed with kapton. The collected XRD spectra in **Figure 5.8** show the two characteristic peaks of metallic Cu at 46.6° and at 50.7°, while no relevant peaks assigned to Cu_xS or Cu_xO are observed. The evolution of the oxidized Cu (I/II) species from the $Cu_{2-x}S$ catalyst (**Appendix III, Figure A5.4**, bottom) toward Cu (0) after electrochemical measurements is consistent with the *in-situ* XRD characterization in **Figure 5.6**. Most notably, the diffraction signals for metallic copper, particularly Cu (111) facet, undergo progressive amorphization over the uses in CO_2ER catalysis. These gradual amorphization suggests a surface reconstruction when increasing the number of cycles.[25] This bias effect was previously observed on Cu and Cu-derived electrocatalysts[18, 26] and was further correlated to the catalytic selectivity.[20, 27] Roldan and co-workers, reported that subtle changes in well-oriented Cu (100) and Cu (111) single-crystal surfaces affect their CO_2ER selectivity. Clean, flat, atomically ordered surfaces are predicted to yield hydrocarbons such as CO, CH_4, C_2H_4 and $HCOO^-$; but these flat structures actually favour production of H_2. Nevertheless, when introducing roughness and defects, significant amounts of hydrocarbons are generated. [28] Indeed, structural and morphological defects are key factors determining the catalytic selectivity of CO_2ER. Therefore, the herein reported enhancement of the selectivity of the $Cu_{2-x}S$ electrocatalyst with uses (**Figure 5.3**) may potentially be attributed to a Cu (111) reconstruction. Partially disordered Cu (111) would exhibit major selectivity toward the CO_2-to-formate conversion while suppressing the HER.

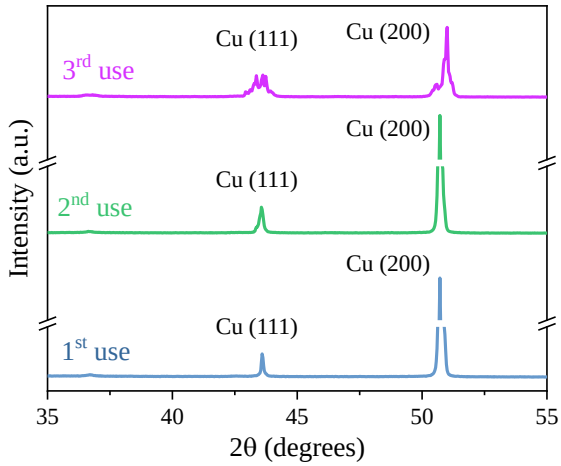

Figure 5.8. *Ex-situ* XRD characterization of the $Cu_{2-x}S$ electrodes after one, two and three uses in nitrogen atmosphere.

5.4 Conclusions

In summary, this chapter shows different strategies to control the selectivity of $Cu_{2-x}S$ electrocatalysts for CO2 reduction towards formate. By applying an optimal current density of - 6.5 $mA \cdot cm^{-2}$ and reusing the catalyst, it was possible to improve the selectivity of CO_2ER to formate, while suppressing HER. Specifically, starting FE_{HCOO^-} values of 35% were increased to remarkable values of 75%. By means of an extensive in-situ and ex-situ characterization of the electrodes, it was determined that (i) Cu (0) are the actual catalytically active species for CO_2R, (ii) after the first measurement of $Cu_{2-x}S$, the catalyst evolves and presents a combination of Cu (I) and Cu (0) species, (iii) Cu (111) amorphizes with the number of uses and (iv) this structural reconstruction could be related to the improvement of selectivity. In conclusion, this chapter reports important insights about boosting the catalytic activity of Cu-based electrodes for CO_2ER toward formate. These strategies are key for the design of protocols to prepare highly efficient Cu-based electrocatalysts for CO_2ER.

5.5 References

1. Lee, M.-Y.; Park, K. T.; Lee, W.; Lim, H.; Kwon, Y.; Kang, S., Current achievements and the future direction of electrochemical CO2 reduction: A short review. *Critical Reviews in Environmental Science and Technology* **2020,** *50* (8), 769-815.
2. Park, S.; Wijaya, D. T.; Na, J.; Lee, C. W., Towards the large-scale electrochemical reduction of carbon dioxide. *Catalysts* **2021,** *11* (2), 253.
3. Yu, F.; Deng, K.; Du, M.; Wang, W.; Liu, F.; Liang, D., Electrochemical CO2 reduction: From catalysts to reactive thermodynamics and kinetics. *Carbon Capture Science & Technology* **2023,** *6*, 100081.
4. Jin, S.; Hao, Z.; Zhang, K.; Yan, Z.; Chen, J., Advances and challenges for the electrochemical reduction of CO2 to CO: from fundamentals to industrialization. *Angewandte Chemie* **2021,** *133* (38), 20795-20816.
5. Garg, S.; Li, M.; Weber, A. Z.; Ge, L.; Li, L.; Rudolph, V.; Wang, G.; Rufford, T. E., Advances and challenges in electrochemical CO 2 reduction processes: an engineering and design perspective looking beyond new catalyst materials. *Journal of Materials Chemistry A* **2020,** *8* (4), 1511-1544.
6. Hori, Y.; Murata, A.; Takahashi, R.; Suzuki, S., Electroreduction of carbon monoxide to methane and ethylene at a copper electrode in aqueous solutions at ambient temperature and pressure. *Journal of the American Chemical Society* **1987,** *109* (16), 5022-5023.
7. Gao, D.; Arán-Ais, R. M.; Jeon, H. S.; Roldan Cuenya, B., Rational catalyst and electrolyte design for CO2 electroreduction towards multicarbon products. *Nature Catalysis* **2019,** *2* (3), 198-210.
8. Tomboc, G. M.; Choi, S.; Kwon, T.; Hwang, Y. J.; Lee, K., Potential link between Cu surface and selective CO2 electroreduction: perspective on future electrocatalyst designs. *Advanced Materials* **2020,** *32* (17), 1908398.
9. Li, Y. C.; Wang, Z.; Yuan, T.; Nam, D.-H.; Luo, M.; Wicks, J.; Chen, B.; Li, J.; Li, F.; De Arquer, F. P. G., Binding site diversity promotes CO2 electroreduction to ethanol. *Journal of the American Chemical Society* **2019,** *141* (21), 8584-8591.
10. Zhou, Y.; Che, F.; Liu, M.; Zou, C.; Liang, Z.; De Luna, P.; Yuan, H.; Li, J.; Wang, Z.; Xie, H., Dopant-induced electron localization drives CO2 reduction to C2 hydrocarbons. *Nature chemistry* **2018,** *10* (9), 974-980.
11. Hoang, T. T. H.; Verma, S.; Ma, S.; Fister, T. T.; Timoshenko, J.; Frenkel, A. I.; Kenis, P. J. A.; Gewirth, A. A., Nanoporous copper–silver alloys by additive-controlled electrodeposition for the selective electroreduction of CO2 to ethylene and ethanol. *Journal of the American Chemical Society* **2018,** *140* (17), 5791-5797.

12. Deng, Y.; Huang, Y.; Ren, D.; Handoko, A. D.; Seh, Z. W.; Hirunsit, P.; Yeo, B. S., On the role of sulfur for the selective electrochemical reduction of CO2 to formate on CuS x catalysts. *ACS applied materials & interfaces* **2018,** *10* (34), 28572-28581.
13. García-Muelas, R.; Dattila, F.; Shinagawa, T.; Martín, A. J.; Pérez-Ramírez, J.; López, N., Origin of the selective electroreduction of carbon dioxide to formate by chalcogen modified copper. *The Journal of Physical Chemistry Letters* **2018,** *9* (24), 7153-7159.
14. Lim, J. W.; Dong, W. J.; Park, J. Y.; Hong, D. M.; Lee, J.-L., Spontaneously Formed CuS x Catalysts for Selective and Stable Electrochemical Reduction of Industrial CO2 Gas to Formate. *ACS applied materials & interfaces* **2020,** *12* (20), 22891-22900.
15. Shinagawa, T.; Larrazábal, G. O.; Martín, A. J.; Krumeich, F.; Perez-Ramirez, J., Sulfur-modified copper catalysts for the electrochemical reduction of carbon dioxide to formate. *ACS Catalysis* **2018,** *8* (2), 837-844.
16. Li, T.; Yang, C.; Luo, J.-L.; Zheng, G., Electrolyte driven highly selective CO2 electroreduction at low overpotentials. *ACS Catalysis* **2019,** *9* (11), 10440-10447.
17. Sun, Z.; Ma, T.; Tao, H.; Fan, Q.; Han, B., Fundamentals and challenges of electrochemical CO2 reduction using two-dimensional materials. *Chem* **2017,** *3* (4), 560-587.
18. Arán-Ais, R. M.; Rizo, R.; Grosse, P.; Algara-Siller, G.; Dembélé, K.; Plodinec, M.; Lunkenbein, T.; Chee, S. W.; Cuenya, B. R., Imaging electrochemically synthesized Cu2O cubes and their morphological evolution under conditions relevant to CO2 electroreduction. *Nature communications* **2020,** *11* (1), 3489.
19. Herzog, A.; Bergmann, A.; Jeon, H. S.; Timoshenko, J.; Kühl, S.; Rettenmaier, C.; Lopez Luna, M.; Haase, F. T.; Roldan Cuenya, B., Operando Investigation of Ag-Decorated Cu2O Nanocube Catalysts with Enhanced CO2 Electroreduction toward Liquid Products. *Angewandte Chemie International Edition* **2021,** *60* (13), 7426-7435.
20. Rossi, K.; Buonsanti, R., Shaping copper nanocatalysts to steer selectivity in the electrochemical CO2 reduction reaction. *Accounts of Chemical Research* **2022,** *55* (5), 629-637.
21. Zhao, J.; Zhao, Y.; Yue, W.-C.; Zheng, S.-M.; Li, X.; Gao, N.; Zhu, T.; Zhang, Y.-J.; Xia, G.-M.; Wang, B., Facile fabrication of hollow CuO nanocubes for enhanced lithium/sodium storage performance. *CrystEngComm* **2021,** *23* (35), 6107-6116.
22. Gaur, A.; Shrivastava, B. D.; Joshi, S. K. In *Copper K-edge XANES of Cu (I) and Cu (II) oxide mixtures*, 2009; IOP Publishing: p 012084.

23. Klysubun, W.; Thongkam, Y.; Pongkrapan, S.; Won-in, K.; T-Thienprasert, J.; Dararutana, P., XAS study on copper red in ancient glass beads from Thailand. *Analytical and bioanalytical chemistry* **2011,** *399*, 3033-3040.
24. Zhan, C.; Dattila, F.; Rettenmaier, C.; Bergmann, A.; Kühl, S.; García-Muelas, R.; López, N. r.; Cuenya, B. R., Revealing the CO coverage-driven C–C coupling mechanism for electrochemical CO2 reduction on Cu2O nanocubes via operando Raman spectroscopy. *ACS catalysis* **2021,** *11* (13), 7694-7701.
25. Zhu, Y.; Kuo, T.-R.; Li, Y.-H.; Qi, M.-Y.; Chen, G.; Wang, J.; Xu, Y.-J.; Chen, H. M., Emerging dynamic structure of electrocatalysts unveiled by in situ X-ray diffraction/absorption spectroscopy. *Energy & Environmental Science* **2021,** *14* (4), 1928-1958.
26. Kim, Y.-G.; Baricuatro, J. H.; Javier, A.; Gregoire, J. M.; Soriaga, M. P., The evolution of the polycrystalline copper surface, first to Cu (111) and then to Cu (100), at a fixed CO2RR potential: a study by operando EC-STM. *Langmuir* **2014,** *30* (50), 15053-15056.
27. Grosse, P.; Yoon, A.; Rettenmaier, C.; Herzog, A.; Chee, S. W.; Roldan Cuenya, B., Dynamic transformation of cubic copper catalysts during CO2 electroreduction and its impact on catalytic selectivity. *Nature communications* **2021,** *12* (1), 6736.
28. Scholten, F.; Nguyen, K. L. C.; Bruce, J. P.; Heyde, M.; Roldan Cuenya, B., Identifying Structure–Selectivity Correlations in the Electrochemical Reduction of CO2: A Comparison of Well-Ordered Atomically Clean and Chemically Etched Copper Single-Crystal Surfaces. *Angewandte Chemie International Edition* **2021,** *60* (35), 19169-19175.

APPENDIX III

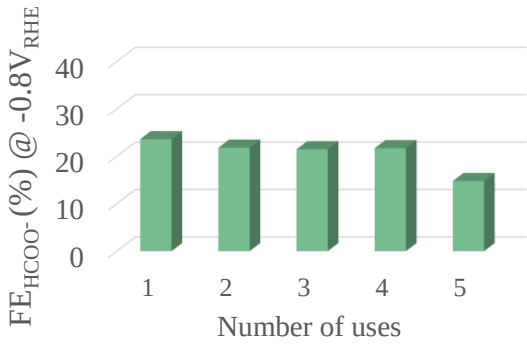

Figure A5.1. Blank experiment for CO_2R with electropolished Cu foil. Faradaic efficiencies toward formate after 1h of CA at -0.8 V *vs* RHE in each use.

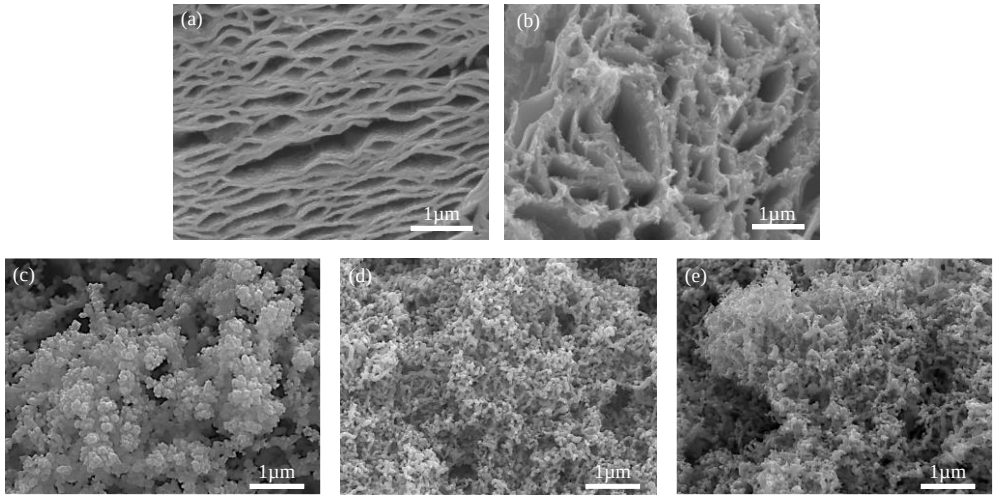

Figure A5.2. Top-view SEM images of the $Cu_{2-x}S$ electrocatalyst before (a) and after the electrochemical test (b-e). (b) SEM image showing the formation of nanocrystals/nanocubes on the reticular structure of the $Cu_{2-x}S$ in (a) after 1 h CA at -0.8 V *vs* RHE. Top-view SEM images of these structures characterized after the first (c), second (d) and third (e) use.

(a)

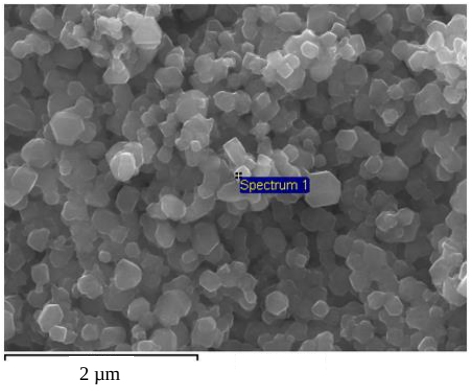

(b)

Element	Weigh (%)	Atomic (%)
K K	0.18	0.47
Cu K	31.27	49.65
O	7.91	49.88
Total		100

Figure A5.3. (a) Top-view SEM images of the Cu-derived electrocatalyst after 1 h CA at -0.8 V *vs* RHE for each use and (b) EDS analysis of the selected area in (a) showing a stoichiometric Cu-O ratio of 1:1. The presence of K is due to the electrolyte composition: CO_2 sat. 0.1 M $KHCO_3$.

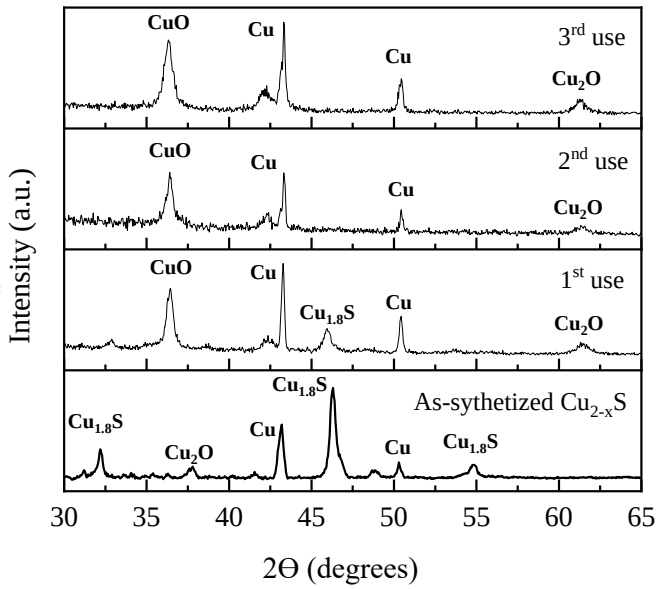

Figure A5.4. X-ray diffractogram of the electrodes after the first, second and third use. Compared to the characterization of the as-synthetized electrodes detailed in C*hapter 3*, an intense peak appears at 2Θ values of 36.48° consistent with the formation of CuO (PDF #892531) and a weaker peak at 61.4° assigned to the formation of Cu_2O (PDF #653288). The rest of the peaks were already identified in the as-synthetized sample: the peaks around 43.1° and 50.4° corresponds to the metallic Cu substrate and the characteristic peaks of $Cu_{1.8}S$ at 32.35°, 46.16° and 54.85° disappear with the number of uses, due to sulfur leaching, as showed in chapter 4 for HER.

Experimental section

- Electrochemical measurements

The electrochemical performance of the electrodes was evaluated by linear sweep voltammetry (LSV), chronoamperometry (CA) and Chronopotentiometries (CP) using an Autolab potentiostat/galvanostat PGSTAT302 in a two-compartment electrochemical cell (you an indicate the commercial name and company). Aqueous Ag/AgCl (0.3M KCl, ALS, Japan) and a Pt wire (Alfa Aesar) were used as reference and counter electrode, respectively and a 1 cm^2 geometrical area $Cu_{2-x}S$ film as working electrode. Nafion 212 membrane was used as separator elements. CO_2 saturated potassium bicarbonate ($KHCO_3$) was chosen as electrolyte. All the potentials reported herein refer to the reversible hydrogen electrode (RHE) and were calculated through the Nernst equation: $V_{RHE} = V_{Ag/AgCl} + 0.199 + 0.059 \cdot pH$. LSVs were performed between 0.1 and -1 V vs RHE with a scan rate of 0.01 V/s and step of 0.002 V, CAs were measured at a constant potential of -0.8 V vs RHE for 1 h and CPs were measured at a constant current density of -6.5 $mA \cdot cm^{-2}$ for 1 h.

- Identification and quantification of products

The H_2 generation was monitored by gas chromatography measurements coupling the sealed cell to an Agilent Micro-GC gas chromatograph. The faradaic efficiency (FE) was estimated through the relation: FE (%) = H_2(exp)/ H_2(theo), where H_2(exp) is the amount of evolved H_2 in mol and H_2(theo) corresponds to the theoretical H_2 evolved calculated by the Faraday's law: $n(mol) = j_{H2}t/nF$, where j_{H2} is the current density recorded during the chronoamperometry measurement, t is the time in seconds, n is the number of electrons transferred in the reaction and F is the Faraday constant, 96485.33 C mol^{-1}.

The formate production was quantified by high performance liquid chromatography (HPLC). Electrolyte aliquots after each CP were collected and filtered with the appropriate filters before measurement to avoid problems of clogging. The product separation was performed on an ion-exchange ligand-exchange column, Agilent Hi-Plex and 20:80 acetonitrile:10 mM H_2SO_4 was used as mobile phase. The measurements were conducted on a HPLC Agilent 1260 Infinity II LC System provided with a Diode Array Detector (DAD) and a Refractive Index Detector (RID).

Chapter 6

Switchable $CsPbBr_3$ NCs photoelectrodes for solar-driven organic transformations

In the previous chapters, the development of novel materials for electrocatalytic applications, using renewable electricity has been described. Further integration of renewable energy schemes can be obtained through photoelectrochemical energy conversion. New materials are also needed with excellent optoelectronic and photoelectrochemical properties. This chapter presents a proof-of-concept to validate the versatility of inorganic halide perovskite nanocrystalline ($CsPbBr_3$ NC) photoelectrodes to drive organic transformations. Interestingly, the photoelectrochemical behaviour of $CsPbBr_3$ NC films could be modulated through the proper choice of the selective contacts and accepting species in the electrolyte. The PEC functionality of the photoelectrodes was evaluated through the oxidation of benzyl alcohol (BzOH) to benzyl aldehyde (BzCHO) and the reverse reduction of BzCHO to BzOH. The obtained results highlight the huge potential and versatility of halide perovskite NCs for photoelectrocatalytic applications.

6.1 Introduction

All inorganic halide perovskite nanocrystals (NCs) have emerged in the last years as promising materials featuring defect-tolerant structure, high extinction coefficient,[1] ultrahigh photoluminescence quantum yield (PLQY),[2-3] multiple exciton generation and tunable bandgap (E_g) through composition engineering or

quantum confinement effect.[4-5] These excellent optoelectronic properties have boosted inorganic halide perovskite NCs as suitable materials for various solid-state energy conversion devices, such as photovoltaic solar cells,[6-7] light-emitting diodes (LEDs),[8-9] optically pumped lasers,[10] and photodetectors.[11-12] This broad range of optoelectronic applications takes advantage of the high PLQY of halide perovskite NCs, due to their low non-radiative carrier recombination.[3] More recently, these systems are receiving increasing attention for solar-driven photocatalytic and photoelectrocatalytic applications. Specifically, inorganic halide perovskite NCs, [13-15] are gaining interest due to their proven ability to transfer photogenerated charges to a liquid solution, targeting: H_2 generation,[16] degradation of dyes and organic pollutants,[17-18] organic transformations[5, 19], CO_2 reduction,[20-21] C-C coupling,[22] and photoelectrochemical sensing.[13]

Most of these studies are focused on photocatalytic applications, due to the high compatibility of the colloidal NCs with photocatalytic systems. In contrast, photoelectrochemical (PEC) applications require the homogeneous deposition of the colloidal NCs on (semi)conductive substrates, challenging the overall functional and mechanical stability of the films. However, the inherent advantages of the PEC configuration, have encouraged researchers to investigate boundary conditions and protocols to address these limitations.[23]

In this chapter, an interfacial engineering approach to tailor $CsPbBr_3$ NCs photoelectrodes for PEC applications is presented. Specifically, the photoelectrochemical behaviour of these materials could be designed with the adequate selective contacts[24-26] (NiO and TiO_2, as hole and electron transporting layers, respectively). To validate the concept, the organic transformation of benzyl alcohol (BzOH) to benzyl aldehyde (BzCHO) and the reverse reaction were targeted.[27-28]

6.2 Preparation of the photoelectodes

$CsPbBr_3$ NCs were prepared by a hot-injection synthetic method reported elsewhere.[29] The as-synthetized NCs exhibit the expected cubic morphology, (**Figure 6.1a**), with an average size of ~10 nm (**Figure 6.1b**) and featuring a bright green emission (508 nm) under UV illumination (**Figure 6.1c**). Subsequently, the NCs were spin-coated on FTO/TiO_2 and FTO/NiO substrates. All the experimental procedures are detailed in **Appendix V, Experimental section**. Both the FTO/TiO_2 and FTO/NiO with and without the photoactive layer of $CsPbBr_3$ NCs were characterized by AFM, SEM, EDS and XRD to confirm their structure and chemical composition, and to determine their thickness.

The thickness of TiO_2 and NiO undrelayers deposited on top of the 350 nm thick FTO was estimated by SEM cross-section images featuring thicknesses of approximately 30-40 nm (**Appendix V, Figure A6.1**). Furthermore, their elemental chemical composition was qualitatively estimated through EDS analysis (**Appendix V, Figure A6.2** and **Table A6.1**) and their crystalline structure was identified by XRD measurements (**Appendix V, Figure A6.3**). Similarly, the resulting $CsPbBr_3$ NCs heterostructured photoelectrode were characterized. AFM images (**Figure 6.1d** and **6.1g**) SEM top views (**Appendix V, Figure A6.4**) of the heterostrucured phototelectrodes reveal the formation of a continuous and homogeneous $CsPbBr_3$ NCs layer on the respective metal oxides. The homogeneous $CsPbBr_3$ NC thin films exhibited ~60 nm thickness on both substrates, TiO_2 and NiO, as evidenced by the cross-section SEM images in **Figure 6.1e** and **6.1h**, respectively. Their crystalline structure, identified through XRD, is shown as **Figure 6.1f** and **6.1i**, for NC layers deposited on TiO_2 and NiO substrates, respectively. Representative peaks are associated with the (100), (110), (200), (210), (211) and (202) planes from the perovskite structure with a

cubic phase (JCPDS card # 00-054-0752), consistently with previous studies.[30-31]

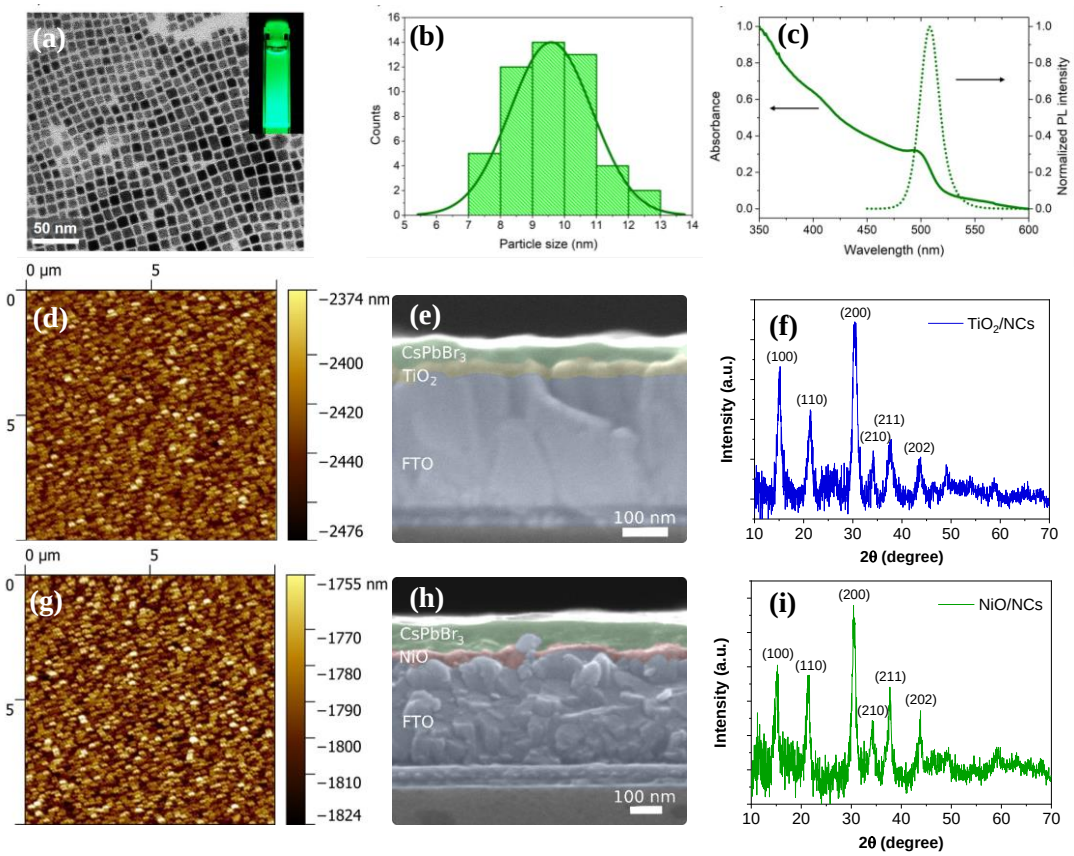

Figure 6.1 (a) Representative TEM image, (b) size distribution and (c) optical absorbance and emission spectra of the as-synthesized $CsPbBr_3$ NCs, (d) AFM top-view, (e) cross-section SEM images and (f) XRD diffractogram of the as-synthesized FTO/TiO_2/$CsPbBr_3$ heterostructured electrodes. (g) AFM top-view, (h) cross-section SEM images and (i) XRD diffractogram of the as-synthesized FTO/NiO/$CsPbBr_3$ heterostructured electrodes.

Steady-state photoluminescence (PL) measurements were also conducted on the NCs films deposited on glass, FTO, TiO_2 and NiO substrates, featuring an emission peak at 516 nm and a slight reduction of the Full-Width-at-Half-Maximum (FWHM) PL in the FTO/TiO_2/NCs and FTO/NiO/NCs, compared to the references glass/NCs and FTO/NCs. (**Appendix V, Figure A6.5a**). This

clearly indicates that the nature of the substrate does not modify the optical properties of the NCs, and provides particle size uniformity. On the other hand, the PL dynamics of the NCs was monitored by time-resolved photoluminescence (TRPL) measurements (**Appendix V, Figure A6.5b**). A slower PL decay was obtained in FTO/TiO_2/NCs and FTO/NiO/NCs films, compared to the reference FTO/NCs film, while glass/NCs film exhibits the longest PL decay. By fitting the PL decays through a bi-exponential function, $y = y_0 + A_1e^{-x/t1} + A_2e^{-x/t2}$, their corresponding average electron lifetimes, τ_{avg},[32] were estimated as 18.5, 23.7, 21.4 and 25.7 ns from NCs deposited on FTO, FTO/TiO_2, FTO/NiO and glass, respectively **(Appendix V, Table A6.2**). This is a clear evidence that the carrier transfer is promoted faster in FTO substrate, which does not present any selectivity to one type of photocarriers from NCs. However, the PL dynamics of $CsPbBr_3$ NCs is retarded when contacts such as TiO_2 and NiO layers are introduced. This feature is key to facilitate the selective extraction of electrons or holes, respectively, and promote the photoelectrochemical oxidation and reduction of organic compounds, as will be shown below.

6.3 Photoelectochemical evaluation

The photoactivity of the photoelectrodes was first evaluated by measuring the optical absorptance of the TiO_2 and NiO films with and without the $CsPbBr_3$ NCs. The optical absorbance spectra in **Figure 6.2a** clearly show their enhanced light harvesting efficiency upon deposition of the NCs, extending the absorption range from 350 nm to 550 nm, in good agreement with their optical absorbance reported in **Figure 6.1b**. The switchable photoelectrochemical (PEC) activity of the $CsPbBr_3$ NCS films towards oxidation and reduction reactions of BzOH and BzCHO, respectively was rationally designed through the energy diagrams from the literature.[31, 33-34]

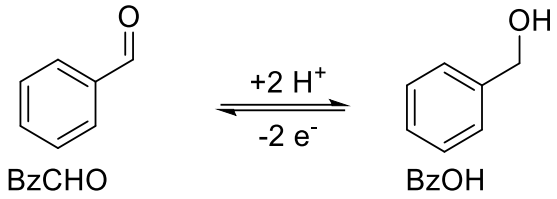

Scheme 6.1. Schematic of the reduction of benzaldehyde (BzCHO) and oxidation of benzyl alcohol (BzOH) reactions.

The tuneable PEC behaviour of the $CsPbBr_3$ NCs films was evaluated in 0.1 M tetrabutylammonium hexafluorophosphate in dichloromethane according to previous studies,[23, 31] which reported the optimized stability of the $CsPbBr_3$ NCs in these conditions. Cyclic voltammetry measurements in the dark and under illumination revealed the photoanodic behaviour of FTO/TiO_2/$CsPbBr_3$ NCs electrodes, as showed in **Figure 6.2b**. In this configuration, photogenerated holes at the halide perovskite NCs are driven towards the electrode/liquid solution interface, oxidizing the electron donor species, while the photogenerated electrons are driven to the TiO_2 contact and injected to the external circuit. These electrons lead to the reduction of the electron acceptor species at the cathode, closing the electronic circuit. Blank measurements with and without the $CsPbBr_3$ NCs layer confirmed the contribution of the $CsPbBr_3$ NCs enhancing this anodic photocurrent, see **Appendix V, Figure A6.6**. On the one hand, the addition of BzOH (concentration 0.05 M) leads to a four-fold increase of this anodic photocurrent, reflecting the activity of $CsPbBr_3$ NCs to photoelectro-oxidize this organic substrate at the photoelectrode/electrolyte interface (**Figures 6.2b** and **A6.6a**). On the other hand, cyclic voltammograms of the FTO/NiO/NCs films in the dark and under illumination confirmed the photocathodic behaviour of these electrodes, driving the photogenerated electrons to the semiconductor/liquid interface and transferring them to electron acceptor species in the solution. Upon addition of BzCHO as an electron acceptor, the photocurrent exhibits a three-fold enhancement, boosting from 50 $\mu A \cdot cm^{-2}$ to 150 $\mu A \cdot cm^{-2}$ (**Figures 6.2c** and

A6.6b), highlighting the favoured photo-reduction ability of the electrode for this two-electron transformation (see **scheme 6.1**).

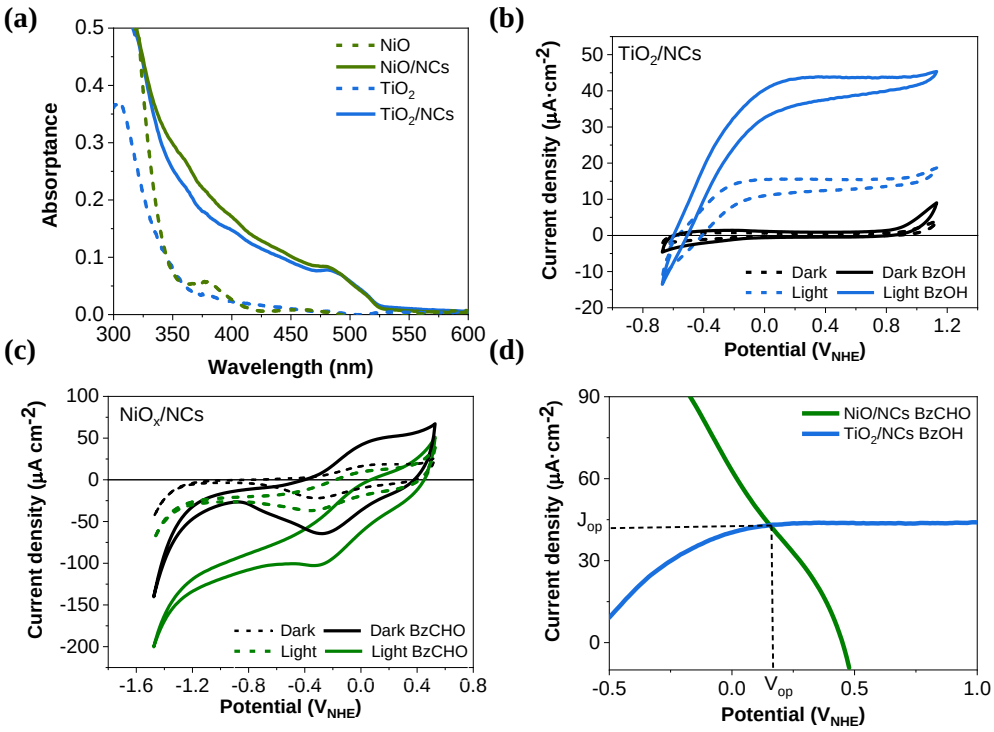

Figure 6.2. (a) Optical absorbance of the FTO/TiO_2 and FTO/NiO photoanodes with and without $CsPbBr_3$ NCs, (b) Cyclic voltammetry curves in the dark and under illumination showing the photocurrents of FTO/TiO_2/$CsPbBr_3$ NCs photoanodes with and without BzOH substrate in 0.1 M Bu_4NPF_6 in dichloromethane electrolyte, (c) Cyclic voltammetry curves in the dark and under illumination showing the photocurrents of FTO/NiO/$CsPbBr_3$ NCs photocathodes with and without BzCHO substrate in 0.1 M Bu_4NPF_6 in dichloromethane electrolyte, (d) Operation condition of the tandem arrangement of a photoanode and a photocathode for a photo-assisted BzOH/BzCHO fuel cell. A 400 nm high pass neutral filter was used to suppress photoexcitation of TiO_2 and NiO selective contacts or a plausible formation of singlet oxygen under UV light, which could react with the organic species.[35]

The successful photoelectro-oxidation of BzOH to BzCHO and the reverse photoelectro-reduction reactions could potentially be performed in a parallel tandem arrangement of photoanode and photocathode operating at 42 $\mu A \cdot cm^{-2}$ as shown in **Figure 6.2d**. This result, as a proof-of-concept, opens new horizons on

solar-driven electrochemical applications with halide perovskite NCs, spanning from redox-flow batteries[36] to solar-driven fuel cells.[37]

The PEC activity of FTO/TiO_2/NCs and FTO/NiO/NCs electrodes was evaluated by quantifying the produced BzCHO during BzOH oxidation and the generation of BzOH by reducing BzCHO, respectively. The transformation of BzOH into BzCHO, through a two-hole reaction was analytically monitored by HPLC. The chromatograms after the respective reactions show an increase in intensity with respect to the blank before the reaction at the retention times assigned to each product (1.28 min for benzyl alcohol and 1.57 min for benzaldehyde) as shown in **Figure A6.7**. Therefore, in view of these results, both conversions are confirmed to be taking place. Note that the quantification of BzCHO as well as BzOH for both oxidation and reduction reactions, proved to be challenging due to the low product concentration given by the low achieved photocurrents and stabilities of these photoelectrodes, detaching after a few minutes of operation. Few attempts of BzOH oxidation with perovskite NCs are shown in literature, for example, Huang *et. al.*, reported the photocatalytic oxidation of BzOH with TiO_2/organic inorganic halide perovskite NCs with a 60 % conversion rate, in an 8 hours experiment illuminating with a Xe lamp (with a AM1.5G filter to simulate the solar spectrum).[19] Indeed, several hours are generally needed in photocatalytic/photoelectrochemical experiments for the reliable assessment of both productivity and selectivity.[38] For example, a recent study with metal oxide photoanodes ($BiVO_4$) operating at higher current densities, was conducted for more than 12 hours for a quantitative assessment.[35] It is also plausible that once the $CsPbBr_3$ NCs detach from the electrode, they continue working as photocatalysts, with the reduction of BzCHO to BzOH being thermodynamically favourable compared to the oxidation of BzOH. This is supported by the relative positions of the valence and conduction bands with the

redox position of the BzCHO/BzOH couple depicted in **Figure 6.5**. Optical photographs of the photoelectrodes before and after electrochemical testing, under visible and UV illumination are showed in **Appendix V, Figure A6.8**. All the photoelectrochemical experiments were carried out with >400 nm light where alternative side reactions, driven by UV radiation, like singlet oxygen are ruled out for the oxidation of BzOH.[35]

Further insights into carrier dynamics were obtained through exploring the dependence of both photocurrent (J_{ph}) and photovoltage (V_{ph}) with illumination intensity. These parameters were measured for both photoanode and photocathode configurations, as illustrated in **Figure 6.3** and **6.4**. The photocurrent was evaluated at the working potential estimated from **Figure 6.2d**, (0.15 V vs. NHE) and the photo-voltage is defined as $V_{ph} = V_{light} - V_{dark}$, where V_{dark} and V_{light} are the open circuit potentials in the dark and under illumination (with filtered light < 400 nm), respectively. Both the FTO/TiO_2/NCs photoanode and FTO/NiO/NCs photocathodes show a linear dependence of J_{ph} with light intensity, see **Figure 6.3a**, **6.3b**, **Figure 6.4a** and **6.4b**, suggesting fast hole (electron) transfer kinetics from the $CsPbBr_3$ Valence (Conduction) Band to the BzOH (BzCHO), involving kinetic control of the photocurrent.[26] However, V_{ph} does not show a monotonic trend with light intensity, particularly at low light intensities (see **Figure 6.3c**, **6.3d** for oxidation and **Figure 6.4c**, **6.4d** for reduction), which could be related to the existence of surface defects leading to Fermi level pinning.[39]

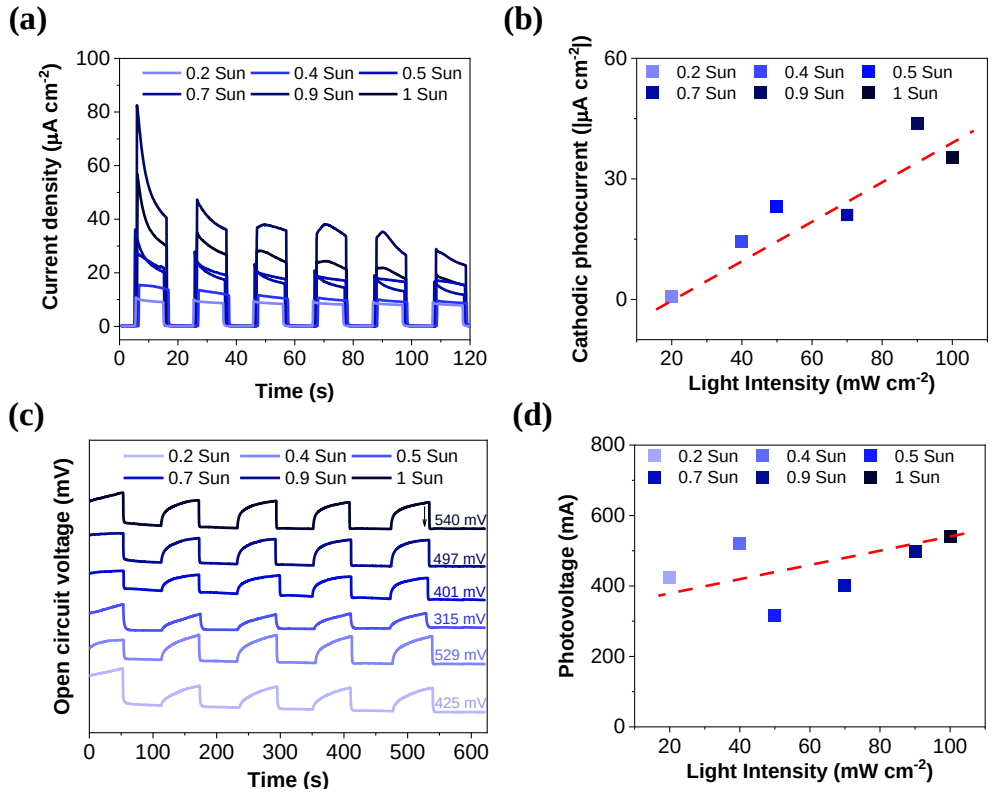

Figure 6.3. Chronoamperometric (a) and chronovoltammetric (c) measurements at different illumination intensities for BzOH photo-oxidation. The values of photopotential are indicated numerically, next to the specific plot. Relevant photocurrents and photopotentials corresponding to Figures (a) and (c) are showed as (b) and (d), respectively. The red dashed lines serve as eye guides. All measurements were performed in 0.05 M BzOH in 0.1 M Bu_4NPF_6 in dichloromethane electrolyte.

In contrast, the oxidation photocurrents (**Figure 6.3a**) decrease with time, while this is not the case for reduction photocurrents (**Figure 6.3e**), which is attributed to the significantly higher photocurrent values recorded for the oxidation tests.

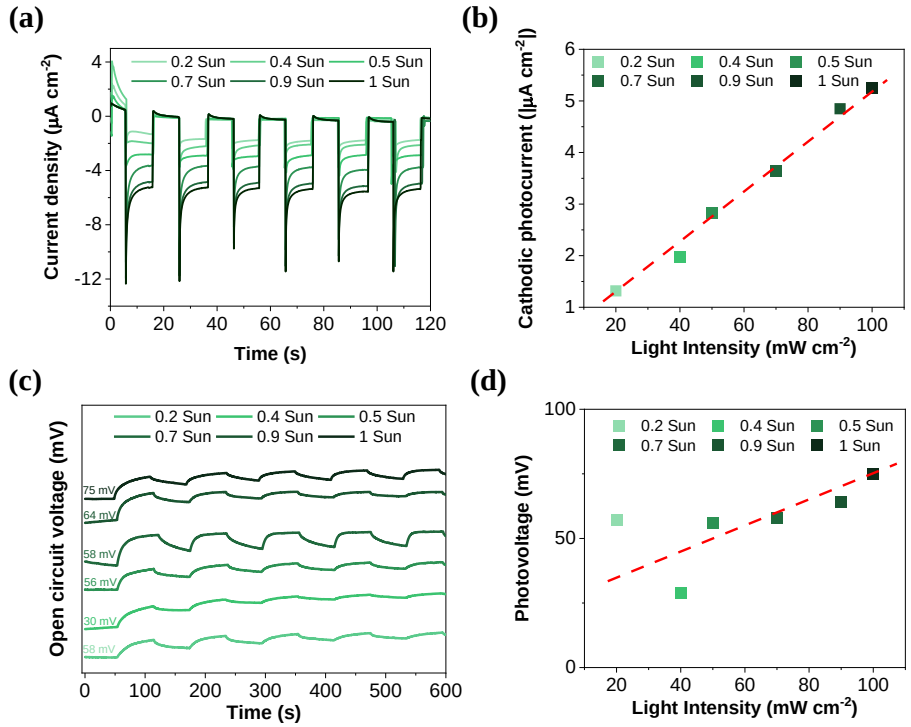

Figure 6.4. Chronoamperometric (a) and chronovoltammetric (c) measurements at different illumination intensities for BzCHO photo-reduction. The values of photopotential are indicated numerically, next to the specific plot. Relevant photocurrents and photopotentials corresponding to Figures (a) and (c) are showed as (b) and (d), respectively. The red dashed lines serve as eye guides. All measurements were performed in 0.05 M BzCHO in 0.1 M Bu_4NPF_6 in dichloromethane electrolyte.

The switchable photoelectrochemical (PEC) activity of the $CsPbBr_3$ NCS films towards oxidation and reduction reactions of BzOH and BzCHO, respectively can be rationalized through the energy diagrams scheduled in **Figure 6.5**. The relative positions of conduction and valence band of the heterostructured FTO/TiO_2/NCs and FTO/NiO/NCs electrodes were extracted from the literature.[31, 33-34] From these energy diagrams, it is clear that both BzOH oxidation and BzCHO reduction are thermodynamically favourable with photogenerated carriers at $CsPbBr_3$ NCs in the developed heterostructured electrodes, consistently with the voltammograms showed in **Figure 6.2**. Indeed, higher thermodynamic driving force exists for the photoelectro-reduction of BzCHO,

compared to the photoelectro-oxidation of BzOH, which may account for the enhanced photocurrents reported here for this reduction reaction. Consequently, interfacial engineering of all-inorganic halide perovskite NCs provides a versatile tool to harness the excellent optoelectronic properties of these materials towards sustainable photoelectrochemical transformations, highlighting the need for stabilization of these materials under operation conditions to move from proof-of-concept to more relevant technological developments. Promising on-going strategies, like ligand passivation[5] or core/shell structures,[14] will be key to achieve this goal.

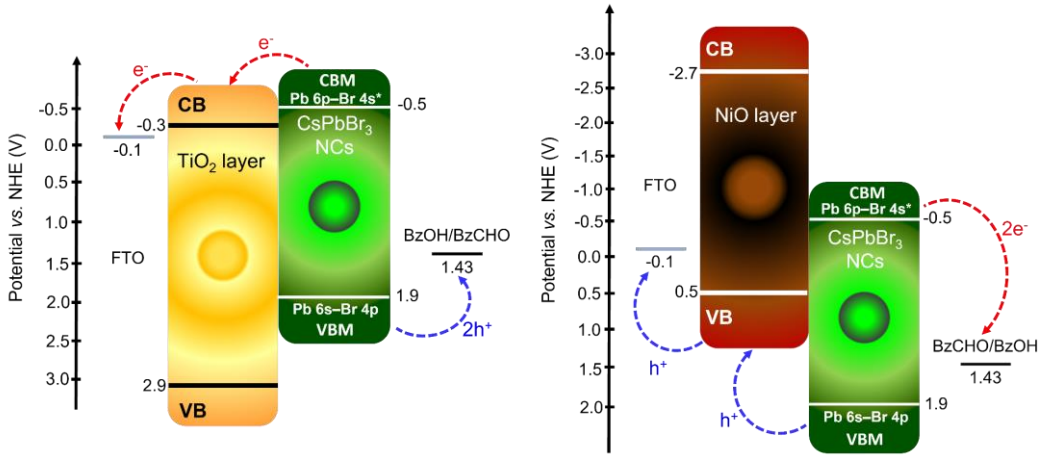

Figure 6.5. Band diagram of the $CsPbBr_3$ NC heterostructured photoelectrodes and redox potential of the benzyl alcohol/benzaldehyde.

6.4 Conclusions

In this chapter the switchable photoelectrochemical behavior of heterostructured $CsPbBr_3$ NCs films upon selective contact engineering is demonstrated. This concept has been applied to the solar-driven transformation of BzOH into BzCHO and vice versa. Both BzOH oxidation and BzCHO reduction are thermodynamically favourable, leading to meaningful photocurrents of 40 $\mu A \cdot cm^{-2}$ and 5 $\mu A \cdot cm^{-2}$ at 0.15 V vs NHE for photoelectro-

oxidation and photoelectro-reduction reactions, respectively. Indeed, higher thermodynamic driving force exists for the photoelectro-reduction of BzCHO, compared to the photoelectro-oxidation of BzOH, which may account for the enhanced photocurrents reported here for this reduction reaction. Kinetic control of the photocurrent takes place for both two-carrier reactions and absence of surface states participating in the charge transfer mechanisms is evidenced for BzOH oxidation, while photovoltage saturation for the photocathodic reaction may indicate Fermi level pinning. The proposed energy diagram is consistent with the functional behaviour reported and validates the strategy of selective contact engineering towards PEC applications with these materials. Further efforts are compulsory for the stabilization of NCs films under operation in a liquid solution, so the findings of the present study can translate into meaningful technological developments. Remarkably, the obtained results can pave the way towards a wide range of solar-driven synthesis of organic compounds, as well as the application of these promising materials for advanced electrochemical applications like redox flow batteries and solar-driven fuel cells.

6.6 References

1. Maes, J.; Balcaen, L.; Drijvers, E.; Zhao, Q.; De Roo, J.; Vantomme, A.; Vanhaecke, F.; Geiregat, P.; Hens, Z., Light Absorption Coefficient of CsPbBr3 Perovskite Nanocrystals. *The Journal of Physical Chemistry Letters* **2018,** *9* (11), 3093-3097.
2. Protesescu, L.; Yakunin, S.; Bodnarchuk, M. I.; Krieg, F.; Caputo, R.; Hendon, C. H.; Yang, R. X.; Walsh, A.; Kovalenko, M. V., Nanocrystals of Cesium Lead Halide Perovskites (CsPbX3, X = Cl, Br, and I): Novel Optoelectronic Materials Showing Bright Emission with Wide Color Gamut. *Nano Letters* **2015,** *15* (6), 3692-3696.
3. Gualdron-Reyes, A. F.; Masi, S.; Mora-Sero, I., Progress in halide-perovskite nanocrystals with near-unity photoluminescence quantum yield. *Trends in Chemistry* **2021,** *3* (6), 499-511.
4. Suri, M.; Hazarika, A.; Larson, B. W.; Zhao, Q.; Vallés-Pelarda, M.; Siegler, T. D.; Abney, M. K.; Ferguson, A. J.; Korgel, B. A.; Luther, J. M., Enhanced Open-Circuit Voltage of Wide-Bandgap Perovskite Photovoltaics by Using Alloyed (FA1–xCsx)Pb(I1–xBrx)3 Quantum Dots. *ACS Energy Letters* **2019,** *4* (8), 1954-1960.
5. Gualdron-Reyes, A. F.; Rodriguez-Pereira, J.; Amado-Gonzalez, E.; Rueda-P, J.; Ospina, R.; Masi, S.; Yoon, S. J.; Tirado, J.; Jaramillo, F.; Agourani, S.; Munoz-Sanjose, V.; Gimenez, S.; Mora-Sero, I., Unravelling the Photocatalytic Behavior of All-Inorganic Mixed Halide Perovskites: The Role of Surface Chemical States. *Acs Applied Materials & Interfaces* **2020,** *12* (1), 914-924.
6. Yuan, J.; Hazarika, A.; Zhao, Q.; Ling, X.; Moot, T.; Ma, W.; Luther, J. M., Metal Halide Perovskites in Quantum Dot Solar Cells: Progress and Prospects. *Joule* **2020,** *4* (6), 1160-1185.
7. Hao, M.; Bai, Y.; Zeiske, S.; Ren, L.; Liu, J.; Yuan, Y.; Zarrabi, N.; Cheng, N.; Ghasemi, M.; Chen, P.; Lyu, M.; He, D.; Yun, J.-H.; Du, Y.; Wang, Y.; Ding, S.; Armin, A.; Meredith, P.; Liu, G.; Cheng, H.-M.; Wang, L., Ligand-assisted cation-exchange engineering for high-efficiency colloidal Cs1−xFAxPbI3 quantum dot solar cells with reduced phase segregation. *Nature Energy* **2020,** *5* (1), 79-88.
8. Zhang, X.; Sun, C.; Zhang, Y.; Wu, H.; Ji, C.; Chuai, Y.; Wang, P.; Wen, S.; Zhang, C.; Yu, W. W., Bright Perovskite Nanocrystal Films for Efficient Light-Emitting Devices. *The Journal of Physical Chemistry Letters* **2016,** *7* (22), 4602-4610.
9. Wang, Y.-K.; Yuan, F.; Dong, Y.; Li, J.-Y.; Johnston, A.; Chen, B.; Saidaminov, M. I.; Zhou, C.; Zheng, X.; Hou, Y.; Bertens, K.; Ebe, H.; Ma, D.; Deng, Z.; Yuan, S.; Chen, R.; Sagar, L. K.; Liu, J.; Fan, J.; Li, P.; Li, X.; Gao,

Y.; Fung, M.-K.; Lu, Z.-H.; Bakr, O. M.; Liao, L.-S.; Sargent, E. H., All-inorganic quantum dot LEDs based on phase-stabilized α-CsPbI3 perovskite. *Angewandte Chemie International Edition* **2021,** *n/a* (n/a).
10. Wang, Y.; Li, X.; Song, J.; Xiao, L.; Zeng, H.; Sun, H., All-Inorganic Colloidal Perovskite Quantum Dots: A New Class of Lasing Materials with Favorable Characteristics. *Advanced Materials* **2015,** *27* (44), 7101-7108.
11. Saleem, M. I.; Yang, S.; Zhi, R.; Sulaman, M.; Chandrasekar, P. V.; Jiang, Y.; Tang, Y.; Batool, A.; Zou, B., Surface Engineering of All-Inorganic Perovskite Quantum Dots with Quasi Core−Shell Technique for High-Performance Photodetectors. *Advanced Materials Interfaces* **2020,** *7* (11), 2000360.
12. Bi, C.; Kershaw, S. V.; Rogach, A. L.; Tian, J., Improved Stability and Photodetector Performance of CsPbI3 Perovskite Quantum Dots by Ligand Exchange with Aminoethanethiol. *Advanced Functional Materials* **2019,** *29* (29), 1902446.
13. Liang, J.; Chen, D.; Yao, X.; Zhang, K.; Qu, F.; Qin, L.; Huang, Y.; Li, J., Recent Progress and Development in Inorganic Halide Perovskite Quantum Dots for Photoelectrochemical Applications. *Small* **2020,** *16* (15), 1903398.
14. Huang, H.; Pradhan, B.; Hofkens, J.; Roeffaers, M. B. J.; Steele, J. A., Solar-Driven Metal Halide Perovskite Photocatalysis: Design, Stability, and Performance. *ACS Energy Letters* **2020,** *5* (4), 1107-1123.
15. Wang, X.-D.; Miao, N.-H.; Liao, J.-F.; Li, W.-Q.; Xie, Y.; Chen, J.; Sun, Z.-M.; Chen, H.-Y.; Kuang, D.-B., The top-down synthesis of single-layered Cs4CuSb2Cl12 halide perovskite nanocrystals for photoelectrochemical application. *Nanoscale* **2019,** *11* (12), 5180-5187.
16. Xiao, M.; Hao, M.; Lyu, M.; Moore, E. G.; Zhang, C.; Luo, B.; Hou, J.; Lipton-Duffin, J.; Wang, L., Surface Ligands Stabilized Lead Halide Perovskite Quantum Dot Photocatalyst for Visible Light-Driven Hydrogen Generation. *Advanced Functional Materials* **2019,** *29* (48), 1905683.
17. Gao, G.; Xi, Q.; Zhou, H.; Zhao, Y.; Wu, C.; Wang, L.; Guo, P.; Xu, J., Novel inorganic perovskite quantum dots for photocatalysis. *Nanoscale* **2017,** *9* (33), 12032-12038.
18. Cardenas-Morcoso, D.; Gualdrón-Reyes, A. F.; Ferreira Vitoreti, A. B.; García-Tecedor, M.; Yoon, S. J.; Solis de la Fuente, M.; Mora-Seró, I.; Gimenez, S., Photocatalytic and Photoelectrochemical Degradation of Organic Compounds with All-Inorganic Metal Halide Perovskite Quantum Dots. *The Journal of Physical Chemistry Letters* **2019,** *10* (3), 630-636.
19. Huang, H.; Yuan, H.; Janssen, K. P. F.; Solís-Fernández, G.; Wang, Y.; Tan, C. Y. X.; Jonckheere, D.; Debroye, E.; Long, J.; Hendrix, J.; Hofkens, J.; Steele, J. A.; Roeffaers, M. B. J., Efficient and Selective Photocatalytic Oxidation

of Benzylic Alcohols with Hybrid Organic–Inorganic Perovskite Materials. *ACS Energy Letters* **2018,** *3* (4), 755-759.
20. Xu, Y.-F.; Yang, M.-Z.; Chen, B.-X.; Wang, X.-D.; Chen, H.-Y.; Kuang, D.-B.; Su, C.-Y., A CsPbBr3 Perovskite Quantum Dot/Graphene Oxide Composite for Photocatalytic CO2 Reduction. *Journal of the American Chemical Society* **2017,** *139* (16), 5660-5663.
21. Ou, M.; Tu, W. G.; Yin, S. M.; Xing, W. N.; Wu, S. Y.; Wang, H. J.; Wan, S. P.; Zhong, Q.; Xu, R., Amino-Assisted Anchoring of CsPbBr3 Perovskite Quantum Dots on Porous g-C3N4 for Enhanced Photocatalytic CO2 Reduction. *Angewandte Chemie-International Edition* **2018,** *57* (41), 13570-13574.
22. Wang, K.; Lu, H.; Zhu, X.; Lin, Y.; Beard, M. C.; Yan, Y.; Chen, X., Ultrafast Reaction Mechanisms in Perovskite Based Photocatalytic C–C Coupling. *ACS Energy Letters* **2020,** *5* (2), 566-571.
23. Samu, G. F.; Scheidt, R. A.; Kamat, P. V.; Janáky, C., Electrochemistry and Spectroelectrochemistry of Lead Halide Perovskite Films: Materials Science Aspects and Boundary Conditions. *Chemistry of Materials* **2018,** *30* (3), 561-569.
24. Mora-Sero, I.; Bertoluzzi, L.; Gonzalez-Pedro, V.; Gimenez, S.; Fabregat-Santiago, F.; Kemp, K. W.; Sargent, E. H.; Bisquert, J., Selective contacts drive charge extraction in quantum dot solids via asymmetry in carrier transfer kinetics. *Nature Communications* **2013,** *4*.
25. Guerrero, A.; Haro, M.; Bellani, S.; Antognazza, M. R.; Meda, L.; Gimenez, S.; Bisquert, J., Organic photoelectrochemical cells with quantitative photocarrier conversion. *Energy & Environmental Science* **2014,** *7* (11), 3666-3673.
26. Ifraemov, R.; Shimoni, R.; He, W.; Peng, G.; Hod, I., A metal–organic framework film with a switchable anodic and cathodic behaviour in a photo-electrochemical cell. *Journal of Materials Chemistry A* **2019,** *7* (7), 3046-3053.
27. Li, F.; Wang, Y.; Du, J.; Zhu, Y.; Xu, C.; Sun, L., Simultaneous oxidation of alcohols and hydrogen evolution in a hybrid system under visible light irradiation. *Applied Catalysis B: Environmental* **2018,** *225*, 258-263.
28. Davis, S. E.; Ide, M. S.; Davis, R. J., Selective oxidation of alcohols and aldehydes over supported metal nanoparticles. *Green Chemistry* **2013,** *15* (1), 17-45.
29. Le, Q. V.; Hong, K.; Jang, H. W.; Kim, S. Y., Halide perovskite quantum dots for light-emitting diodes: properties, synthesis, applications, and outlooks. *Advanced Electronic Materials* **2018,** *4* (12), 1800335.
30. Vitoreti, A. B. F.; Agouram, S.; Solis de la Fuente, M.; Muñoz-Sanjosé, V.; Schiavon, M. A.; Mora-Seró, I., Study of the Partial Substitution of Pb by Sn in Cs–Pb–Sn–Br Nanocrystals Owing to Obtaining Stable Nanoparticles with

Excellent Optical Properties. *The Journal of Physical Chemistry C* **2018,** *122* (25), 14222-14231.
31. Cardenas-Morcoso, D.; Gualdron-Reyes, A. F.; Vitoreti, A. B. F.; Garcia-Tecedor, M.; Yoon, S. J.; de la Fuente, M. S.; Mora-Sero, I.; Gimenez, S., Photocatalytic and Photoelectrochemical Degradation of Organic Compounds with All-Inorganic Metal Halide Perovskite Quantum Dots. *Journal of Physical Chemistry Letters* **2019,** *10* (3), 630-636.
32. Ravi, V. K.; Scheidt, R. A.; Nag, A.; Kuno, M.; Kamat, P. V., To Exchange or Not to Exchange. Suppressing Anion Exchange in Cesium Lead Halide Perovskites with PbSO4–Oleate Capping. *ACS Energy Letters* **2018,** *3* (4), 1049-1055.
33. Akkerman, Q. A.; Gandini, M.; Di Stasio, F.; Rastogi, P.; Palazon, F.; Bertoni, G.; Ball, J. M.; Prato, M.; Petrozza, A.; Manna, L., Strongly emissive perovskite nanocrystal inks for high-voltage solar cells. *Nature Energy* **2016,** *2* (2), 16194.
34. Subha, N.; Mahalakshmi, M.; Myilsamy, M.; Neppolian, B.; Murugesan, V., The influence of n-type and p-type dopants on the interfacial charge transfer and the band structure of Bi2MoO6 to enhance solar H2 production. *Journal of Photochemistry and Photobiology A: Chemistry* **2019,** *379*, 150-158.
35. Arcas, R.; Peris, E.; Mas-Marzá, E.; Fabregat-Santiago, F., Revealing the contribution of singlet oxygen in the photoelectrochemical oxidation of benzyl alcohol. *Sustainable Energy & Fuels* **2021,** *5* (4), 956-962.
36. Azevedo, J.; Seipp, T.; Burfeind, J.; Sousa, C.; Bentien, A.; Araújo, J. P.; Mendes, A., Unbiased solar energy storage: Photoelectrochemical redox flow battery. *Nano Energy* **2016,** *22*, 396-405.
37. Shapiro, D.; Duffy, J.; Kimble, M.; Pien, M., Solar-powered regenerative PEM electrolyzer/fuel cell system. *Solar Energy* **2005,** *79* (5), 544-550.
38. Li, R.; Kobayashi, H.; Guo, J.; Fan, J., Visible-Light Induced High-Yielding Benzyl Alcohol-to-Benzaldehyde Transformation over Mesoporous Crystalline TiO2: A Self-Adjustable Photo-oxidation System with Controllable Hole-Generation. *The Journal of Physical Chemistry C* **2011,** *115* (47), 23408-23416.
39. Salvador, P.; Hidalgo, M. G.; Zaban, A.; Bisquert, J., Illumination Intensity Dependence of the Photovoltage in Nanostructured TiO2 Dye-Sensitized Solar Cells. *The Journal of Physical Chemistry B* **2005,** *109* (33), 15915-15926.

APPENDIX IV

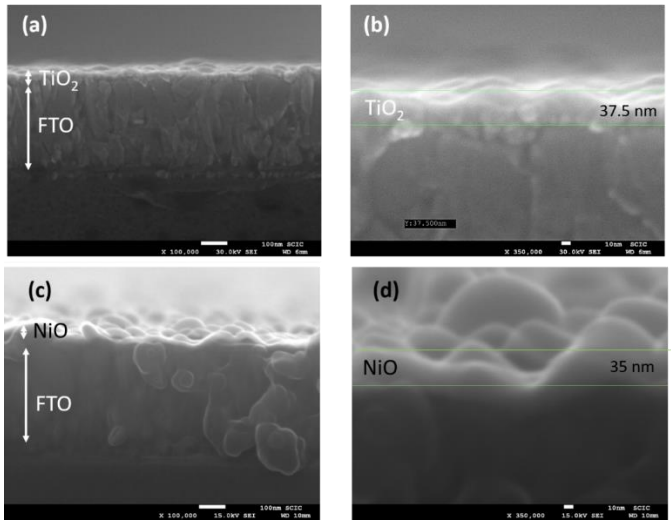

Figure A6.1. Cross-section SEM images of (a), (b) FTO/TiO_2 and (c), (d) FTO/NiO electrodes, illustrating layer thickness (37 nm for TiO_2 and 35 nm for NiO).

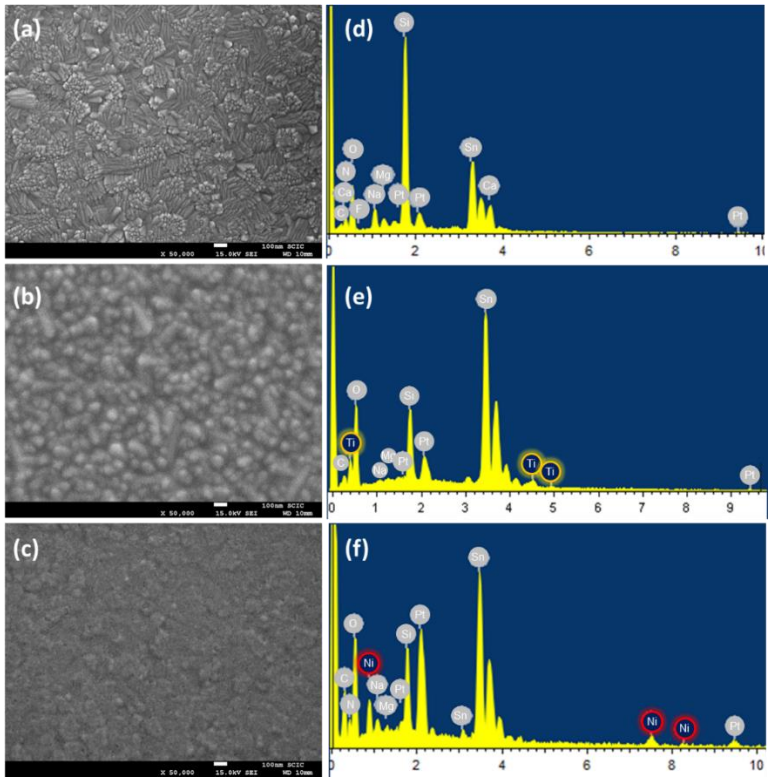

Figure A6.2. Top-view SEM images (a) FTO substrate, (b) FTO/TiO_2 and (c) FTO/NiO electrodes. All images were taken at the same magnification (scale bar 100 nm). EDS spectra of the (d) FTO substrate, (e) FTO/TiO_2 and (f) FTO/NiO electrodes.

The signals from EDS spectra reveal the presence of the elements corresponding to the glass substrate (Si, Na, Ca, Mg and O), the FTO film (Sn, F and O) and the Pt coating, together with those of the TiO_2 (Ti, O) or NiO (Ni, O) electrodes.

Table A6.1. Quantitative analysis of the EDS measurements showed in **Figures A6.2** and **A6.4**, confirming the presence of Ti in FTO/TiO_2 and Ni in FTO/NiO layers, as well as the presence of the $CsPbBr_3$ perovskite NCs on top of the electrodes.

	FTO/TiO_2	**FTO/NiO**	**FTO/TiO_2 /NCs**	**FTO/NiO /NCs**
Element	Atomic%	Atomic%	Atomic%	Atomic%
Si K	7.99	16.68	4.08	4.72
Ti/Ni K	**1.51**	**0.81**	**2.06**	**0.50**
Sn L	22.48	7.70	8.64	17.87
Pt M	1.36	3.10	1.20	1.08
Cs L	-	-	**1.19**	**1.62**
Pb L	-	-	**1.57**	**1.00**
Br L	-	-	**4.61**	**3.46**

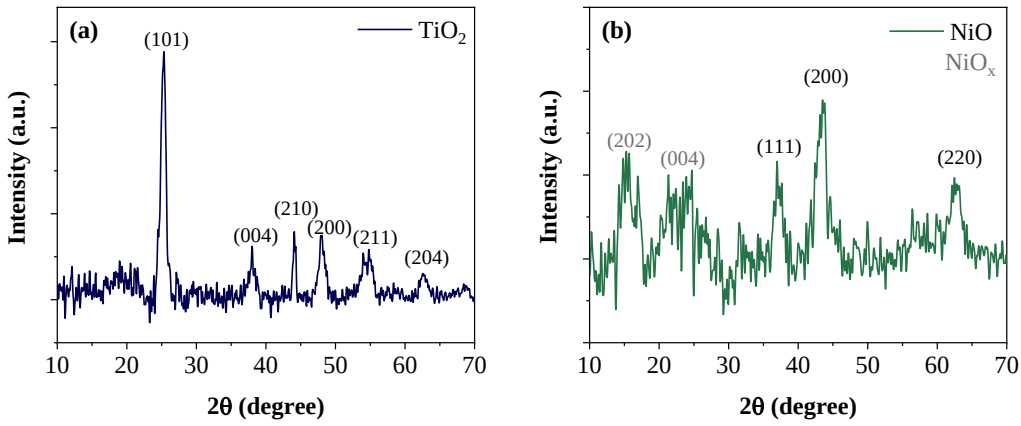

Figure A6.3. XRD diffractograms of the (a) FTO/TiO_2 and (b) FTO/NiO electrodes. Indexed X-ray diffraction peaks in TiO_2 correspond to anatase (card JCPDS 21-1272), while those for Nickel oxide match with cubic NiO (card JCPDS 73-1519), although a small fraction of NiO_x, (card JCPDS 14-0742) is also identified and labeled in grey color.

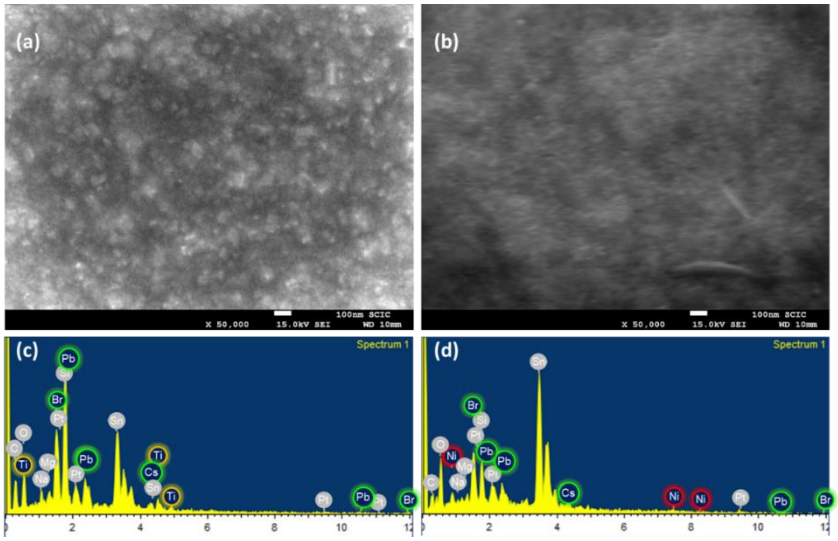

Figure A6.4. Top view SEM images of the (a) FTO/TiO_2/$CsPbBr_3$ and (b) FTO/NiO/$CsPbBr_3$ heterostructured photoelectrodes showing homogeneous deposition of $CsPbBr_3$ NCs on the metal oxide layers. EDS spectra of the (c) FTO/TiO_2/$CsPbBr_3$ and (d) FTO/NiO/$CsPbBr_3$ electrodes. The signals from EDS spectra reveal the presence of the elements corresponding to the glass substrate (Si, Na, Ca, Mg and O), the FTO film (Sn, F and O) and the Pt coating, together with those of the TiO_2 (Ti, O) or NiO (Ni, O) films, and the perovskite layer (Cs, Pb, Br).

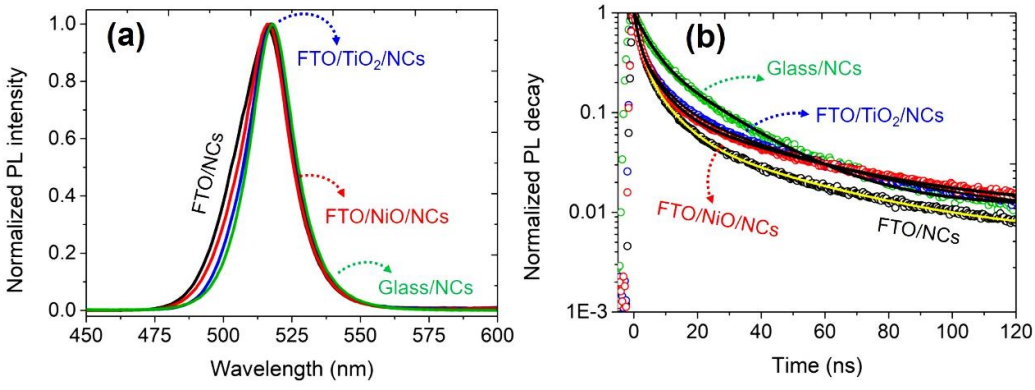

Figure A6.5. (a) Steady-state and (b) time-resolved photoluminescence measurements showing the consistency of the emission properties of $CsPbBr_3$ NCs, independently of the underlying substrate and the slower PL decay on films with selective contacts, indicating enhanced carrier lifetimes.

Table A6.2. Fitting parameters from the time-resolved PL decays of the $CsPbBr_3$ NCs deposited on FTO, FTO/TiO_2 and FTO/NiO and glass substrates to a bi-exponential function: $y = y_0 + A_1 e^{-x/\tau 1} + A_2 e^{-x/\tau 2}$. The values of τ_{avg}, are obtained from their respective definitions: $\tau_{avg} = (\Sigma A_i \tau_i^2 / \Sigma A_i \tau_i)$.[32]

Sample	A_1 (%)	τ_1 (ns)	A_2 (%)	τ_2 (ns)	τ_{avg} (ns)
FTO/NCs	0.47	35.3	0.53	3.7	18.5
FTO/TiO_2/NCs	0.59	36.2	0.41	4.3	23.7
FTO/NiO/NCs	0.34	3.7	0.66	30.5	21.4
Glass/NCs	0.38	49.4	0.62	11.2	27.5

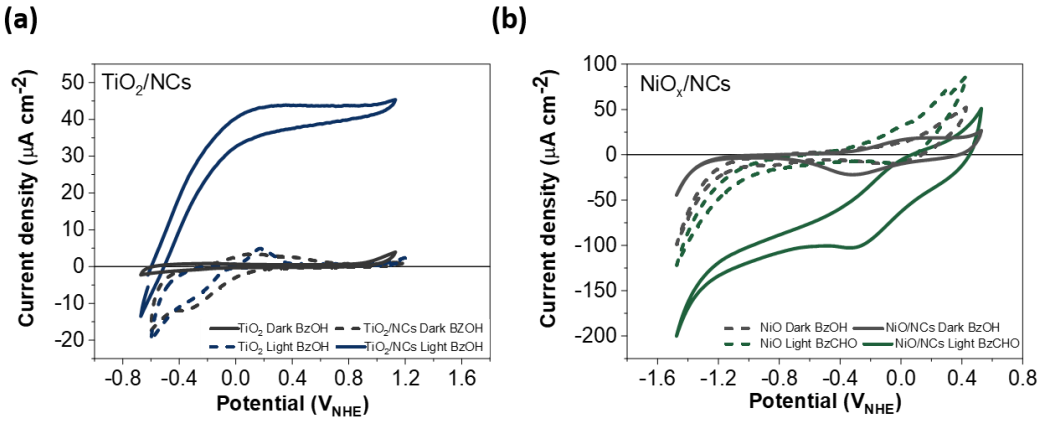

Figure A6.6. Photoelectrochemical characterization of the FTO/TiO_2 and FTO/NiO layers without and with the $CsPbBr_3$ NCs layer for (a) BzOH oxidation (to BzCHO) and (b) BzCHO reduction (to BzCHO) filtering the UV light in 0.05 M of BzOH and 0.05 M of BzCHO in 0.1 M Bu_4NPF_6 in dichloromethane electrolyte.

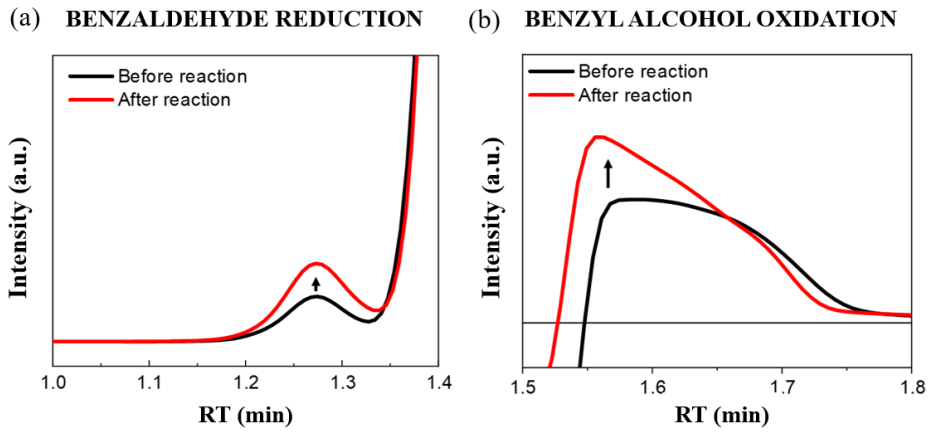

Figure A6.7. HPLC chromatograms for the a) benzaldehyde reduction (benzyl alcohol appears at retention time 1.28 min) and b) benzyl alcohol oxidation (benzaldehyde appears at retention time 1.57 min) after 20 min of chronoamperometric measurements at 0.15 V vs NHE (red). Note that the black line that corresponds to the blank before the reaction, exhibits some traces of the products, already present in the commercial reagent.

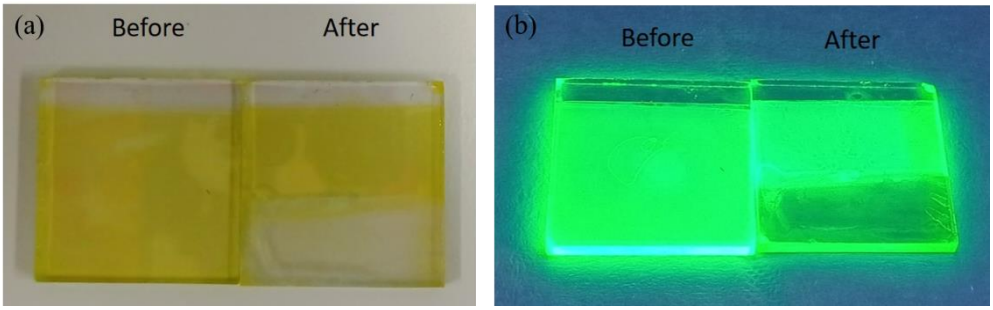

Figure A6.8. Photographs of the FTO/TiO_2/NCs samples under (a) visible and (b) UV light irradiation before and after electrochemical testing, showing the delamination of the NCs layer. Similar behavior is observed for the FTO/NiO/NCs electrodes.

Experimental section

Chemical and solvents: Nickel acetate tetrahydrate ($Ni(OAc)_2 \cdot 4H_2O$, 98% Alfa Aesar), 2-methoxyethanol (MeOEtOH, 99%, Fisher Chemical), and monoethanolamine (MEA, Sigma Aldrich), Nickel (II) acetylacetonate (95%, Sigma-Aldrich), Hydrochloric acid (37%, ACS reagent, Sigma-Aldrich),

Dichloromethane HPLC grade (VWR Chemicals BDH), Tetrabutylammonium hexafluorophosphate (TBFP, 98%, Sigma-Aldrich), Cs_2CO_3 (99.9 %, Sigma-Aldrich), oleic acid (OA, 90 %, Sigma-Aldrich), 1-octadecene (1-ODE, 90 %, Sigma-Aldrich), PbBr2 (ABCR, 99.998%), oleylamine (OLA, 98 %, Sigma-Aldrich), methyl acetate (MeOAc, 99.5%, Sigma Aldrich), hexane (CHROMASOLV, 99.7 %, Honeywell), n-octane (Alfa Aesar) were used as received from the chemical suppliers without further purification.

Synthesis of $CsPbBr_3$ NCs: $CsPbBr_3$ perovskite NCs were obtained by a hot-injection synthetic protocol through stoichiometrically mixing both the Cs-oleate and $PbBr_2$ solutions with some modifications. The corresponding chemicals were used without purification processes. To obtain the Cs-oleate solution, Cs_2CO_3 (0.61 g, 1.87 mmol) and oleic acid (OA, 1.9 mL, 5.98 mmol) were mixed in 30 mL of 1 octadecene (1-ODE) into a 50 mL-three neck flask under vacuum for 30 min at 120 °C and kept under vacuum for 30 min. The mixture was heated to reach 150 °C under N_2-purge to dissolve the Cs_2CO_3 completely. In order to prevent the Cs-oleate precipitation to produce Cs_2O, the resultant solution was kept at 120 °C under vacuum.

In order to synthesize pure $CsPbBr_3$, $PbBr_2$ (0.85 g, 2.32 mmol) was mixed with 50 mL 1-ODE into a 100 mL-three neck flask and then degasified at 120 °C under vigorous stirring for 1 h. Then, 5 mL of each preheated OA (5 mL, 15.8 mmol) and oleylamine (5 mL, 15.2 mmol) were added to the flask at heated again at 170 °C. Simultaneously, 4 mL of preheated Cs-oleate was swiftly injected at this temperature into $PbBr_2$ solution, obtaining a green precipitate in the colloidal solution. Immediately, the flask was immersed into an ice bath for 5 s to quench the reaction. For isolating process, a two-steps purification of NCs was performed. First, the dispersed NCs were centrifuged at 5000 rpm for 5 min with methyl acetate (MeOAc) (all final NCs liquor washed with 120 mL MeOAc).

The precipitated NCs were recovered from supernatant and re-dispersed in 5 mL of hexane. Second, 6 mL of MeOAc was added to the NCs dispersion and centrifuged again at 5000 rpm for 5 min. The NCs solid was separated from supernatant and redispersed with hexane. The final colloidal solution was stored in the fridge for at least 24 h before use, in order to decant residual products. The colloidal NCs solution was dried in a N_2 atmosphere and the precipitate was concentrated at 50 mg/mL with octane for further analysis.

Synthesis of NiO precursor solution: 5 mL of NiO precursor solution was prepared by mixing 50 μL of 38% HCl and 5 mL anhydrous ethanol. Then, Nickel (II) acetylacetonate (129 mg, 0.5 mmol) was added to the mixture and the resulting solution was left stirring overnight at room temperature. Before using the solution, it was filtered to remove undissolved material. The solution was left to stand before filtering to allow sedimentation to occur, then the clear solution was taken from the top and filtered with Poly(tetrafluoroethylene) (PTFE hydrophobe, 0.22 μm particle size, Labbox).

Preparation of NiO/ $CsPbBr_3$ and TiO_2/ CsPbBr3 films: First, 2.5 x 2.5 cm^2 FTO substrates (Pilkington, TEC-15) were washed with soap/Milli-Q water, then rinsed with ethanol and finally with a 3:1 isopropanol-acetone solution sonicating during 15 min each one and dried under air flow. Before spin-coating the metal oxide layer, the substrates were treated under UV-O_3 for 15 min. To deposit the nickel oxide layer, the NiO precursor solution described above (70 μL) was spin-coated at 5000 rpm and 1200 ac for 30 s. Then, after drying on a hot plate at 100 °C during 1 min, the as-deposited NiO layer was annealed at 375 °C for 45 min. To deposit the TiO_2 layer, a Ti-alkoxide solution (ShareChem, SC-BT060, 80 μL) was spin-coated at 4000 rpm and 1000 ac for 30 s. The as-deposited TiO_2 layer was dried at 150 °C for 10 min. Then, the TiO_2 films were annealed at 500 °C for 30 min. Three layers of the purified $CsPbBr_3$ NCs solution in octane were

deposited by spin-coating on either NiO or TiO_2 layer at 1000 rpm for 30 s. Between each $CsPbBr_3$ NCs layer deposition, the substrates were cleaned, first, using a solution composed by 10 mg mL^{-1} of $Pb(NO_3)_2$ in methyl acetate and dried under nitrogen flow and then with neat methyl acetate and dried again.

Structural and optical characterization: XRD diffraction data was carried out with a D4 Endeavor system (Bruker-AXS) with Cukα radiation (λ= 1.5406 Å). The morphology of the different samples was analyzed with a JEOL JEM-3100 Field Emission Scanning Electron Microscope (FE-SEM) including EDS analysis. The topography of the samples was recorded using AFM atomic force microscope (Concept Scientific Instrument) on a relatively large area (10 x10 μm). The optical properties of the prepared colloidal solutions and films were determined using a Lambda 1050+ Perkin Elmer UV/Vis/IR spectrophotometer. The absorbance (A) of the thin films was estimated from transmittance (T) and diffuse reflectance (R) measurements using an integrating sphere as A = − log (T + R), and the absorptance (a) was calculated as $a = 1 - 10^{-A}$. Steady-state and time-resolved photoluminescence (PL) measurements were conducted through photoluminescence spectrophotometer (Fluorolog 3-11, Horiba). An excitation wavelength of 420 nm was used to perform the PL measurements. The wavelength range for the measurements was 450–600 nm. Time resolved PL measurements (TRPL) were carried out at 405 nm pulsed laser (NanoLED-405L, <100 ps of pulse width, 1 MHz frequency).

Photoelectrochemical characterization: Cyclic voltammetry, linear sweep voltammetry and chronoamperometric measurements were performed on a commercial H-cell (PECH H-cell 2x1.5 ml, RedoxMe) in three-electrode configuration, using an Autolab Potentiostat/ Galvanostat. A Nafion 212 (FuelCellStore) membrane was used to separate the anodic and cathodic compartments. A non-aqueous $Ag/AgNO_3$ electrode (ALS, Japan) and a

Platinum wire were used as reference and counter electrode, respectively. FTO/TiO2/$CsPbBr_3$ and FTO /NiO/$CsPbBr_3$ electrodes were used as the working electrode on the oxidation and reduction reactions, respectively. A solution of 0.1 M Tetrabutylammonium hexafluorophosphate (Bu_4NPF_6) in dichloromethane was used as supporting electrolyte. 0.05 M BzOH/0.05 M BzCHO were the initial concentrations in the oxidation and reduction compartments, respectively. To calibrate the system to the Normal Hydrogen Electrode (NHE) scale, the Ferrocene/Ferrocenium (Fc/Fc^+) couple was used as internal standard, by adding 1.9 mM of ferrocene after the electrochemical tests. Films were back-side illuminated with a Xe lamp at 1 sun, filtering the UV light with a 400 nm high pass neutral filter to avoid the photoelectrocatalytic activity of both TiO_2 and NiO layers.

Product analysis: Identification and quantification of evolved products was carried out by High-Performance Liquid Chromatography (HPLC) performed on a 1260 Infinity II Agilent equipment. An Agilent (poroshell EC-C18, 4.6x100 mm, 2.7µm) set at 40.0 °C and a DAD detector (UV range) column was used for product separation and detection. The eluent rate used was 0.9 mL/mL a 35%-65% water-acetonitrile mixture and the volume of sample injection was 5.0 µL. Faradaic efficiencies (%FE) were calculated according to the expression: $FE = (n_{experimental}/n_{theoretical}) \cdot 100$. The theoretical moles were calculated by the Faraday's law: $n_{theoretical} = \frac{j \cdot t}{n \cdot F}$, where *j* is the current density recorded during the chronoamperometry measurement, t is the time in seconds, n is the number of electrons transferred in the reaction (n=2 in the addressed reactions) and F is the Faraday constant, 96485.33 C mol^{-1}, nexperimental was determined by HPLC.

Chapter 7

Concluding remarks and outlooks

The scalability of efficient (photo)electrochemical systems for the production of fuels and chemicals constitutes one of the key challenges towards a sustainable future. In this context, the investigation of efficient and durable (photo)electrocatalysts based on earth-abundant materials and cost-effective manufacturing processes is essential. In the present PhD thesis, these challenges were addressed by the design, synthesis and functional evaluation of novel (photo)electrocatalytic materials for hydrogen production, CO_2 reduction and organic transformations. Furthermore, a wide library of microscopic and spectroscopic techniques was employed to understand the operation mechanisms and to propose optimization guidelines. The main conclusions obtained are listed below:

(i) A low-cost, rapid and sustainable synthesis for preparing copper sulfide ($Cu_{2-x}S$) electocatalysts was designed and optimized.

(ii) A complete chemical and structural characterization of the $Cu_{2-x}S$ electrodes revealed a nanoporous structure, characteristic of foamy materials.

(iii) The $Cu_{2-x}S$ electrodes were evaluated for the hydrogen evolution reaction (HER), exhibiting a record durability of almost one month of continuous operation, with Faradaic efficiencies close to 100% during several days. An 8-fold increment of the current density was obtained,

mainly attributed to an increaseof the electrochemically active surface area (ECSA) during continuous operation.

(iv) Cu centred species were responsible for the catalytic operation during HER, as concluded by the analysis of the results provided by a combination of powerful characterization techniques including spectroelectrochemistry (SEC), *quasi-in situ* XPS and *operando* XRD. Indeed, it was the first time that SEC was employed for electrochemical HER with Cu-based electrodes.

(v) Future studies to improve the functional performance of $Cu_{2-x}S$ electrocatalysts will be focused on the preparation of $Cu_{2-x}S$ nanoparticles, their deposition on different substrates and the exploration of alternative electrochemical reactions.

(vi) The $Cu_{2-x}S$ electrocatalyst also showed outstanding performance for the carbon dioxide electrochemical reduction (CO_2ER). By adjusting the measurement conditions, an impressive enhancement of the Faradaic Efficiency from 35% to 75% was obtained for the production of formate. A correlation between the selectivity for formate and the crystallinity of the Cu (111) facet was suggested, in good agreement with previous reports.

(vii) Complementary surface characterization, such as near ambient pressure (NAP)XPS could confirm this correlation.

(viii) Future optimization of this material for CO_2 reduction electrocatalysis could be based on the synthesis predicted Cu (111) nanocrystals.

(ix) The photoelectrochemical behavior of $CsPbBr_3$ nanocrystalloine photoelectrodes was succesfully tailored by engineering the selective contacts and accepting species in the electrolyte.

(x) This concept was successfully applied to the photoelectrochemical oxidation of benzyl alcohol (BzOH) to benzyl aldehyde (BzCHO) and

the reverse photoelectrochemical reduction of BzCHO to BzOH, as a proof-of-concept to validate the huge potential of halide perovskite nanocrystals for photoelectrochemical transformations.

(xi) Future work should address the implementation of robust stabilization strategies to move beyond the proof-of-concept stage to relevant technological developments.

Summarizing, the results obtained in this PhD thesis provide valuable strategies for the rational design of efficient (photo)electrocatalysts. A wide range of advanced microscopic and spectroscopic characterization techniques has demonstrated to be essential to provide a complete mechanistic description of the addressed reactions. Furthermore, the strategies developed during this thesis for the synthesis and characterization of materials and electrodes can be extended for the investigation of alternative materials and (photo)electrochemical reactions.